Study on Development in Medical Bone Regeneration and Biodegradable of Mg-Based Alloys for Biomedical Applications

骨の再生医療における Mg 基合金の開発と生分解性に関する研究

Haijian Wang

Saitama Institute of Technology

August, 2020

Contents

Abstract

Nowadays, the approved and commonly metallic biomaterials include stainless steels, titanium alloys, cobalt-chromium-based alloys and noble metals. The limitations of these current metallic biomaterials are the possible release of toxic metallic ions or particles through corrosion or wear processes and the long-term biological incompatibility caused by interactions between tissues and permanent metallic implants. Magnesium (Mg) alloys are considered as the new generation of biomedical implant materials due to their good biocompatibility, biodegradability and excellent mechanical properties. This paper reports an exploratory study on the biodegradation of Mg-RE (RE - rare-earth elements) alloy sheets with fine grain around amorphous zone produced by vertical twin roll casting (TRC) and its interaction with rat femur was observed by micro-CT, which provides a novel method of crystalline/amorphous structuring alloy design and an important evidence of the potential use of Mg-RE for future surgical implant applications.

A new type of Mg-RE (Ce, La) sheets were prepared by vertical (TRC) technology. The microscopic characterization experiments show that the crystal structure is crystalline phase containing amorphous phase. Electrochemical experiments and immersion testing both showed that Mg-RE (La,Ce) sheet with TRC has a better corrosion resistance than master alloy of Mg-RE alloys, and a uniform corrosion layer on the sheet surface. *In vivo* tests show that Mg-RE sheets have better biocompatibility and induce new bone formation.

Mg-RE and AZ31 sheets were prepared by vertical (TRC) technology under identical casting conditions. The microstructure characterization showed that the Mg-RE exhibited a higher amorphous forming ability than the AZ31. Moreover, the results of electrochemical impedance spectroscopy (EIS) and potentiodynamic polarization indicated that the Mg-RE sheets displayed a higher corrosion resistance compared with the AZ31 sheets. Additionally, the Ti, Mg-RE and AZ31 sheet implants were immobilized and implanted in a rat femur model to observe degradation behavior during 16 weeks. *In vivo* tests showed that no significant change in the femur surrounding the Ti group, which excluded the external factor that the new bone formation resulting from bone remodeling.

Furthermore, the Mg-RE group induced more newly formed bones, which met the necessary conditions for the prevention of pathological fractures.

Two casting speeds of 10 rpm and 30 rpm were used in vertical twin-roll casting (TRC) to obtain Mg-rare earth (Mg-RE) alloys. The results indicated that the roll-castings of TRC-30-rpm exhibited a finer grain size and higher volume fraction of non-crystallization than those in castings of TRC-10-rpm. Moreover, the results of electrochemical impedance spectroscopy (EIS) and potentiodynamic polarization indicated that the castings of TRC-30 rpm displayed a higher corrosion resistance compared to those in the castings of TRC-10-rpm. Animal tests showed that a higher degree of newly formed bone tissues was achieved by implants of TRC-30-rpm. Additionally, *in vivo* tests displayed that degradation properties of the TRC-30-rpm implants were better than those of the TRC-10-rpm implants; furthermore, the degradation layer was a two-layer structure, and P and Ca were enriched in the outer degradation layer. In summary, these findings elucidated that casting speed has a substantial effect on the microstructure and degradation property of Mg-based implants, and the degradation property performs better with increased casting speed.

Keywords: Magnesium alloys, Biomedical materials, Microstructure, *In vivo* degradation and bone response

Chapter 1 Introduction

For a long time, the biological materials, such as artificial joints and sutures, have been implanted in body to heal damaged tissue. The artificial joints as a permanent implant require high durability, while the sutures as a biodegradable implant are broken down and absorbed by the body after tissue repair. In the past, the implants were usually durable and permanent, so they had to be surgically removed after tissue repair. However, the biodegradable materials have been developed and used as fixation materials for fractures, such as polylactic acid materials (PLA) are used for suture and as a fixed material for fractures in low-burden areas, thus reducing the burden of reoperation. In addition, the calcium cyanate ceramics can also be used as the bone - free compensation materials. However, only polymers and ceramic materials are developed, and their applications in biomedical materials are limited. Because these biodegradable absorbent materials lack the necessary mechanical strength, they cannot be overused in stressed areas. Therefore, it is desirable to develop biomaterials with better mechanical and better biodegradable properties.

In recent years, the application of magnesium (Mg) alloy in biodegradable materials have attracted the attention of researchers and medical personnel. Mg has high specific strength and is the lightest of the practical metal materials used as structural materials. In addition, as Mg is a bio-essential element, the biological safety of magnesium alloys remains high after *in vivo* degradation.

1.1 Biomedical Materials

Biomaterial can be made into devices that can be used to diagnose, treat or replace tissues and organs that are weakened or completely lost due to lesions or damage [1]. Biomaterials can be natural, synthetic, or a combination of them. As early as 5000 BC, there are records of artificial teeth being used to repair lost teeth in ancient Egypt and China. In the 2nd century AD, there are records of artificial teeth being used as suture lines to

ligate wounds and prevent arterial blood loss. With the rapid development of social progress and modern science and technology, the biomedical material industry has also entered its rapid development stage, which plays an important role in improving people's quality of life and guaranteeing human health. It has gradually become an emerging industry with extremely rapid development.

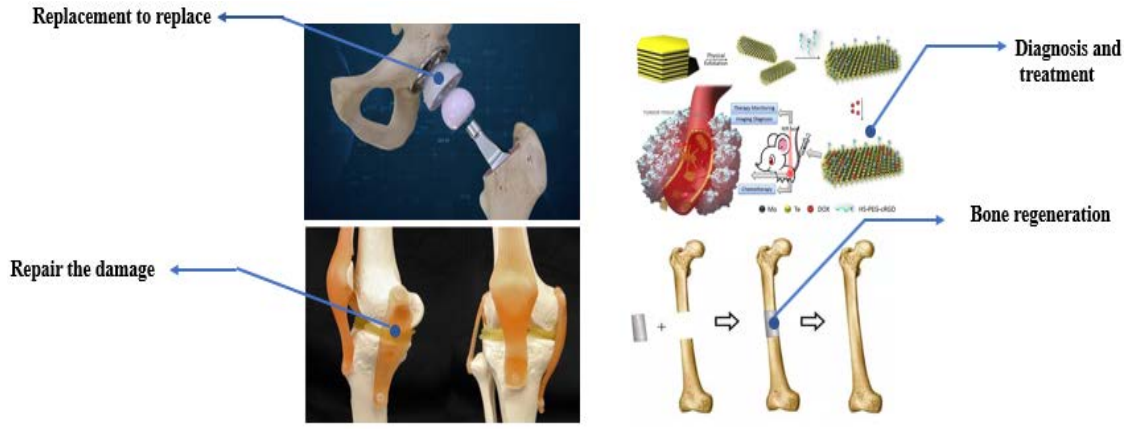

Fig. 1.1 Various biomedical materials and their functions [1].

Biomedical materials can be classified into three categories according to the biochemical reaction level of materials in physiological environment: (1) nearly inert biological materials, (2) bioactive materials, (3) biodegradable and absorbable biological materials. According to the traditional material composition and properties, biomedical materials can be divided into five categories: (1) medical metal materials, (2) medical polymer materials, (3) biological ceramic materials, (4) biological derivative materials and (5) biomedical composite materials. Each of them account for more than 40 percent of biomaterial application amount. Table 1-1 describes the application, advantages and disadvantages of different types of biomaterials.

Table 1-1 Commonly used biomaterials [2]

Materials category	Advantage	Shortcoming	Application
Metallic materials (Titanium and its alloy; CO-Cr alloy; Stainless steel; Au; Pt, etc)	High strength; stiffness; flexible	Easy-corrosive high density	Joint replacement; Bone nail and bone plate
High polymer material	Good resilience; Easy preparation	Low intensity; Prone creep	Stylolite; blood vessel, ear, soft tissue
Ceramics (aluminum oxide; calcium phosphate; base apatite, etc)	Good biocompatibility; inert, high compression strength	Too brittle, poor elasticity; Not easy processing	Surface coatings for dental, femoral head, dental and orthopedic implants
Composites (carbon-carbon composites, carbon fiber reinforced bone cement, etc.)	High strength, can be cut	Not easy preparation	Joint implants, heart valves

1.2 Biomedical metallic materials

Metal materials are applied as biological materials due to their excellent mechanical properties and good electrical conductivity and thermal conductivity. Because the metal bonds in metal materials are non-directional, they can change the position of metal atoms without destroying the crystal structure. Therefore, metal materials show the characteristics of plastic deformation.

Due to its excellent mechanical properties and corrosion resistance, some metal materials can be applied to replace bone screws, plates and other bone fracture repair devices of hard tissues such as hip and knee joints, spinal fixation devices and dental

implants. It can also be applied to cardiovascular stents, orthodontic teeth, cochlear implants and other places that need to play an active role in the location.

Fig. 1.2 Biomedical metallic materials.

The alloying elements in most medical metal materials are allowed in very small amounts in the human body. Trace amounts of metallic elements can play a positive role in human body. For example, trace amounts of Fe are very important for red blood cells, and Co is an essential element for the synthesis of vitamin B12. However, when the intake of these metallic elements exceeds the limit of human body, it will have many negative effects on human physiological functions [3]. Due to the long-term existence of metal implants in the human body and the corrosion of the internal body fluid environment, it is inevitable that trace elements will be dissolved into the human body. Therefore, the biocompatibility of metal elements is an important factor that metal materials as biological materials must be concerned. At present, the widely used medical metal materials mainly include four categories: stainless steel, titanium alloy, cobalt-based alloy and precious metal.

1.2.1 Stainless steel bone reinforcement plate

The first-generation stainless steel used in making implanted devices is 302 stainless steel, and the stainless steel has higher strength and more excellent corrosion resistance in the human body environment compared to the vanadium steel. The researchers found that based on the composition of 302 stainless steel by adding a small amount of Mo (2 ~ 4 wt %) can significantly improve corrosion resistance in saline environment features. The

introduction of Mo in the composition stainless steel can dramatically improve the performance of the resistance to pitting formation caused by chloride ion. In the last century 1950s, the researchers further enhance the corrosion resistance of stainless steel in the physiological saline by reducing the concentration of the carbon element in stainless steel (0.08 wt % decrease to 0.03 wt %), which is now known as SUS316/316L stainless steel and its composition as shown in table 1-2. The Cr content in stainless steel must be higher than 12 wt % to guarantee enough corrosion resistant performance, and the Ni is used to make stainless steel in the austenite phase to keep stable at room temperature [4].

The SUS316/316L steels are austenitic stainless steels and are widely used in the manufacture of medical implant devices. They are difficult to be strengthened by heat treatment, but it can be strengthened by work hardening. The mechanical properties of SUS316/316L stainless steel show in Table 1-3.

Fig. 1.3 Stainless steel bone reinforcement as bone fixed implants.

Although SUS316/316L steel has a good corrosion resistance in the biotic environment. when the material is subject to the great stress and in the absence of oxygen environment, it will also be corroded, such as the position where the bone nail contacts the bone. The material will lose its fixation function due to the influence of corrosion. Therefore, the SUS316/316L stainless steel can only be used as temporary implant device when it is used as bone nail, bone plate and femoral head nail.

Table1-2 Composition of USL316L stainless steel [2]

Element	C	Mn	P	S	Si	Cr	Ni	Mo
Content wt%	<0,03	<2.00	<0.03	<0.03	<0.75	17~20	12~14	2~4

Table1-3 Mechanical properties of USL316L stainless steel for implants [2]

Condition	YTS (MPa)	UTS (MPa)	Elongation (%)	Rockwell hardness
Annealed	172	485	40	95
Cold-worked	690	860	12	-

1.2.2 Bone reinforcement plate of CoCr alloy

The CoCrMo with the as-cast state is common typical alloy. The as-cast CoCrMo alloy has been used as a medical metal for decades. It was mainly used as a dental material in the early stage. Recently, it has been widely used in the field of artificial joints. The deformed CoNiCrMo alloy as a medical metal material has a relatively short use time, and it is mainly used to make the handle of knee or hip prosthesis that to bear a large load [5,6].

American ASTM recommends four types of CoCr alloys for use in medical metallic materials: (1) as-cast CoNiCrMo alloy, (2) morphed CoCrWNi alloy, (3) morphed CoNiCrMo alloy, and (4) morphed CoNiCrMoWFe alloy. The chemical compositions are shown in Table 1-4. At present, the cast CoCrMo alloy and the variable CoNiCrMo alloy are most widely used for applications. In these two alloys, the content of Co can be as high as 65%, and the alloy element Mo can significantly refine the grain size of the alloy. The Cr can play a role in solid solution strengthening, on the other hand, it can also significantly improve the corrosion resistance of the alloy [6].

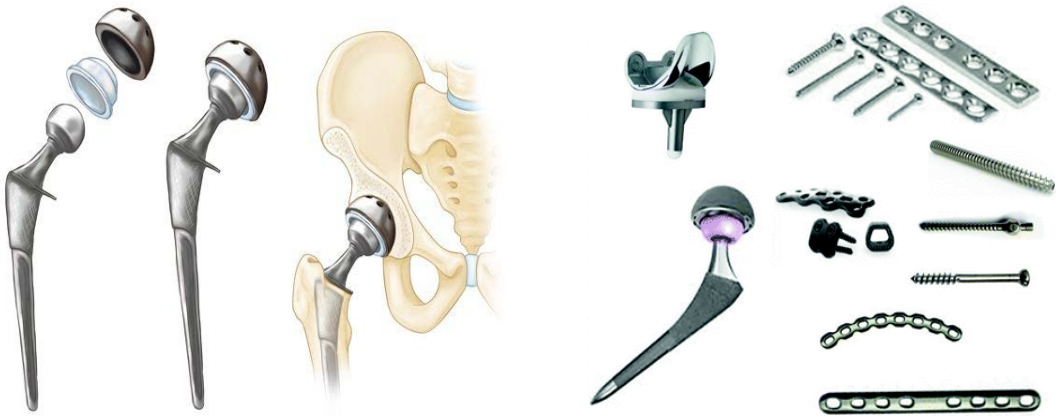

Fig. 1.4 Bone reinforcement of Cobalt alloy.

Table 1-4 Chemical Compositions of Co–Cr alloys [9]

Element (wt. %)	CoCrMo	CoCrWNi	CoNiCrMo	CoNiCrMoWFe
Cr	27.0~30.0	19.0~21.0	19.0~21.0	18.00~22.00
Mo	5.0~7.0	-	9.0~10.5	3.00~4.00
Ni	~2.5	9.0~11.0	33.0~37.0	15.00~25.00
Fe	~0.75	~3.0	~1.0	4.00~6.00
C	~0.35	0.05~015	~0.025	~0.05
Si	~1.00	~1.00	~0.15	~0.05
Mn	~1.00	~2.00	~0.15	~1.00
W	-	14.0~16.0	-	3.0~4.0
P	-	-	~0.01	~0.01
Ti	-	-	~1.0	0.50~3.50
Co		Balance		

Table 1-5 Mechanical properties of Co-Cr alloys [9]

Property	Cast CoCrMo	Wrought CoCrWNi	Wrought CoNiCrMo	
			Solution Annealed	Cold worked and aged
YS/MPa	450	310	240~650	1585
UTS/MPa	655	860	793~1000	1793
Elongation/%	8	10	50	35
Elastic modulus/GPa		220~234		

The deformed CoNiCrMo alloy and the as-cast CoCrMo alloy have similar wear resistance (their wear rate is 0.14mm/year). The CoNiCrMo alloy has high tensile strength and fatigue resistance, which is more suitable for the handle of hip prosthesis. The mechanical properties of the CoCr alloy are shown in Table 1-5. The elastic modulus of the CoCr alloy is 220 ~ 234GPa, so this alloy is very hard with very low wear in metal-metal, which has obvious advantages in application of metal-metal artificial joint replacement [7].

When the CoCr alloy is applied in joint replacement, the metal products result from the metal wear and corrosion will have an adverse effect on the surrounding organ tissues. In vitro experiment results show that the Co particles have a toxic effect on osteoclasts and inhibit the synthesis of I-type collagen, osteocalcin and alkaline phosphatase. However, the metal Cr and CoCr alloy particles did not show significant toxicity. The experiments of metal extraction liquid showed that the Co and the Ni extracts had significant cytotoxicity and significantly reduced the survival rate of cells, thus, the Cr extracts had lower cytotoxicity than Co and Ni [8].

1.2.3 Ti and Ti alloy

In the 1930s, people began to try to apply titanium implant device for manufacturing. It found that the titanium showed better biocompatibility, low density of titanium relative

to the stainless steel, the CoCrMo alloy, and its alloys (as shown in Table 1-6), and the excellent mechanical properties (Table 1-7), which is the most significant advantage used for making implanted devices [10, 11].

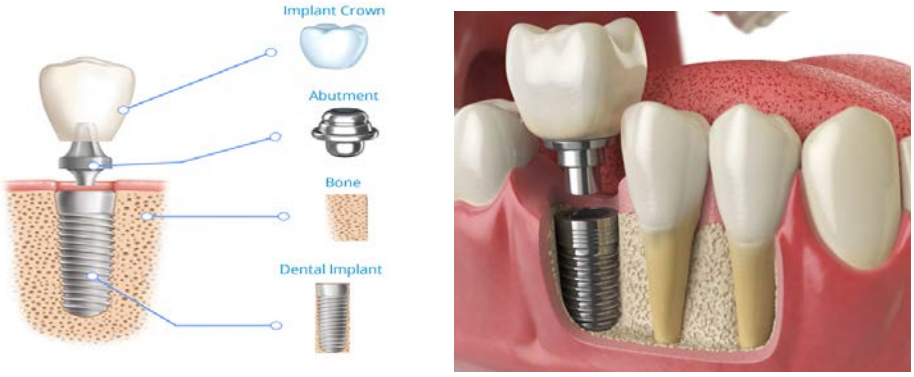

Fig. 1.5 Ti / Ti alloy as dental implants.

Table 1-6 Density of Ti and its alloy; and some metallic implant alloys [10,11]

Alloys	Density (g/cm^3)
Ti and its allloys	4.5
316 Stainless steel	7.9
CoCrMo	8.3
CoNiCrMo	9.2
NiTi	6.7

The pure titanium (Ti) metal as medical implanted is divided into four grades according to its purity, among which the contents of impurity elements, such as O, Fe and N need strict control, especially the impurity element O has a significant adverse impact on the toughness and strength of titanium metal. The Ti6Al4V is widely used in the production of medical implant devices. Its main alloy elements are Al (5.5 ~ 6.5wt%) and V (3.5 ~ 4.5wt%). The alloy element Al could stabilize the α phase by increasing the transition

temperature of the α phase / β phase, while alloy element V stabilizes the β phase by reducing the phase transition temperature of the α phase / β phase [12].

In commercial pure titanium, with the increase of impurity content, the strength increases and the plasticity decreases of the materials. Although the strength of titanium alloy is lower than some stainless steel and CoCr alloy, it's the specific strength is obviously higher than these two materials. In addition, the shear strength of titanium and its alloys is lower, which makes them not suitable for the preparation of bone screws, bone plate and other types of devices which need to withstand higher shear stress. The wear-resisting performance of titanium and its alloys is poorer when it is in contact with the same material or other metal materials, which limits the application as a medical implant metal material [13].

Table 1-7 Mechanical properties of Ti and its alloys [9]

Properties	Pure Ti				Ti6Al4V	Ti13Ni13Zr
	Grade1	Grade2	Grade3	Grade4		
UTS / MPa	240	345	450	550	860	1030
YS / MPa	170	275	380	480	795	900
Elongation / %	24	20	18	15	10	15
E / GPa	110					79

1.3 Biodegradable magnesium alloy

The biomaterials mentioned above are biologically inert, non-biodegradable, and once implanted, they will remain permanently in the body unless removed by a second surgery. The process of a second surgical excision will undoubtedly increase the patient's pain and financial burden (Fig. 6) [14]. Therefore, the development trend of the new generation of biomedical materials not only requires that the materials have good biocompatibility, but also hopes that they can be biodegradable *in vivo*. Medical polymer materials have made

great progress in this direction. However, the polymer materials generally have low elastic modulus and poor plasticity, which are difficult to be applied in some occasions such as cardiovascular stent, bone nail and plate, anastomosis nail, etc. Magnesium and its alloys are biodegradable, and it also has advantages in mechanical properties and processing properties of metal materials [15-19].

1.3.1 Degradation characteristics

The degradation of magnesium alloy is accomplished by corrosion of magnesium alloy in physiological environment. The corrosion process is an electrochemical reaction process, and the total reaction formula can be written as follows [15, 20]:

$$Mg + H_2O = Mg(OH)_2 + H_2 \quad (1\text{-}1)$$

The electrochemical reactions can be decomposed into the following anodic oxidation and cathodic reduction reactions:

$$\text{Anode reaction: } Mg \rightarrow Mg^{2+} + 2e^- \quad (1\text{-}2)$$

$$\text{Cathode reaction: } 2H_2O + 2e^- \rightarrow H_2 + 2OH^- \quad (1\text{-}3)$$

$$\text{Product formation: } Mg^{2+} + 2OH^- \rightarrow Mg(OH)_2 \quad (1\text{-}4)$$

The degradation mechanism of magnesium alloy in physiological environment is shown in Fig. 1.7. When the magnesium alloy comes into contact with the humoral environment, the Mg is oxidized to $Mg2^+$, and the generated electrons are reaction with water to form H_2 and OH^-. Due to the poor electronegativity between the magnesium alloy matrix and the intermetallic compound as the second phase, the above reactions generally occur at the surface position where the magnesium alloy materials are in contact with the fluid environment. At the same time, the organic molecules such as proteins, amino acids and fats, which are widely existed in the humoral environment. It is easy to be adsorbed on the surface of materials, thus affecting the degradation of magnesium alloys.

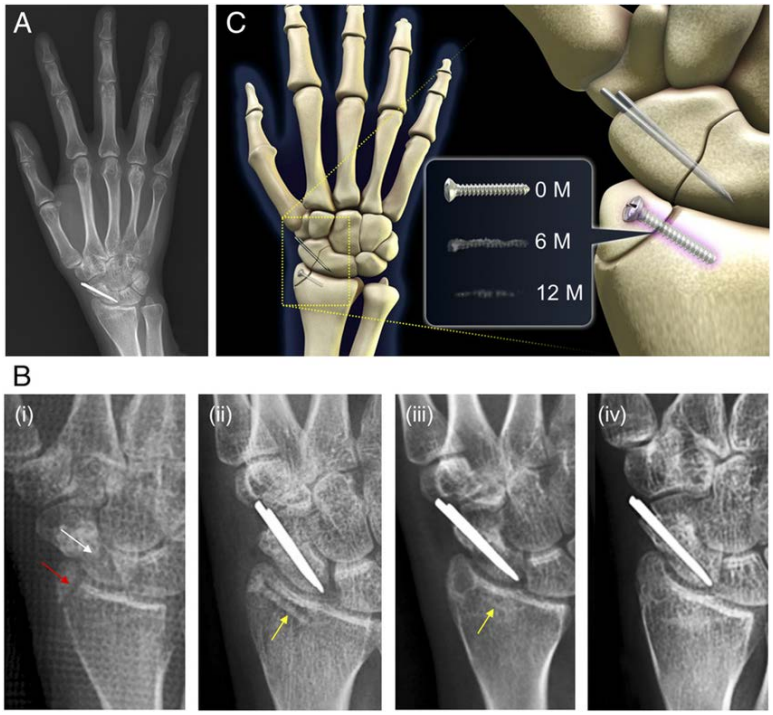

Fig. 1.6 Clinical observation of degradation and bone healing of Mg alloy screw over a 1-year [14].

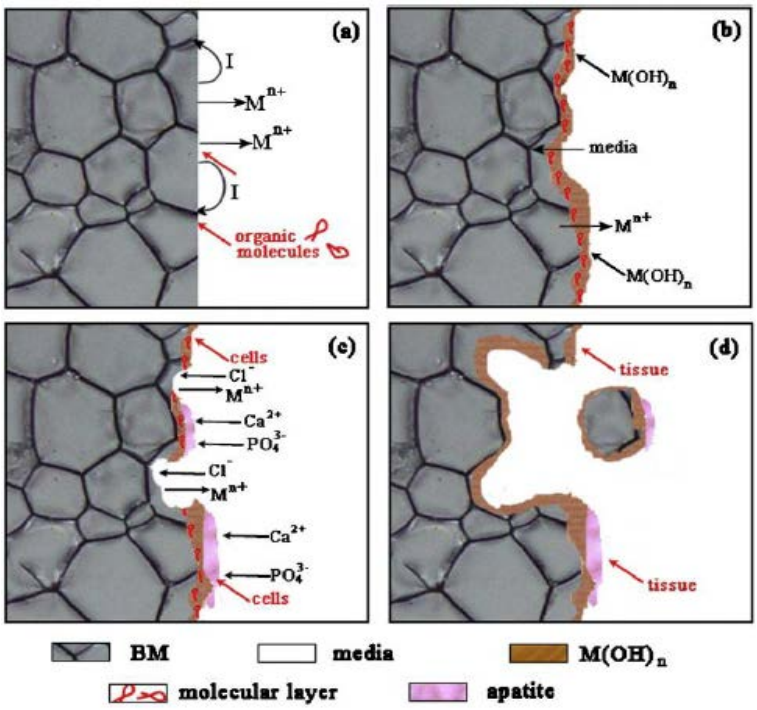

Fig. 1.7 Schematic diagram of the biocorrosion at magnesium/medium interface [15, 20].

The reaction product of $Mg(OH)_2$ is easily dissolved in humoral environment that contains Cl^- ions and absorbed by the body. The adsorption of Cl^- on the surface of the material will lead to the dissolution of $Mg(OH)_2$ protective layer which result in pitting. It is not easy to form a deep corrosion pit in magnesium alloy. This because the corrosion process of magnesium alloy occurs quickly, and the local environment around the place where the corrosion occurs presents a high alkalinity, leading to the difficulty of further corrosion reaction at this place. Because the degradation of magnesium alloy makes the surrounding environment became alkaline, and the saturated Ca ions and phosphates exist in the body fluids, the calcium phosphate is easy to deposit on the $Mg(OH)_2$ product layer, the cells tend to adsorb on this surface layer. With the extension of implantation time, the deposited cells grew into tissues adjacent to the layer of corrosion products [15].

1.3.2 Mechanical properties

Mechanical property is one of the important indexes of magnesium alloy as medical metal materials, which determines the bearing capacity and plastic deformation capacity of medical devices. Pure magnesium has a dense hexagonal crystal structure and only three slip systems, so its plastic deformation ability is poor. The commonly methods to improve the deformation properties of magnesium alloys include alloying heat treatment and deformation processing. By adding the Ca [22], Zr [23], Zn [24] and other alloy elements into magnesium, the grain size of the as-cast magnesium alloy can be significantly refined and the plastic deformation ability of the magnesium alloy can be improved. In addition, it has been reported in the literature [24] that the addition of Nd, Gd, Pr, Dy and other rare earth elements in magnesium alloy can refine the grain size and reduce the stacking fault energy of magnesium alloy, which is considered to be one of the important mechanisms to improve the plasticity of magnesium alloy. It is also helpful for improve the plasticity of magnesium alloy to choose the treatment technology and reduce the rough second phase in the as-cast magnesium alloy.

The strength of pure magnesium is relatively low (between 100 and 150MPa),

which cannot meet the requirements in occasions that requiring higher bearing capacity. To improve the strength of magnesium alloy, there are usually several ways as follows: the firstly, the solid solution strengthening method. The strength of magnesium alloy can be improved by adding Al, Zn, rare earth elements and other alloy elements with solid solution strengthening into pure magnesium. Secondly, the second phase strengthening. The strength of magnesium alloy can be improved by adding alloy elements to the magnesium alloy to form intermetallic compounds with strengthening effect. Thirdly, the grain boundary strengthening. The grain size of magnesium alloy can be effectively reduced through the alloying or thermal deformation processing, the strength of magnesium alloy can be improved by increasing the proportion of grain boundary.

1.3.3 Biocompatibility

The cell toxicity evaluation is an important means of characterization of magnesium alloy biocompatibility. Theoretically, the human body has a limit for the intake of any element [16, 25]. When a certain element is consumed in excess of the limit, it can cause toxic reactions in humans. The biocompatibility of a material is related to its elemental release, which depends on the corrosion rate of the materials. Magnesium is considered as an essential element in human body. However, when the concentration of Mg^{2+} in human serum is higher than 1.05 mmol/L, it will also cause muscle paralysis, hypotension, respiratory disorders and other adverse reactions. When the concentration of Mg^{2+} in blood is as high as 6~7mmol/L, it will also lead to cardiac arrest and other risks.

There are a lot of *in vitro* experimental results show that the main factors affecting the biocompatibility of magnesium alloys are the increase of ambient pH value and the change of magnesium ion concentration due to the degradation of magnesium alloys. The squeezed state of pure magnesium show that the different degradation rates have a significant impact on cell adhesion, proliferation and the cell survival rate [17].

From the year of 2000 to 2003, Heublein et al. [26] attempted to make the degradable cardiovascular stents with AE21 magnesium alloy. They implanted magnesium stents into coronary arteries of domestic pigs. The scaffold lost its mechanical integrity after 35 to 56 days of implantation due to the rapid degradation of magnesium alloy. Biotronik, a German company, has tried to implant magnesium alloy stents made from WE43 into the coronary arteries of miniature pigs, and no deaths have occurred after a period of implantation. In 2005, Peeters et al. [27] who first attempted to implant magnesium alloy stents into 20 patients for the treatment of varicose veins. The stents were completely degraded after 6 weeks, and no adverse reactions such as poisoning or allergy occurred in the patients. In 2007, Biotronik implanted 71 magnesium stents in 63 patients and no myocardial infarction clots or deaths occurred before the stents broke down [28]. In 2013, Haude et al. implanted drug-coated magnesium alloy stents into 46 patients. The stents degraded after 9-12 months, and no stent thrombosis or decreased blood flow was observed within 6-12 months after implantation [29].

Magnesium alloy plate, screws and wires are considered to have great potential for bone fixation. The screws prepared by ZEK100 [30] LAE442 [31] MgCa0.8 [32] and Mg-Y-RE-Zr [33] have been used in animal experiments, and the results show that magnesium alloy has the ability to induce new bone formation. After 12 months of implantation, the adhesion of Mg-0.8Ca bone nail and bone tissue were much higher than that LAE442 and bone tissue, indicating that Mg-0.8Ca had better biocompatibility. The MAGNEZIX® bone nail made of Mg-Y-RE-Zr alloy showed the same efficacy as titanium nail in the correction of thumb eversion, and no adverse symptoms such as foreign body reaction, osteolysis and inflammatory reaction occurred 6 months after implantation.

1.3.4 Advantages and disadvantages in biomedical applications

As a biomedical implant material, magnesium alloy has its unique advantages and disadvantages. Narayanan et al. [34] summarized the advantages of

magnesium and its alloys in biomedical field in the literature: (1) Mg has no toxic effect on human body. Magnesium is an essential trace element, and the amount of magnesium in human body is relatively high. Therefore, the degraded magnesium ion does not cause any side effects; (2) The presence of Mg in the human bone system is beneficial to bone strengthening and growth; (3) Compared with other implanted metals, the density and young's modulus of Mg alloy closest to human bone can reduce the interfacial stress between bone and implanted material. In addition, Mg stimulate the growth of bone, and enhance the stability of implants; (4) Mg has better physical and mechanical properties than other metal-based or polymer-based implants and is more suitable for bone repair and replacement; (5) Mg has higher fracture toughness than ceramic biomaterials, higher strength than degradable plastics, and more suitable elastic modulus than other commonly used metallic biomaterials; (6) Mg is involved in a variety of metabolic reactions and biological mechanisms in the human body, including the formation of crystal apatite, which is important for metal bone implant materials. Mg is also a cofactor of many enzymes and stabilizes the structure of DNA and RNA. (7) Mg is important from a physiological point of view, as a deficiency of Mg promotes cardiovascular disease, and low serum levels of magnesium have been linked to an increased risk of neuropathy in patients with peripheral artery disease.

Although Mg alloy has certain advantages as a biomedical implant material, there are still many problems in the large-scale application of magnesium alloy in biological and medical fields. The implanted Mg will react with water and other ions in the body fluids to form $Mg(OH)_2$ and H_2, which the forming gas pockets that may cause delayed wound healing and tissue necrosis. At the same time, the rapid degradation of magnesium *in vivo* is accompanied by the rise of PH value in local body fluids, and local alkalinity is not conducive to the balance of physiological reactions dependent on pH value near the implant material [34].

1.4 Modification of magnesium alloy materials

At present, the most of researches on degradable medical Mg alloys are the commercial Mg alloys, and AZ series, such as AZ31 [35-37], AZ61 [38, 39], AZ91 [40, 41], etc. These Mg alloy materials have been applied in the industry due to their excellent performance in strength or corrosion resistance respectively. The elastic modulus of Mg alloy (45 GPa) is very close to that of natural bone (3~20 GPa) and the stress shielding effect can be effectively avoided [42]. It has been reported that Mg can also promote osteogenesis [35]. Therefore, Mg alloys have been widely studied as orthopedic implant materials. As orthopedic materials (such as bone plate and bone screw), Mg alloy usually needs to have higher corrosion resistance to meet the performance requirements of implant material instrument.

As a bone graft material, Mg alloy has its unique advantages. However, it has been reported that Mg alloy will be seriously degraded after implantation [43,44]. How to solve the problem of too fast degradation of Mg alloy has become the focus in research. At present, the commonly used solutions are surface modification and alloying.

1.4.1 Surface modification

(1) Electrochemical deposition

Electrochemical deposition is the process of deposition ions on the electrode surface to prepare coatings under the action of electric fields. It is an important method for surface modification of Mg alloys. Electrodeposition can be divided into inert metal (Ni, Cu) coating and calcium hydroxy-phosphate coating. At present, the research focuses on electrodeposited bioactive coatings. Electrodeposited coating has its unique advantages, and there is no residual thermal stress in the coating, and uniform coating can be prepared on a special shape or porous substrate. Song et al [45]. prepared the coating on the surface of Mg alloy by electrochemical deposition, and then soaked it in 80℃ to transform it into

stable hydroxyapatite. The coating improves the degradation rate of Mg alloys in simulated body fluids. The thin and loose shape is good for bone tissue to grow, but the bond strength between coating and substrate is weak. Gao et al [46]. obtained porous coatings by micro-arc oxidation (MAO) on the surface and prepared rod-like nano hydroxyapatite coatings on the surface by electrochemical deposition. This layer of hydroxyapatite dense uniform distribution and conducive to cell survival in the pores. Because of the membrane, the coating bond strength about times of electrochemical deposition film alone. How to further improve the bonding strength of coating and base still need a lot of research.

(2) plasma spraying

Plasma spraying technology is used to drive dc arc plasma as a heat source, such as ceramic alloy metal materials heated to molten or semi-molten state, and at high speed injection to the workpiece surface to form a solid surface method. The substrate surface can be wear-resistant, corrosion resistant and high temperature oxidation resistance.

(3) Chemical conversion film

Chemical conversion film is a chemical or electrochemical method to form metal oxide, chromate, phosphate or other refractory conversion film on the surface of a metal. Magnesium alloy conversion film mainly includes chromate conversion film, potassium permanganate conversion film, fluorozirconate conversion film, stannate conversion film, rare earth conversion film and phytic acid conversion film [47-51].

(4) Biomimetic

Bionic method is to prepare a layer of coating on the surface of magnesium and its alloy under conditions similar to physiological environment. This method simulates the deposition process of human body fluids, and the coating material prepared can better meet the requirements of human implants. Compared with other methods, the bionic method has the following advantages [52]: (1) Biomimetic mineralization enables apatite to be deposited on human tissues and its composition is closer to the quality of human bone mineral. (2) The bionic method is carried out

at room temperature, which avoids the phase transition and brittle cracking caused by high temperature, and also provides the possibility for the deposition of biological macromolecules such as proteins. (3) This process can be used to prepare coating on the surface of complex and porous materials by bionic method.

(5) Micro-arc oxidation

Micro-arc oxidation [53-57] is the formation of ceramic film dominated by matrix metal oxide under the action of instantaneous high temperature and high pressure caused by light arc discharge on its alloy surface. The characteristics of micro-arc oxidation process are as follows: (1) simple process, environmentally friendly and pollution-free electrolyte. (2) The micro-arc oxide film not only contains high temperature stable phase, but also contains a certain number of amorphous phases, so the film has higher hardness, toughness, wear resistance and corrosion resistance. (3) This process is widely applicable. (4) The micro-arc oxidation technology mostly adopts pulsed dc, so it has little influence on the mechanical properties of raw materials. (5) The micro-arc oxidation film formed is rough and porous.

1.4.2 Alloying of bone reinforcement materials

In recent years, the alloying has greatly improved the mechanical properties and corrosion resistance of purity Mg alloys. The addition of some alloy elements can refine the microstructure. In the Mg alloy matrix, the second phase is mostly the cathode phase, and the second phase is refined after the addition of alloy elements. Gu et al. [58] compared magnesium alloys composed of different metals with pure magnesium. It was found that the alloying of magnesium can improve the hardness of the alloy or reduce the corrosion rate of the alloy in the liquid. Song et al [59] compared the dissolution rates of Mg-Zn with that of pure Mg immersed in simulated body fluids, the results showed that the dissolution rates much lower than that of pure Mg, therefore, the alloying treatment can effectively reduce the corrosion rate of magnesium alloy. Hassel et al [60] pointed out that the corrosion

resistance and mechanical properties of Mg alloy could be improved. Zhang et al. showed that adding Ca into Mg-Zn-Ca could significantly refine grain, and the refinement effect was best when the mass fraction of Ca was 0.5%.

1.4.3 Research status of magnesium alloys

At present, researches on Mg alloy as a degradable medical implant material mainly focus on the following aspects: bone fixation material, bone tissue engineering, porous stent material and cardiovascular stent material [61]. Mg alloys have been tried as orthopedic implants since the early 20th century to repair damaged bone tissue [62]. Studies [63,64] have shown that Mg alloy is not suitable for use as a splint because of its fast degradation rate, but it is suitable for making screws. Mg has a positive effect on the deposition and hardening of bone tissue. In 1944, some people implant bone nails and plates with small amounts of Ca and Mg in patients with severe fractures. There was no postoperative increase in Mg content caused by inflammation of the implant. It was found that the Mg alloy implant could promote bone growth. After 6 weeks of fracture healing, the Mg alloy plate of the implant had disappeared [65]. F. whitte implanted four different Mg alloys into the thigh bone of guinea pigs, and it found that the degradation rates of different Mg alloys *in vivo* were significantly different. He added HA particles to AZ31 alloy, and the corroded materials showed uniform corrosion characteristics, and the $CaCO_3$ deposition was formed on the surface [66,67]. Zhang et al. implanted Mg alloy into rabbits and concluded that Mg alloy had an obvious effect on the osteogenesis of bone tissue [68]. Zhang [69,70] implanted four different components and magnesium alloy into rabbits, and the results showed that the degradation product (calcium phosphate) could induce the growth of new bone tissue, and the new bone could be formed between the degradation product and bone tissue. Therefore, we believe that Mg alloy has good bone induction performance. In recent years, Magnesium alloys have made progress in cardiovascular stents. Erbel, etc. used Mg alloy as a cardiovascular stent. After 4

months, the stent was completely degraded, and certain successful clinical application was achieved. Due to the slow degradation of Mg alloy in the vascular wall, the incidence of long-term vascular wall stimulation caused by intimal hyperplasia caused by traditional scaffolds is reduced [71,72].

1.5 The purpose of this research

As a biodegradable medical metal material, Mg alloy has an attractive application prospect. It is likely to be applied in clinical applications in bone plates, anastomoses, sutures and other implant devices in the next few years. However, the poor corrosion resistance of magnesium alloy materials is a very important reason that affects its service performance. For example, in the process of treating fracture healing, Mg alloy as a bone plate needs to undergo greater corrosion. However, the corrosion resistance of Mg alloy is poor, and it is easy to over degrade, leading to fracture healing failure. To solve this problem, we mainly start from the perspective of material design, and make the Mg-based materials have good corrosion resistance and degradation to meet the application requirements by designing reasonable processing technology.

In this study, a new Mg-RE alloy is designed and developed by twin-roll casting (TRC). Its microscopic characterization experiments shown that the microstructure structure is crystalline phase containing amorphous phase. This particular microstructure composed of amorphous/crystalline composite. The degradation characteristics and corrosion resistance of Mg-based materials are usually improved by adding rare earth elements. Finally, the Mg-RE sheets were processed into bone sheets and a fixation device. Through this study, we expect to the Mg-RE sheet with a special organizational structure to be potential biodegradable material. Meanwhile, it was implanted into the femur of rat to explore its prospect as biological transplantation material.

Although the crystal structure has better corrosion resistance than the amorphous structure, the microstructure of the designed Mg-RE alloy in this study is partial amorphous structure rather than all amorphous structure. In addition, the amorphous structure of the Mg-RE alloy through the whole crystal structure (Fig. 2.1). The reasons are as follows:

(1) In this study, the TRC technology has a maximum casting speed of 30rpm, which indicates that the solidification rates provided by the experimental equipment is limited. It is very difficult to process the bulk amorphous with the existing experimental equipment. However, the TRC equipment is more cost-effective than other amorphous alloy production equipment, and has better cost performance.

(2) The microstructure characteristics of the new Mg-RE alloy are amorphous structure throughout the whole crystal structure, and the distribution is relatively uniform. Previous studies showed that the amorphous structure has better strength, toughness and corrosion resistance than the crystal structure. However, the amorphous structure is more brittle. therefore, the microstructure of the amorphous and crystal composite can provide better support function as the implant material.

(3) In this study, the master alloy for the preparation of the new Mg-based alloy includes AZ31 ingot, because AZ31 alloy contains Al element. Previous studies showed that Al is an adverse element to the organism, and it is important to minimize the amount of Al. The microstructure of the new Mg-RE alloy in this study consists of amorphous spheres, and Al is enriched in the amorphous sphere and surrounded by crystal structure. Because the crystal structure is more easily degraded than the amorphous structure, the amorphous structure containing Al element is not easily degraded. As bone implant material, the amorphous sphere containing the element Al is finally surrounded by the new bone, making it part of the new bone.

The research contents of this paper are as follows:

(1) Designed of novel Mg-based materials.

The composition of Mg-based alloy was designed, the new alloy was processed by twin-roll casting (TRC) technology. The microstructure and the corrosion resistance of the material were analyzed, and the Mg-RE alloy with better comprehensive performance was obtained.

(2) Characterization of novel Mg-based materials.

The Mg-based sheet was processed by TRC, and the microstructure and corrosion resistance of the plate were characterized, and the degradation performance of Mg-based alloy as bone sheet was evaluated.

(3) Application research of Mg-based materials

The corrosion behaviour of Mg-based alloy sheet was characterized by *in vitro* electrochemical experiments and immersion experiments. The alloy sheet was fixed to the femur of rats, and the pathological reaction of the bone tissue around the femur was observed at different time periods, to characterize the performance of the sheet as a degradable fixation material.

(4) Optimization of TRC casting method for Mg-based materials.

Different TRC casting methods were used to process novel Mg-RE alloys. The microstructures, degradation properties and bone tissue reaction *in vivo* of these alloys were studied to obtain a more favorable casting method.

1.6 References

1. Yaoting Yu, Xingdong Zhang. Biomedical material. Tianjin university press; 2000.
2. Front Matter. Biomaterials: CRC Press; 2012. p. i-xviii.
3. Black J. Biological performance of materials: fundamentals of biocompatibility: CRC Press; 2005.
4. Bordjih K, Jouzeau J-Y, Mainard D, Payan E, Delagoutte J-P, Netter P. Evaluation of the effect of three surface treatments on the biocompatibility of 316L stainless steel using human differentiated cells. Biomaterials 1996; 17:491-500.
5. Hanawa T. Metals for medicine. Japan Institute of Metals, Sendai 2010.
6. Niinomi M. Metallic biomaterials. Journal of artificial organs: the official journal of the Japanese Society for Artificial Organs 2008; 11:105-10.
7. Kumagai K, Nomura N, Ono T, Hotta M, Chiba A. Dry friction and wear behavior of forged Co-29Cr-6Mo alloy without Ni and C additions for implant applications. Materials transactions 2005; 46:1578.
8. Granchi D, Ciapetti G, Savarino L, Cavedagna D, Donati ME, Pizzoferrato A. Assessment of metal extract toxicity on human lymphocytes cultured in vitro. Journal of biomedical materials research 1996; 31:183-91.
9. International A, Testing ASf, Materials. Annual book of ASTM standards. American Society for Testing & Materials; 2004.
10. Geetha M, Singh A, Asokamani R, Gogia A. Ti based biomaterials, the ultimate choice for orthopaedic implants–a review. Progress in Materials Science 2009; 54:397-425.
11. Bannon B, Mild E. „Titanium Alloys for Biomaterial Application: An Overview. Titanium alloys in surgical implants, ASTM STP 1983;796:7-15.
12. Nastac L, Gungor M, Ucok I, Klug K, Tack WT. Advances in investment casting of Ti–6Al–4V alloy: a review. International Journal of Cast Metals Research 2006; 19:73-93.
13. Balazic M, Kopac J, Jackson MJ, Ahmed W. Review: titanium and titanium alloy applications in medicine. International Journal of Nano and Biomaterials 2007;

1:3-34.

14. J.W Lee, H. S Han, K. J Han, S. J Yang. Long-term clinical study and multiscale analysis of in vivo biodegradation mechanism of Mg alloy. Proceedings of the National Academy of Sciences, 2016, 113:3, 716-721.
15. Zheng YF, Gu XN, Witte F. Biodegradable metals. Materials Science and Engineering: R: Reports 2014; 77:1-34.
16. Staiger MP, Pietak AM, Huadmai J, Dias G. Magnesium and its alloys as orthopedic biomaterials: a review. Biomaterials 2006; 27:1728-34.
17. Chen Y, Xu Z, Smith C, Sankar J. Recent advances on the development of magnesium alloys for biodegradable implants. Acta Biomater 2014; 10:4561-73.
18. Witte F. The history of biodegradable magnesium implants: a review. Acta Biomater 2010; 6:1680-92.
19. Farraro KF, Kim KE, Woo SL, Flowers JR, McCullough MB. Revolutionizing orthopaedic biomaterials: The potential of biodegradable and bioresorbable magnesium-based materials for functional tissue engineering. Journal of biomechanics 2014; 47:1979-86.
20. Witte F, Hort N, Vogt C, Cohen S, Kainer KU, Willumeit R, et al. Degradable biomaterials based on magnesium corrosion. Current Opinion in Solid State and Materials Science 2008; 12:63-72.
21. Zheng Y, Gu X. Research activities of biomedical magnesium alloys in China. JOM 2011; 63:105-8.
22. Li Z, Gu X, Lou S, Zheng Y. The development of binary Mg-Ca alloys for use as biodegradable materials within bone. Biomaterials 2008; 29:1329-44.
23. Zhang E, Yin D, Xu L, Yang L, Yang K. Microstructure, mechanical and corrosion properties and biocompatibility of Mg–Zn–Mn alloys for biomedical application. Materials Science and Engineering: C 2009; 29:987-93.
24. Zhang S, Zhang X, Zhao C, Li J, Song Y, Xie C, et al. Research on an Mg-Zn alloy as a degradable biomaterial. Acta Biomater 2010; 6:626-40.
25. Kirkland NT, Staiger MP, Nisbet D, Davies CH, Birbilis N. Performance-driven design of Biocompatible Mg alloys. JOM 2011; 63:28-34.

26. Heublein B, Rohde R, Kaese V, Niemeyer M, Hartung W, Haverich A. Biocorrosion of magnesium alloys: a new principle in cardiovascular implant technology? Heart 2003; 89:651-6.

27. Peeters P, Bosiers M, Verbist J, Deloose K, Heublein B. Preliminary results after application of absorbable metal stents in patients with critical limb ischemia. Journal of Endovascular Therapy 2005; 12:1-5.

28. Erbel R, Di Mario C, Bartunek J, Bonnier J, de Bruyne B, Eberli FR, et al. Temporary scaffolding of coronary arteries with bioabsorbable magnesium stents: a prospective, non-randomised multicentre trial. The Lancet 2007; 369:1869-75.

29. Haude M, Erbel R, Erne P, Verheye S, Degen H, Böse D, et al. Safety and performance of the drug-eluting absorbable metal scaffold (DREAMS) in patients with de-novo coronary lesions: 12 month results of the prospective, multicentre, first-in-man BIOSOLVE-I trial. The Lancet 2013; 381:836-44.

30. Reifenrath J, Angrisani N, Erdmann N, Lucas A, Waizy H, Seitz JM, et al. Degrading magnesium screws ZEK100: biomechanical testing, degradation analysis and soft-tissue biocompatibility in a rabbit model. Biomedical Materials 2013; 8:045012.

31. Wolters L, Angrisani N, Seitz J, Helmecke P, Weizbauer A, Reifenrath J. Applicability of Degradable Magnesium LAE442 Alloy Plate-Screw-Systems in a Rabbit Model. Biomedical Engineering/Biomedizinische Technik 2013.

32. Erdmann N, Angrisani N, Reifenrath J, Lucas A, Thorey F, Bormann D, et al. Biomechanical testing and degradation analysis of MgCa0. 8 alloy screws: a comparative in vivo study in rabbits. Acta biomaterialia 2011; 7:1421-8.

33. Erdmann N, Angrisani N, Reifenrath J, Lucas A, Thorey F, Bormann D, et al. Biomechanical testing and degradation analysis of MgCa0. 8 alloy screws: a comparative in vivo study in rabbits. Acta biomaterialia 2011; 7:1421-8.

34. Narayanan T. S. N. S., Park I. S., Lee M. H. Strategies to improve the corrosion resistance of microarc oxidation (MAO) coated magnesium alloys for degradable implants: Prospects and challenges[J]. Progress in Materials Science, 2014, 60: 1-71.

35. Gu X. N., Xie X. H., Li N., et al. In vitro and in vivo studies on a Mg-Sr binary alloy

system developed as a new kind of biodegradable metal [J]. Acta Biomaterialia, 2012, 8(6): 2360-2374.

36. Brar H. S., Wong J., Manuel M. V. Investigation of the mechanical and degradation properties of Mg-Sr and Mg-Zn-Sr alloys for use as potential biodegradable implant materials [J]. Journal of the Mechanical Behavior of Biomedical Materials, 2012, 7: 87-95.
37. Huan Z., Leeflang M. A., Zhou J., et al. In vitro degradation behavior and cytocompatibility of Mg-Zn-Zr alloys[J]. Journal of Materials Science: Materials in Medicine, 2010, 21(9): 2623-2635.
38. Zhang B., Hou Y., Wang X., et al. Mechanical properties, degradation performance and cytotoxicity of Mg-Zn-Ca biomedical alloys with different compositions[J]. Materials Science and Engineering: C, 2011, 31: 1667-1173.
39. Xu Z, Smith C, Chen S, et al. Development and microstructural characterizations of Mg-Zn-Ca alloys for biomedical applications[J]. Materials Science and Engineering: B, 2011, 176(20): 1660-1665.
40. Hort N., Huang Y., Fechner D., et al. Magnesium alloys as implant materials – Principles of property design for Mg-RE alloys[J]. Acta Biomaterialia, 2010, 6(5): 1714-1725.
41. Li Y., Wen C., Mushahary D., et al. Mg-Zr-Sr alloys as biodegradable implant materials[J]. Acta Biomaterialia, 2012, 8(8): 3177-3188.
42. Hermawan H., Dubé D., Mantovani D. Developments in metallic biodegradable stents[J]. Acta Biomaterialia, 2010, 6(5): 1693-1697.
43. Ascencio M., Pekguleryuz M., Omanovic S. An investigation of the corrosion mechanisms of WE43 Mg alloy in a modified simulated body fluid solution: The influence of immersion time[J]. Corrosion Science, 2014, 87: 489-503.
44. Li wei. Preparation technology and properties of biodegradable rare-earth magnesium alloy stent seamless tubes [D]. Chongqing: chongqing university, 2011.
45. Liu tong. Biodegradation of medical magnesium alloys [D]. Guangzhou: south China university of technology, 2011.
46. Hofstetter J., Martinelli E., Pogatscher S., et al. Influence of trace impurities on the in

vitro and in vivo degradation of biodegradable Mg-5Zn-0.3Ca alloys[J]. Acta Biomateriallia, 2015, 23: 347-353.

47. Nene S. S., Kashyap B. P., Prabhu N., et al. Microstructure refinement and its effect on specific strength and bio-corrosion resistance in ultralight Mg-4Li-1Ca (LC41) alloy by hot rolling[J]. Journal of Alloys and Compounds, 2014, 615: 501-506.
48. Gu CD, Lian JS, Li GY, Niu LY, Jiang ZH. Electroless Ni–P plating on AZ91D magnesium alloy from a sulfate solution. Journal of Alloys and Compounds. 2005; 391(1-2): 104-109
49. Umehara H, Takaya M, Terauchi S. Chrome-free surface treatments for magnesium alloy. Surface and Coating Technology. 2003; 169-170: 666-669
50. Zhang Y, Yan C, Wang F, Lou H, Cao C. Study on the environmentally friendly anodizing of AZ91D magnesium alloy. Surface and Coating Technology. 2002; 161(1): 36-43
51. Gonzalez-Nunez MA, Nunez-Lopez CA, Skeldon P, Thompson GE, Karimzadeh H, Lyon P, et al. A non-chromate conversion coating for magnesium alloys and magnesium-based metal matrix composites. Corrosion Science. 1995; 37(11): 1763-1772
52. Hu T., Xiao W. L., Wang F., et al. Improving tensile properties of Mg-Sn-Zn magnesium alloy sheets using pre-tension and ageing treatment[J]. Journal of Alloys and Compounds, 2018, 735: 1494-1504.
53. Chiu L-H, Chen C-C, Yang C-F. Improvement of corrosion properties in an aluminum-sprayed AZ31 magnesium alloy by a post-hot pressing and anodizing treatment. Surface and Coating Technology. 2005; 191(2-3):181-187.
54. Hsiao HY, Tsung HC, Tsai WT. Anodization of AZ91D magnesium alloy in silicate-containing electrolytes. Surface and Coating Technology. 2005; 199(2-3): 127-134.
55. Hsiao HY, Tsai WT. Characterization of anodic films formed on AZ91D magnesium alloy. Surface and Coating Technology. 2005; 190(2-3): 299-308
56. Sharma AK, Rani RU, Mayanna SM. Thermal studies on electrodeposited black oxide coating on magnesium alloys. Thermochimica Acta. 2001; 376(1): 67-75
57. Skar JI. Corrosion and corrosion prevention of magnesium alloys. Materials and

Corrosion. 1999; 50: 2-6

58. Gu X. N., Zheng Y. F., Cheng Y., et al. In vitro corrosion and biocompatibility of binary magnesium alloys[J]. Biomaterials, 2009, 30(4): 484-498.
59. Su xin. First principle calculation and microstructure properties of rare earth magnesium alloy [D]. Shanghai: Shanghai jiao tong university, 2013.
60. Chen xingwei, wu jianhua, wang jia, et al. Research progress on influencing factors of galvanic corrosion [J]. Corrosion science and protection technology, 2010, 22(4): 363-366.
61. Song guangling. Corrosion and protection of magnesium alloy [M]. Beijing: chemical industry press, 2006, 4.
62. Li J. R., Jiang Q. T., Sun H. Y., et al. Effect of heat treatment on corrosion behavior of AZ63 magnesium alloy in 3.5 wt.% sodium chloride solution[J]. Corrosion Science, 2016, 111: 288-301.
63. Jia J., Fan J. F., Xu B. S., et al. Microstructure and properties of the super-hydrophobic films fabricated on magnesium alloys[J]. Journal of Alloys and Compounds, 2013, 554: 142-146.
64. Kang Z. X., Sang J., Shao M., et al. Polymer plating on AZ31 magnesium alloy surface and film evaluation of corrosion property[J]. Journal of Materials Processing Technology, 2009, 209(9): 4590-4594.
65. Huang n. study on biodegradable magnesium and magnesium alloy coronary stents [D]. Tianjin: hebei university of technology, 2009.
66. Jiang J. H., Ma A. B., Saito N. B., et al. Improving corrosion resistance of RE-containing magnesium alloy ZE41A through ECAP[J]. Journal of Rare Earths, 2009, 27(5): 848-852.
67. Orlov D., Ralston K. D., Birbilis N., et al. Enhanced corrosion resistance of Mg alloy ZK60 after processing by integrated extrusion and equal channel angular pressing[J]. Acta Materialia, 2011, 59(15): 6176-6186.
68. Song G., Xu Z. The surface, microstructure and corrosion of magnesium alloy AZ31 sheet[J]. Electrochimica Acta, 2010, 55(13): 4148-4161.
69. Gui Z. Z., Kang Z. X., Li Y. Y. Mechanical and corrosion properties of Mg-Gd-Zn-

Zr-Mn biodegradable alloy by hot extrusion[J]. Journal of Alloys and Compounds, 2016, 685: 222-230.

70. Zhang Y, Li J X, Li J Y. Microstructure, mechanical properties, corrosion behavior and film formation mechanism of Mg-Zn-Mn-x Nd in Kokubo's solution[J]. Journal of Alloys and Compounds, 2018, 730: 458-470.
71. Zhang L., Zhu S., Han Y., et al. Formation and bioactivity of HA nanorods on micro-arc oxidized zirconium[J]. Materials Science and Engineering: C, 2014, 43: 86-91.
72. Zhao Q. M., Guo X., Dang X. Q., et al. Preparation and properties of composite MAO/ECD coatings on magnesium alloy[J]. Colloids and Surfaces B: Biointerfaces, 2013, 102: 321-326.

Chapter 2 The microstructure, composition design and experiment methods of Mg-based alloy

In this chapter, the purpose is to provide a description of the design and select experimental methods of Mg-based alloy employed in this thesis work, in more detail than could be necessarily found in subsequent chapters. Special attention is devoted towards details that may be considered necessary if the work is to be reproduced or continued in future studies.

2.1 The microstructure of Mg-based alloy design

2.1.1 The microstructure of amorphous / nanocrystalline alloy

Considering the environmental impact of modern industry on sustainable development, the new materials and new processes are expected, and many researchers devote themselves to these fields. It has been clarified that nanocrystalline alloys have new atomic configurations which are differ from those of crystalline alloys. These features have facilitated the appearance of various characteristics, such as good mechanical properties, unique chemical and physical properties which have not been obtained from conventional crystalline alloys [1]. It's worth noting that an amorphous/ nanocrystalline structure (Fig. 2.1), in which the atoms have short-range arranging or are no crystalline defects, like gain boundaries or dislocations. The previous studies [2,3] showed that amorphous/nanocrystalline structure alloys have much higher corrosion resistance than crystalline alloys due to the absence of grain boundaries and second phases. In this study, the biodegradability of the designed Mg-based alloys may be improved if they approach the amorphous/nanocrystalline microstructure. The reasons for the design of such microstructure in this study are described in detail in Chapter 1.5.

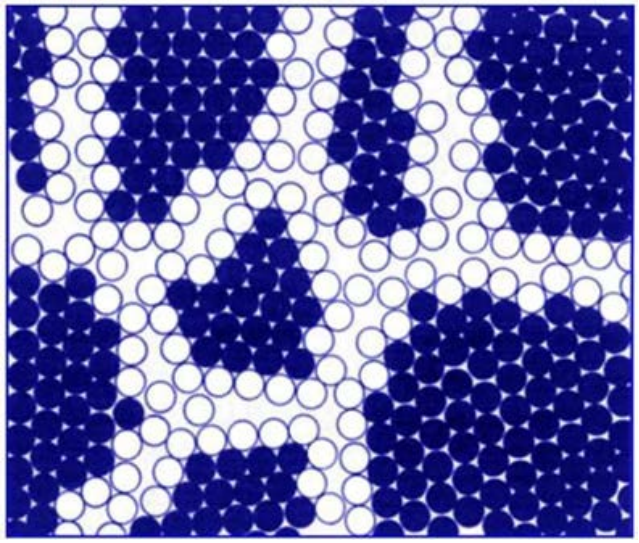

Fig. 2.1 Schematic illustration of microstructure characteristic of amorphous / nanocrystalline phase and atomic structure of a two-dimensional nanocrystalline material. Atoms (hexagonal arrays) in the centers of the —crystals are indicated in filled circles. The ones in the boundary core regions are represented by open circles [4].

2.1.2 Rapid solidification in producing amorphous / nanocrystalline alloys

Amorphous alloys have been produced by rapidly solidifying metallic melts at cooling rates of about 10^6 K·s^{-1} more than half a century ago. The ability to produce amorphous/ nanocrystalline materials with excellent mechanical, chemical and magnetic properties through quench solidification has led to the development of various quench solidification technologies.

Rapid solidification is widely reported as a non-equilibrium process, the extent of departure from equilibrium being a direct function of the increase in solidification rate [5]. A schematic description of the effect of solidification rate on microstructure of alloys is given in Fig 2.2. Using various processes, quenching rates spanning several order of magnitude can be achieved. Increasing the solidification rate, a progressive refinement of the microstructure is generally observed. Composition gradients are reduced and the system evolves towards a single solid phase [6].

With proper control of the solidification rate, it is possible to tailor the microstructure and/or to select the solidification path. The new phases and microstructures can show significantly improved properties or can be used as precursor for controlled phase transformations.

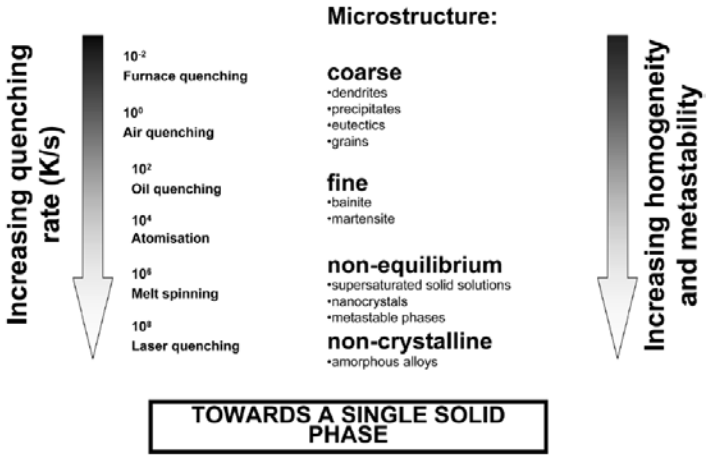

Fig. 2.2 Schematic description of the effect of solidification rate on microstructure of alloy systems [6].

2.1.3 Rapid solidification of twin roll casting technique

In 1970, after Duwez's seminal discoveries, a twin roll casting (TRC) technique for preparing uniform films of metastable phases was taken out by Chen and Miller [7]. And to date, this technique in producing metallic glass ribbons is almost still limited to laboratory scale studies [8-14]. It turns out that TRC is an available process for producing amorphous alloy sheets with a wide range of cooling rates. Nevertheless, most of the studies so far are based on horizontal type twin-roll casters.

Twin roll casting is a rapid solidification process with high temperature gradient combined with thermal flow and rolling deformation in the casting region. Compared with the traditional horizontal continuous casting process, the vertical TRC process can obtain a higher casting speed and thinner alloy sheet, so the vertical TRC process casting Mg-based alloy sheet was adopted in this research.

In this research, the vertical two-roll continuous caster in Saitama Institute of Technology [15, 16] was used as experimental equipment. The characteristics of Mg-based

alloy sheets produced by vertical TRC was studied. The vertical twin roll caster and the schematic diagram of casting process is shown in Fig. 2.3, and the specification of the vertical twin roll caster is listed in Table 2-1.

Although higher cooling rates can be achieved using the vertical TRC process, the ability of the system to reach metastable equilibrium is relative and it has great relations with the element composition and other factors.

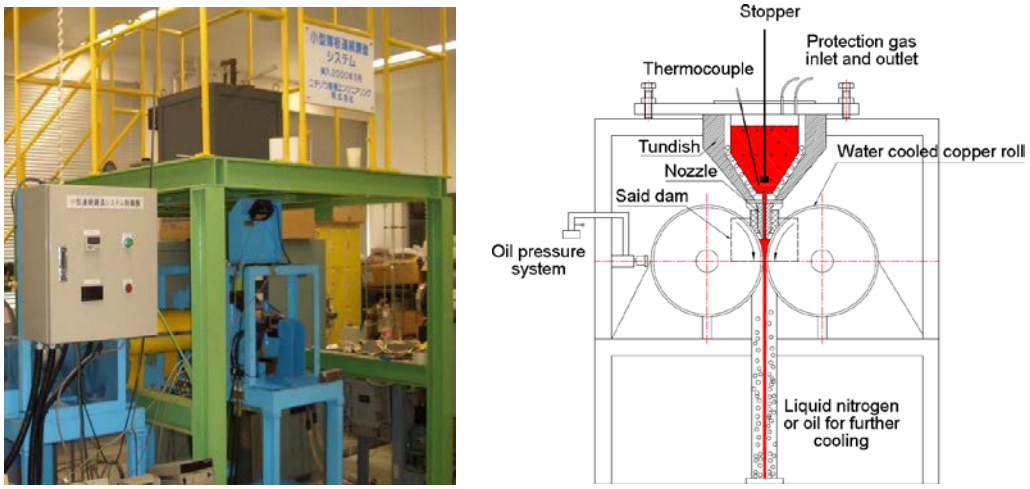

Fig. 2.3 The vertical twin roll caster of Saitama Institute of Technology and the schematic diagram of casting process.

Table 2-1 Specification of vertical pilot twin roll caster

Items	Specification	Remark
Roll diameter	300 mm	Copper Chromium alloy
Roll width	100 mm	
Drive motor	AC 5 kW	Variable Frequency
Casting speed	6~30 rpm	
Strip thickness	0.5~4 mm	
Separating force	0-10000 N	
Nozzle	Slot type	Refractory<1000 ºC
Side dam		Refractory<1000 ºC
Protection gas	SF_6 10% + CO_2 90%.	

2.2 The composition of Mg-based alloy design

There are many standards and models for designing alloy components that have glass (amorphous) phase forming properties. Most of these methods are based on the analysis of a large number of experimental data or based on experience, not applicable to all alloy systems.

2.2.1 The glass forming ability rules in alloys

According to previous research, in general, the bulk metallic glasses (BMGs) have the following four important characteristics [17]:

1. The alloy system has at least three components. This is why they are commonly referred to as multi-component alloy systems. Although the binary BMGs have been reported, the maximum diameter of their products in a fully glassy state is usually reported as 1 ~ 2 mm. Even in a glassy state of binary BMGs, a small amount of nanocrystalline precipitates dispersed in the glassy matrix can be observed.
2. The BMGs can be produced at a slower solidification rate, usually 10^3 K s^{-1} or less. The reported minimum solidification rate is 0.067 K s^{-1}. In addition, the BMGs exhibit large section thicknesses or diameters, a minimum of about 1 mm.
3. A large supercooled liquid region is another character of BMGs. The difference between the glass transition temperature, T_g, and the crystallization temperature, T_x, (i.e., $\Delta T_x = T_x - T_g$) is large, usually a few tens of degrees.

Based on a large amount of data from synthetic BMGs, Inoue formulated three basic empirical rules for BMGs formation that stated as follows [18]:

1. The alloy must contain at least three components. The formation of glass becomes easier with increasing number of components in the alloy system.
2. A significant atomic size difference should exist among the constituent elements in the alloy. It is suggested that the atomic size differences should be above about 12% among the main constituent elements.

3. There should be negative heat of mixing among the (major) constituent elements in the alloy system.

Akihisa Inoue [17] had mentioned that a metallic glass should not contain any crystalline phases which is called a nanocrystalline alloy. If it contains a glass phase and a crystalline phase, it should be called a composite material.

2.2.2 Compositions of the alloys

The amorphous/ nanocrystalline alloys are characterised by an amorphous structure, from which interesting properties stem. However, their stability is moderate so that they can loose all their peculiar properties when annealed. By rapid solidification glasses can be produced in different forms (powders by gas atomisation, ribbons by means of planar flow casting, wires, surface layers and others). The range of applications and the industrial interest for amorphous alloys have been continuously growing during the last years and various materials are commercially available nowadays [19]. The major field of applications is related to the peculiar magnetic properties of Fe, Ni and Co based amorphous alloys, which represent a valid alternative to the traditional soft magnetic materials. The composition ranges of alloys that can be quenched to the glassy state depend on the production technique. Increasing the cooling rate enhances the glass forming range for a given system. The types of alloys showing good glass forming ability are summarized in Table 2-2.

In order to retain an expect structure from the melt, (1) appropriate quenching techniques must be applied, and (2) careful alloy selection must be made. Considering from the topological aspect, atomic radii of candidate alloying elements for magnesium alloys are listed in Table 2-3. Atomic size differences between the alloying elements and magnesium (aluminum) are also calculated which symbolized by ASD_{Mg} (ASD_{Al}).

Table 2-2 A selection of glass-forming alloy systems

Main components	Minor components	Examples
Late transition metal	Metalloid	Fe-B, Fe-Ni-B
Fe, Co, Ni	B, P, Si	Fe-B-Si, Co-Fe-B-Si
Early transition metal	Metalloid	Ti-Si
Ti	Si	
Early transition metal	Late transition metal	Cu-Zr, Cu-Ti
Nb, Zr, Ti	Ni,Cu	Ni-Zr, Ni-Ti
Aluminium	Rare earth-Late transition metal:	Al-La, Al-Sm, Al-Ce
Al	La, Ce, Sm, Ni, Fe	Al-Ni-Y, Al-Fe-Ce
Rare earth	Late transition metal	La-Au, Gd-Co, Gd-Fe
La, Gd	Fe, Ni, Co	La-Al-Ni
Alkaline earth	Metal	Mg-Cu-Y
Mg, Ca	Al, Cu, Y	Ca-Al

The AZ series magnesium alloy is a kind of commonly used commercial magnesium alloy. The alloy composition design considers Mg and Al as the main elements of the Mg-based alloy. According to the Inoue radius principle and Table 2-3, it can be seen that the selected elements mainly include Ca, Ge, La, Ce, Si, Ni, Sm and Gd. According to Table 2.2, the Aluminum - Rare earth – Late transition glass-forming alloy system has the most combinations of these elements. It is well kown that the rare earth (RE) element has a characteristic of so-called—scavenger effect in Mg-based alloys, and impurity elements can form less cathode intermetallic compounds with rare earth elements. In addition, it has been reported that rare-earth elements (La, Ce) can improve the corrosion resistance of Mg alloy materials [20]. Considering the above analysis, we adopted La and Ce elements in the composition design scheme.

Table 2-3 Atomic radius of some common elements used in Mg alloys

Elements	Radius / nm	ASD_{Mg} / %	ASD_{Al} / %
Mg	0.160	-	11.85
Zn	0.139	12.92	2.60
Ca	0.198	23.40	38.02
Ge	0.124	22.56	13.39
Cu	0.128	20.19	10.74
Mn	0.135	15.69	5.71
Al	0.143	10.59	-
Ti	0.146	8.73	2.08
Ce	0.183	13.95	27.45
La	0.188	17.34	31.24
Si	0.115	27.30	19.47
Y	0.180	12.50	25.82
Fe	0.127	20.63	11.90
Ni	0.124	22.50	13.29
Zr	0.160	0.08	11.90
B	0.095	40.63	33.57
Co	0.126	21.25	11.89
Sm	0.180	12.50	25.87
Gd	0.180	12.50	15.87

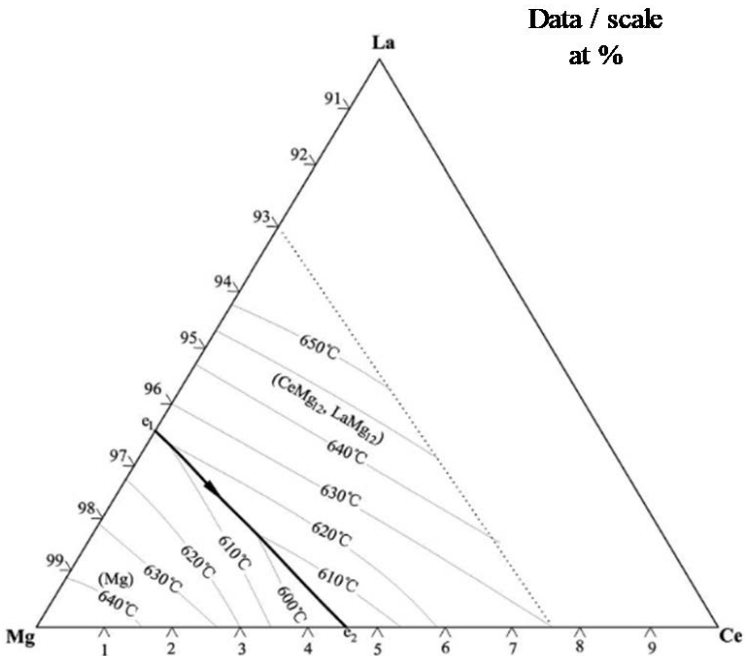

Fig. 2.4 Projection of Mg- rich angle on liquid surface of ternary phase diagram of Mg-Ce-La [21].

Through the above analysis, the Ce and La were added to the Mg-based alloy in this research, and their ternary phase diagram with magnesium (Mg-Ce-La) is shown Fig. 2.4 [21]. According to the ternary phase diagram, it is feasible to prepare the new Mg-RE (rare-earth) alloy by TRC process under the current casting conditions with the addition of rare-earth elements (Ce, La).

2.3 Preparation of Mg-based alloys with TRC

All materials in the studies were fabricated with vertical-type twin roll casting (TRC) system. The TRC experiments were carried out on a vertical-type twin roll casting mill with two identical rolls made of copper alloy. The diameter and width of both rolls are 300 mm and 100 mm respectively, and the initial roll gap was set to be 0 mm. In consideration of the separation force generated in the casting process, metal blocks were set at the two rotating rolls side to form a supporting force, minimizing the roll gap during casting process as much as possible. When the alloy melted completely, the melt was introduced into the roll gap between the left and right rolls through the asbestos casting nozzle, and the casting rolls begins to operate with 30 rpm. An oil tank was placed under the rotating rolls to avoid

further grain growth, hence the cast sheet dipped into the tank could quickly solidify as exits at the rolls. The schematic diagram and practicality illustration of TRC are shown in Fig. 2.5 (a) and Fig. 2.5 (b), respectively.

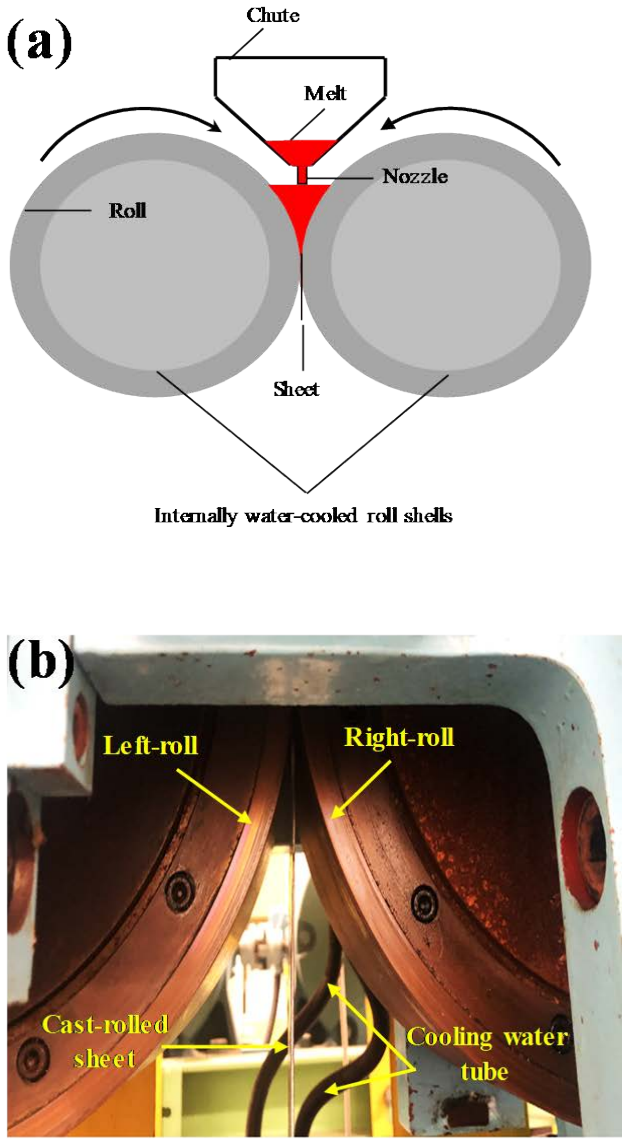

Fig. 2.5 Schematic diagram **(a)** and practicality illustration **(b)** of TRC technique.

High purity of Mg ingot (99.99%), AZ31 ingot, Mg-10La and Mg-20Ce (in wt.%) were used as raw materials. The melting process was carried out in a resistance furnace under the protection of shielding gas ($SF_6$10% and CO_2 90%). AZ31 sheets in this study were produced by melting Mg ingot and AZ31 ingot. The Mg-RE sheets in this study were produced by melting Mg ingot, AZ31 ingot, Mg-10La and Mg-20Ce.

Firstly, the Mg ingot and AZ31 ingot were placed into the resistance furnace, and the compound were heated up to 720 ℃ for 1.5 h to completely melted. Secondly, the Mg-10La and Mg-20Ce master alloys were added into the melt, then the melt temperature reduced to 700 ℃ and held for 1.5 h. It can be seen that AZ31 alloy sheets could be obtained in the first casting process, while Mg-RE alloy sheets could be obtained in the whole casting process. The final thickness of the sheets between 0.5 mm and 1.1 mm and the width of the strip rang is 25 mm to 50 mm.

2.4 Microscopic characterization

From the as-extruded Mg-based sheets, samples with a dimension of 10 × 10 × 1 mm^3 were firstly grounded with SiC papers to1200 grid, and then by diamond pastes down to #0.25 μm grade. The microstructures of the polished surfaces were observed using a field emission scanning electron microscope (FE-SEM, JMS-6301, Tokyo, Japan) and the elements distribution maps were observed by electron probe micro-analysis (EPMA, JXA-8530F, Tokyo, Japan). The alloy phases were obtained by an X-ray diffractometer (XRD, D/Max 2500 PC, Tokyo, Japan). For TEM (HF-3300, Tokyo, Japan) analysis, the focused ion beam (FIB, JIB-4500, Tokyo, Japan) was used for preparation. During the original work of sample preparation, the alloy sheet was cut into 10 mm^2 square shapes, and the thinned section thickness was about 60 μm. Square metal sheets with an area of 1.5 mm^2 were cut off from the as-cast sheet and stuck together on a Mo grid with some resin glue, and then the sample was further cut with FIB to obtain the ultimate sample thickness of 0.1 μm.

2.5 Preparation of TEM foils by focused ion beam (FIB) milling

A combination of mechanical thinning and FIB milling was used to prepare TEM foils from the size of 1.5mm×1.5mm alloy specimens. The FIB equipment used for preparing TEM samples is JIB-4500 Multi Beam system, and the sample making process is illustrated in Fig. 2.6.

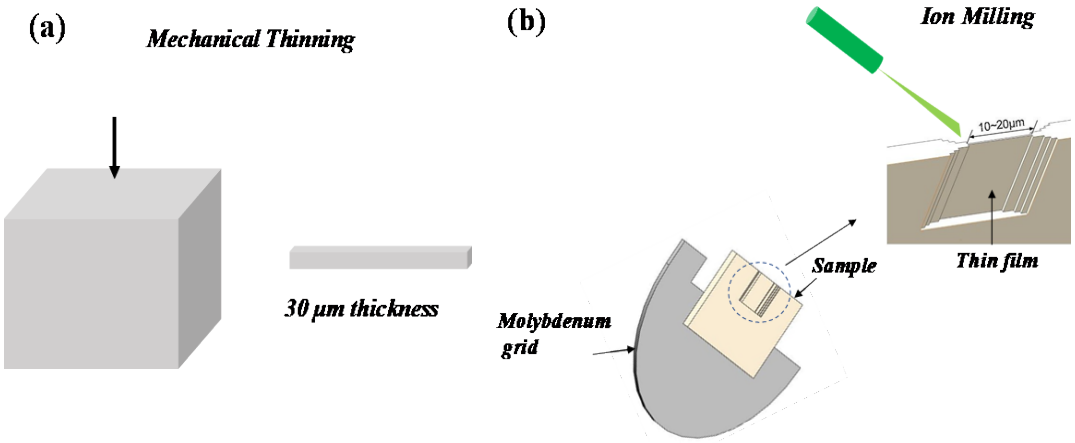

Fig. 2.6 From (a) to (b), the process flow for preparing TEM sample by mechanical thinning and ion milling.

Beginning with 400 grit SiC paper and finishing with 1200 grint SiC paper, the individual cub segments were thinned with an automated parallel-plate polisher to a final thickness of approximately 30 μm (Fig. 2.6a). The samples were transferred and glued (resin glue) on a molybdenum grid, one at a time, to the ion mill for further thinning. The milling processes by FIB method was shown in Fig. 2.6 (b). The focus of sample was milled into stair-step shape initially, finally milled down to a thickness of 0.1 μm of thin film.

2.6 Electrochemical characterization

2.6.1 Introduction of Electrochemical Workstation

Electrochemical workstation is short for electrochemical measurement system. In this research field, it is mainly used in the study of corrosion or degradation behavior of Mg-based materials.

It is important to construct a reasonable three-electrode system when using electrochemical workstation to measure corrosion information. The three-electrode system consists of two loops, one consisting of a working electrode (WE) and a reference electrode (RE), for measuring the electrochemical reaction process of the

working electrode. The other circuit consists of a working electrode (WE) and a counter (CE) electrode, which transmits electrons to form a circuit. The connection mode of the three electrodes is shown in the Fig. 2.7.

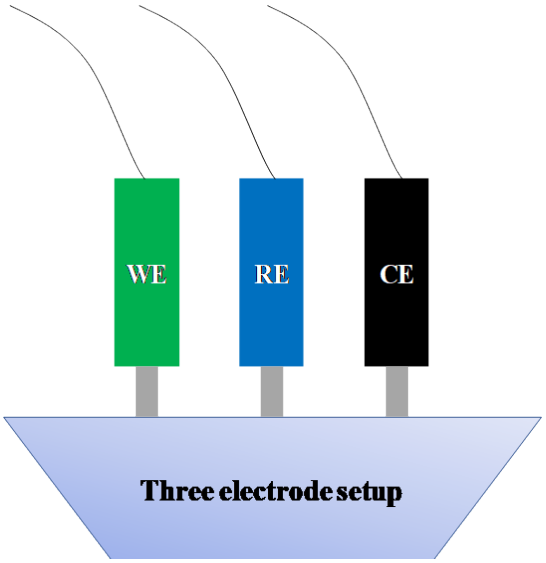

Fig. 2.7 Model diagram of two connection modes of three-electrode operation.

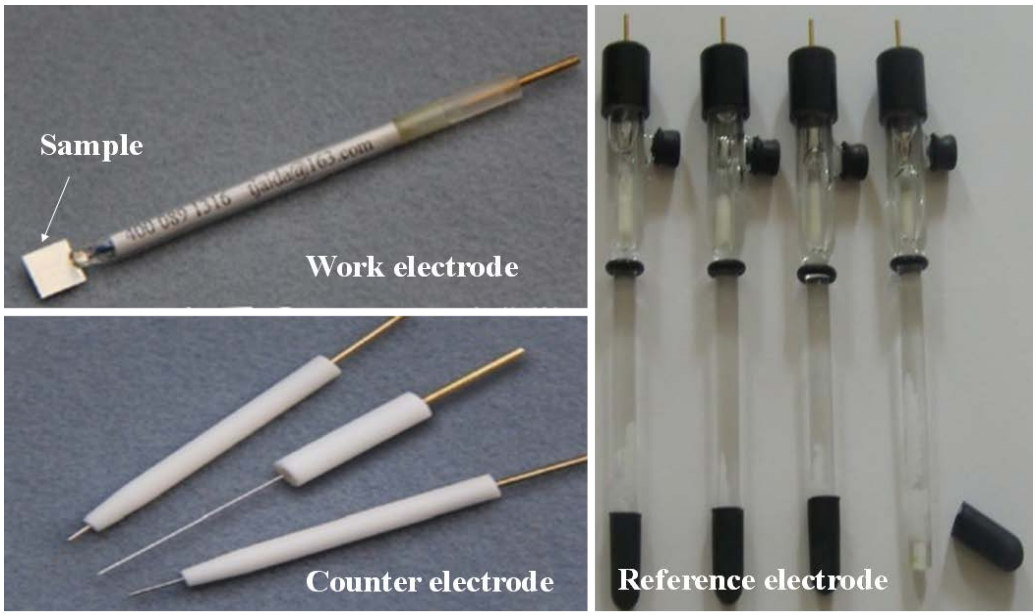

Fig. 2.8 The diagram of three-electrode.

One end of the working electrode is connected to the alloy sample in this study. The counter electrode and the working electrode form a series circuit. In addition, platinum or graphite materials are often used as counter electrodes. Common reference electrodes include saturated calomel electrode (SCE), Ag/AgCl electrode, reversible hydrogen electrode (RHE), Hg/HgO electrode, Hg/Hg_2SO_4 electrode, etc. The diagram of the three electrodes as shown in the Fig. 2.8.

2.6.2 Tafel linear extrapolation

When a metal is immersed in a corrosive medium, the metal and the medium form a corrosive system, which is called the conjugate system. The metal is anodized and the depolarizer is reduced. Take metallic M in hydrochloric acid system as an example:

Anodic reaction: $M-2e = M^{2+}$

Cathodic reaction: $H^{+}+2e = H_2$

The current density of anode reaction is expressed as i_a, and the speed of cathode reaction is expressed as i_b. When the system reaches stability, there will be no net current accumulation in the system, and the system is at a stable potential Φ_c. According to Faraday's law, there is a strict one-to-one correspondence between the current passing through the system and the amount of substances that react on the electrode, so the current density of the anodic and cathodic reaction can represent the corrosion rate of the metals. Therefore, the corrosion current of the metal is calculated to represent the corrosion rate of the metals.

The relation curve between the polarization potential and the polarization current or polarization current density is called the polarization curve. The polarization curve is very important in the study of metal corrosion behavior. The corrosion rate can be obtained by gathering measurements in the weak polarization zone near the corrosion point. The main parameters of cathodic protection and anodic protection can also be obtained by measuring the polarization curve.

2.6.3 Electrochemical impedance spectroscopy (EIS)

Typical electrochemical processes contain some basic components, such as double layers and Faraday reaction, which can be approximated by the following model as shown in Fig. 2.9. Internal resistance **(R_Ω):** Internal resistance between electrolyte and electrode. Double layer capacitance **(C_d):** From the electrolyte of inactive ions, no chemical reaction occurred, and only change the charge distribution. Faraday impedance **(Z_f):** From the active ions in the electrolyte, redox reaction occurs and there is charge transfer.

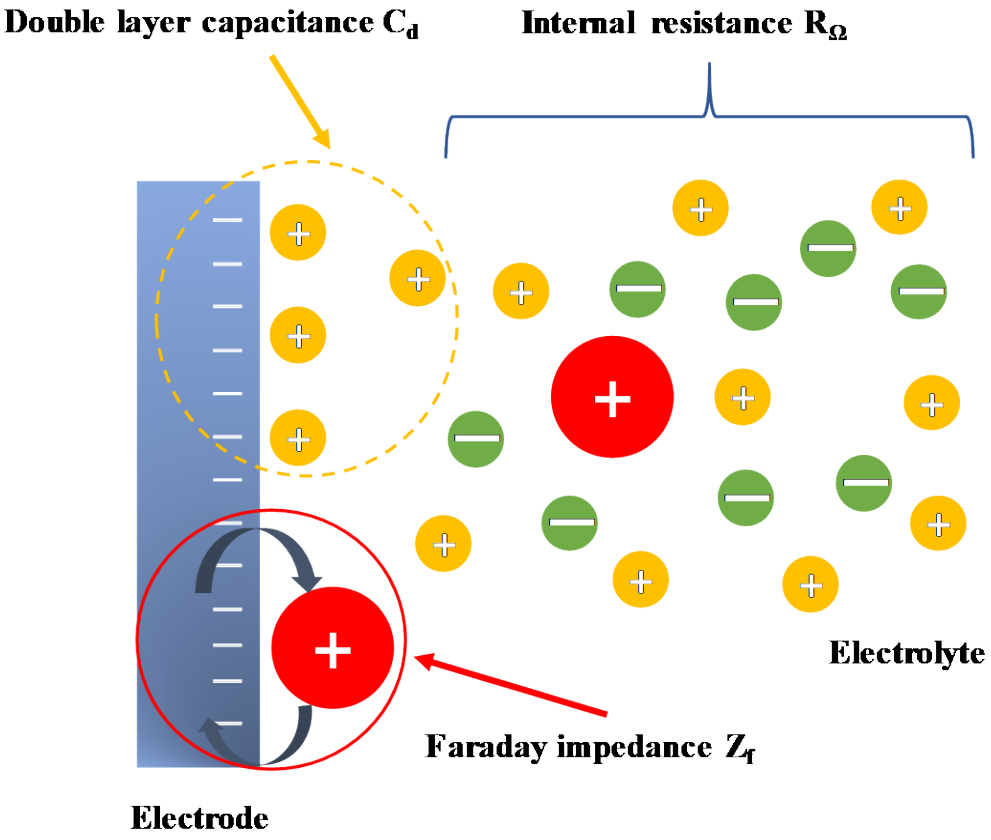

Fig. 2.9 Electrochemical reaction model.

Electrochemical reaction equivalent circuit as shown in Fig. 2.10, where, Faraday process **(Z_f)** is further divided into charge transfer resistance **(R_{ct})** and warburg impedance **(Z_w)**.

It should be noted that for the same set of spectra, more than one circuit can be found to perform fitting analysis, so it is a highly subjective method to predict electrochemical reaction process by relying on equivalent circuit.

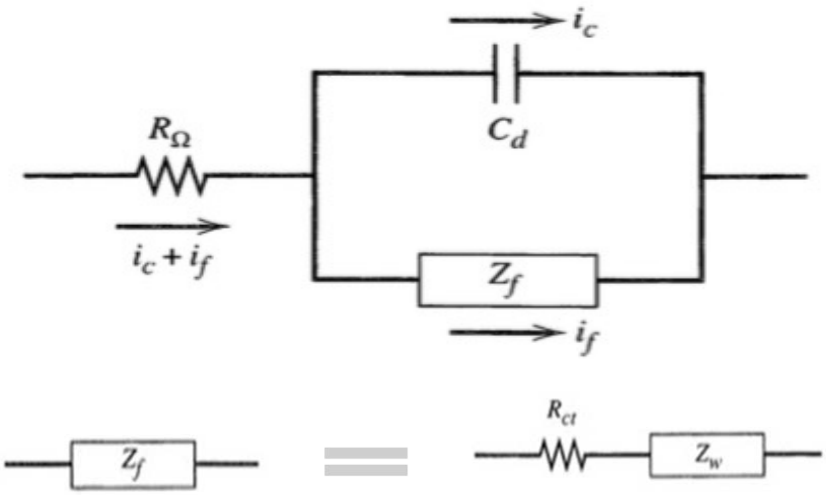

Fig. 2.10 Electrochemical reaction equivalent circuit diagram. Faraday process **(Z_f)** is further divided into charge transfer resistance **(R_{ct})** and warburg impedance **(Z_w)**.

2.7 Animals tests

In the present study, The Mg-based alloy as implants were investigated during a 16-week observation in rat femoral model. In addition, the evaluation of bone response might be influenced by bone remodeling result from sheet fixed model. This part mainly introduces the surgical methods of animal experiments.

2.7.1 Implant method

The sheet samples were machined into 15 mm × 5 mm with a thickness 0.5 mm. All surfaces were grounded with SiC papers up to 1200 grid in order to ensure surface flatness and roughness. The Ti and Mg screws (4.5 mm in length, with a shaft diameter of 3.2 mm) were selected to immobilized the Ti, and the casting-rolled sheets respectively. The implant device as shown in Fig. 2.11. The implants were sterilized using ethylene oxide in an ultrasonic vibrator.

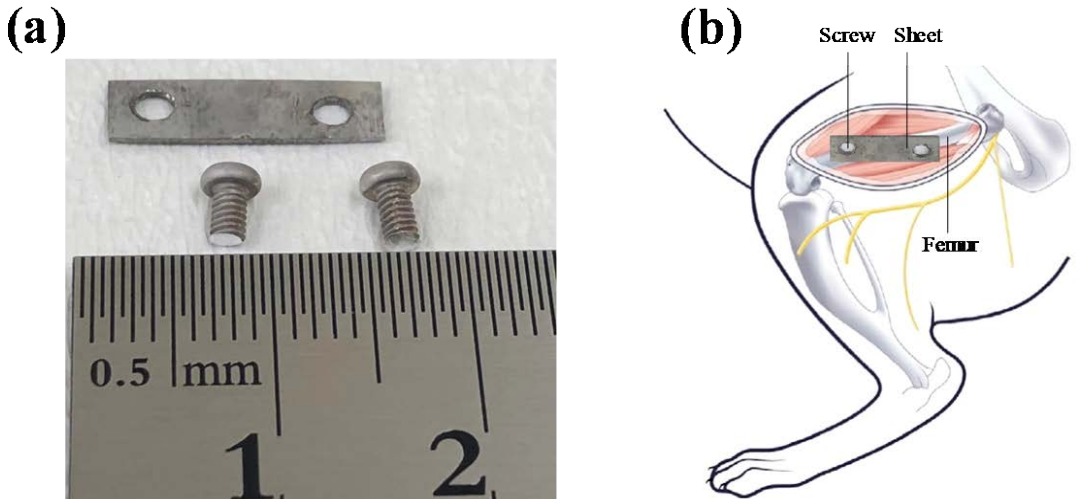

Fig. 2.11 Digital image showing implants before implantation (a); schematic diagram of cast-rolled or Ti sheets and screws fixation device with rat femoral (b).

2.7.2 Experimental animals

All animal experiments were reviewed by the Saitama Institute of Technology Animal Care and Use Committee (Grant No. 2019-5). All procedures in this study were permitted by the Animal Institutional Review Board of Saitama Institute of Technology in accordance with the guidelines of the U.S. National Institutes of Health, and performed compliance with the Guiding Principles for the Care and Use of Animals in the Field of Physiological Sciences approved by the council of the Physiological Society of Japan. The experimental white rats (Wistar; male, 16 weeks of age, 340 ± 15 g) from Tokyo University Institute of Medicine were selected for the animal study. For micro-CT analysis and histological preparation, groups of fives animals for sheet implants were used for 16 weeks postoperatively respectively.

2.7.3 Surgical procedure

Before surgical, all rats were anesthetized with isoflurane inhalation solution with the concentration 1% ~ 3%. The rats were placed in a lateral position and prepared for an aseptic operation on the right femur. Photographs of the surgical procedure are shown in Fig. 2.12.

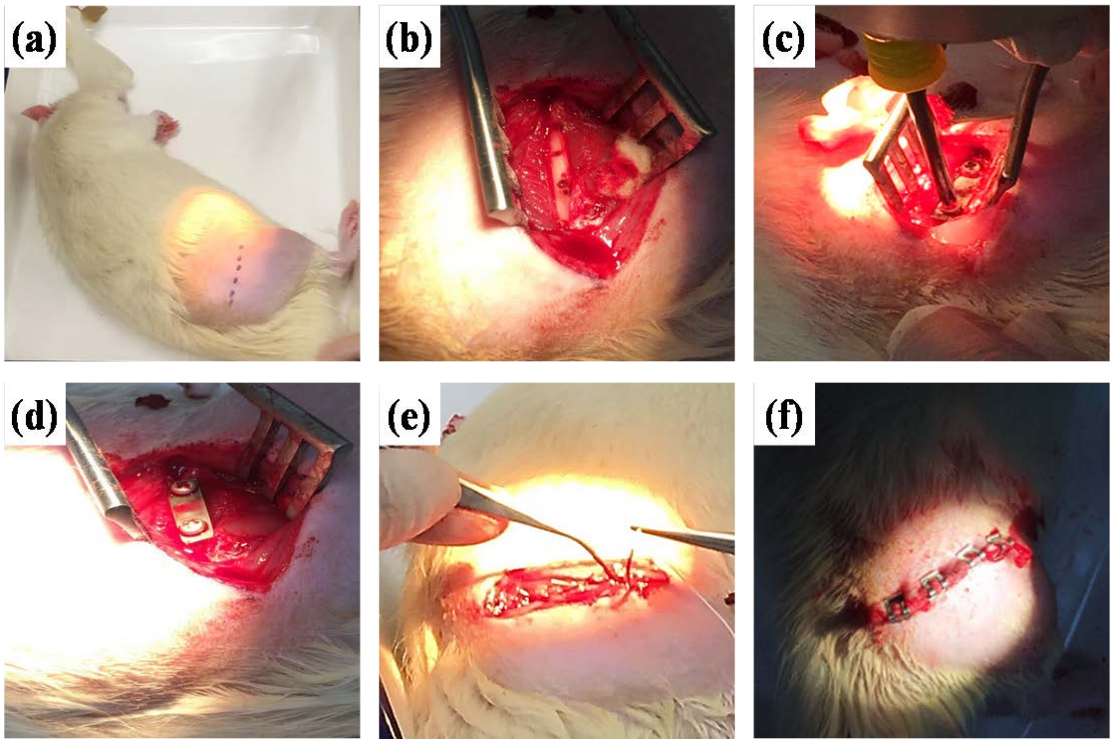

Fig. 2.12 Surgical procedure used to implant sheet implants: (a) marking indicating symbolic and the skin incision to reveal the femur; (b) screw holes being created in rat femur using electric drill; (c) sheet was fixed inside by screws; (d) after the sheet was implanted; (e) the fascia was closed with monofilament; (f) surgical site fully closed and sutured.

Firstly, the right hind limb of each rat was shaved and sterilized, and an incision of approximately 20 mm was marked in the dorsolateral right hind limbs as shown in Fig. 2.12 (a). Subsequently, the incisions were cut over the femur. Then, the region of the femur was exposed through subcutaneous dissections approach. Two screw holes (3 mm diameter) were made on both sides of femur according to the sheet geometry with sterile water cooling, as shown in Fig. 2.12 (b). The implant sheets were fixed by Mg/Ti screws (Fig. 2.12c and 2.12d). After the sheet samples were implanted, the muscles and fascia were closed with absorbable monofilament (GA03SW) (Fig. 2.12e), and the skin was closed using non-absorbable metal clips (Reflex 9) (Fig. 2.12f). Post-operative pain and distress were observed on a daily for expressions of behavioral abnormalities, food and water intake. All analgesics with an intramuscular injection of buprenorphine

hydrochloride (0.01 ~ 0.05 mg/kg; three times a day; one-week), carprofen (5 mg/kg; weekly; four weeks) and penicillin antibiotic (0.2 mg/kg; three times a day; one-week) were used to suppressed pain after the surgery.

2.8 Methods of *in vivo* test analysis

Micro-computed tomography (micro-CT) using a microtomographic imaging system (R.mCT2, Rigaku, Tokyo, Japan) at every two weeks evaluate device degradation and new bone formation. Image processing was performed by the 3D image processing software 3D Viewer and Volume Rendering Control. 3D volumes of the scanned devices were generated from acquired 2D lateral projections using Simple Viewer software (Fig. 2.13).

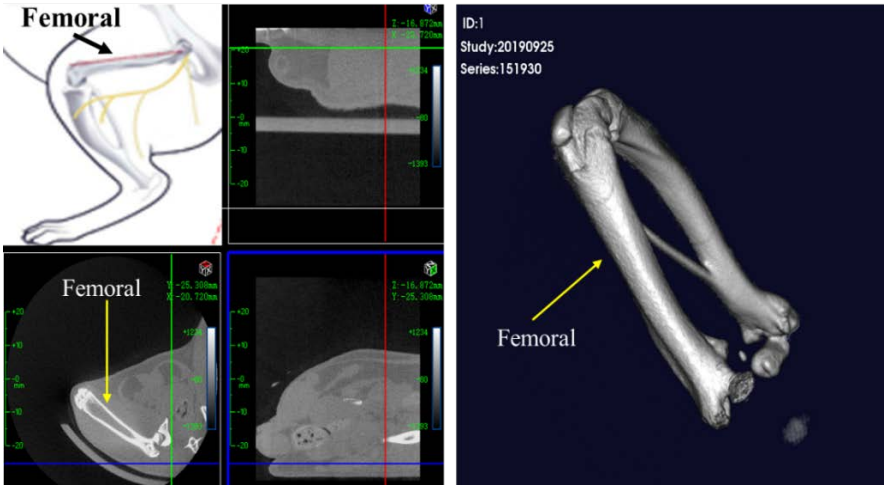

Fig. 2.13 2D images using Simple Viewer software and 3D images using 3D Viewer Volume Rendering software.

2.9 Concluding remarks

To overcome the disadvantage of rapid degradation of biological Mg alloy, a novel Mg-based alloy with amorphous/nanocrystalline structure is designed in this chapter.

According to the three experimental principles for evaluating the amorphous forming ability, and in combination with the selection of the glass forming alloy system, we selected the rare-earth elements (Ce, La) as the components of the new Mg-based alloy material. In addition, the experimental method of producing new Mg-based alloy by TRC process and the characterization method of microstructure are introduced in detail.

The corrosion performance of the new material *in vitro* can be evaluated by electrochemical experiments. Animal experiment program was designed, and the process of material implantation in animals was introduced, as well as the means of evaluating the effect of new material degradation on bone *in vivo*.

Following the above, the experimental principles and methods involved in this study are described in detail for the convenience of understanding the experimental data and the conclusions in the following research.

2.10 References

1. Inoue A, Hashimoto K. Amorphous and nanocrystalline materials: Preparation, properties, and applications [M]. Springer-Verlag Berlin Heidelberg, 2001.
2. H.F. Li, Y.F. Zheng, Recent advances in bulk metallic glasses for biomedical applications, Acta biomater. 36 (2016): 1-20.
3. H. Wang, D. Ju, H. Wang, Preparation and Characterization of Mg-RE Alloy Sheets and Formation of Amorphous/Crystalline Composites by Twin Roll Casting for Biomedical Implant Application, Metals, 9 (10), 1075.
4. Gleiter H. Nanocrystalline materials [J]. Progress in Materials Science, 1989, 33(4): 223-315.
5. Boettinger, W.J. and Perepezko, J.H. (1993) 'Fundamentals of Solidification at High Rates', in Liebermann, H.H. (Ed.): Rapidly Solidified Alloys, M. Dekker, New York, pp.17–78.
6. Baricco, M., Bosco, E., Olivetti, E., Palumbo, M., Rizzi, P., Stantero, A., & Battezzati, L. Rapid solidification of alloys. International Journal of Materials and Product Technology, 2004, 20(5-6), 358-376.
7. Chen H S, Miller C E. A Rapid Quenching Technique for the Preparation of Thin Uniform Films of Amorphous Solids [J]. Review of Scientific Instruments, 1970, 41(8): 1237-1238.
8. Suzuki T, Anthony A-M. Rapid quenching on the binary systems of high temperature oxides [J]. Materials Research Bulletin, 1974, 9(6): 745-753.
9. Lee J G, Park S S, Lee S B, et al. Sheet fabrication of bulk amorphous alloys by twin-roll strip casting [J]. Scripta Materialia, 2005, 53(6): 693-697.
10. Lee J G, Lee H, Oh Y S, et al. Continuous fabrication of bulk amorphous alloy sheets by twin-roll strip casting [J]. Intermetallics, 2006, 14(8–9): 987-993.
11. Oh Y S, Lee H, Lee J G, et al. Twin-Roll Strip Casting of Iron-Base Amorphous Alloys [J]. MATERIALS TRANSACTIONS, 2007, 48(7): 1584-1588.
12. Urata A, Nishiyama N, Amiya K, et al. Continuous casting of thick Fe-base glassy plates by twin-roller melt-spinning [J]. Materials Science and Engineering: A, 2007,

449–451(12): 269-272.

13. Hofmann D C, Roberts S N, Johnson W L. Twin roll sheet casting of bulk metallic glasses and composites in an inert environment [M]. US. 2013.
14. East D R, Kellam M, Gibson M A, et al. Amorphous magnesium sheet produced by twin roll casting [J]. Materials Science Forum, 2010, 654-656(1): 1078-1081.
15. D.Y. JU and T. INOUE. Simulation of Solidification and Viscoplastic Deformation in the Twin roll Continuous Casting Process. Transaction of the Japan Society of Mechanical Engineering, 1991, 57(537): 1147-1154.
16. T. INOUE and D.Y. JU. Simulation of Solidification and Viscoplastic Stresses during Vertical Semi-continuous Direct Chill Casting Process of Aluminum Alloy. International Journal of Plasticity,1992, 8(2): 161-183.
17. Suryanarayana C, Inoue A. Bulk metallic glasses [M]. CRC Press, 2010.
18. Takeuchi A, Inoue A. Calculation of Supercooled Liquid Range and Estimation of Glass-Forming Ability of Metallic Glasses using the Vogel-Fulcher-Tammann Equation [J]. Materials Transactions, 2002, 43(5): 1205-1213.
19. Suryanarayana, C. and Froes, F.H. (1993) ‘Mechanical, Chemical, and Electrical Applications of Rapidly Solidified Alloys’, in Liebermann, H.H. (Ed.): Rapidly Solidified Alloys.
20. Liu W, Cao F, Chang L, et al. Effect of rare earth element Ce and La on corrosion behavior of AM60 magnesium alloy [J]. Corrosion Science, 2009, 51(6): 1334-1343.
21. Liu C M, Zhu X R, Zhou H T. Magnesium Alloy Phase Diagram.2nd Ed. Changsha: Central South University Press, 2006.

Chapter 3 Preparation and characterization of Mg-RE by TRC for biomedical application

A new type of Mg-based metallic glass has attracted extensive attention due to its excellent corrosion resistance and favorable biocompatibility. In this chapter, an amorphous/crystalline composite Mg-RE alloy sheet was prepared by a vertical type twin roll caster (VTRC) method, and its microstructure was characterized by scanning electron microscopy (SEM), X-ray diffraction (XRD), and electron probe micro-analysis (EPMA) and transmission electron microscopy (TEM); furthermore, the corrosion behaviors of the Mg-RE alloy sheet were investigated in PBS solution using electrochemical techniques and immersion testing in a simulated physiological condition. Furthermore, it was implanted into the femur of rats to explore its prospect as biological transplantation material. Its microscopic characterization experiments show that the crystal structure is crystalline phase containing amorphous phase. Electrochemical experiments and immersion testing both showed that Mg-RE (La, Ce) sheet with VTRC has a better corrosion resistance than master alloy, and a uniform corrosion layer on the surface. In vivo, as an implant material, tests show that Mg-RE alloy sheets have better biocompatibility and induce new bone formation, and they can be expected to be utilized as implant materials in the future.

3.1 Introduction

Metallic glasses present excellent mechanical and chemical properties that are distinctive among solid metals, and are becoming a research hotspot for current studies in the field of metallic materials [1]. In the field of biological health, biomaterials are developing rapidly and improving people’s life quality. Among biomaterials, bioinert metals have been found to be mainly used in cardiovascular scaffolds, orthopedics and dental implants [2–4]. However, the characteristics of

these crystalline alloys, instance of high elastic modulus, relative low abrasion resistance, and stress corrosion cracking lead to bone stress shielding. Compared with traditional crystalline metals, metallic glass has an amorphous structure, higher strength, lower Young's modulus, better wear resistance, higher corrosion resistance, and anti-fatigue performance for some Ti-, Zr-, Fe-base systems [5,6]. Over the course of the decades, many metallic glassy alloys have been developed using a wide range of components, including Pd-, Pt-, Zr-, Mg-, Ti-, Co-, and Au-base systems. Among the various different compositions of metallic glasses, Mg-based metallic glass has been widely studied for biomedical applications.

Many amorphization techniques have been developed for metallic glasses, including gun and splat quenching [7], melt spinning [8], high-pressure die casting [9,10], copper mold casting [11], and twin roll casting (TRC). TRC has the advantages of a shorter production cycle, low production cost and lower capital investment compared with conventional techniques [12]. In 1970, following Duvez's seminal discoveries, Chen and Miller developed a TRC technique for producing metastable uniform sheets [13]. Until now, the technique for producing metallic glass strips has been almost solely confined to laboratory-scale research [14–20].

Previous studies have shown that TRC is a useful technique for preparing amorphous alloy sheets with an extensive cooling speed. However, the major research until now has been based on horizontal double roll casters. It is turns out that the heat transfer efficiency of vertical-type twin roll casting (VTRC) is higher than that of horizontal double roll casting (HTRC), and the cooling speed of VTRC is higher [21,22]. The rapid cooling speed of the alloy during the TRC process is beneficial for reducing segregation, achieving higher uniformity and expanded solid solubility, refining the microstructure characteristics [23]. It enables better utilization to be made of a variety of transition elements that have limited solid solubilities in magnesium alloy, to improve mechanical and chemical properties [24]. As mentioned above, heat transfer VTRC is more effective method for continuous production of magnesium alloy sheet than HTRC, and the VTRC

process enables achieve a wide range of variable casting speed [25], as a result, the processability and application performance of the products are improved.

However, studies of the rapid casting speed of Mg alloy sheets produced by rapid solidification technology using TRC are rare. In this study, based on the VTRC process, the Mg-RE (RE—rare-earth elements) sheets were produced on a vertical twin roll caster and then were annealed. The microstructure of the Mg-RE sheets was investigated. The corrosion behavior properties were studied. Through this study, we expect to the Mg-RE sheet with a special organizational structure to be potential biodegradable material. Meanwhile, it was implanted into the femur of rat to explore its prospect as biological transplantation material.

3.2 Materials and methods

Ingots of Mg-RE alloy were prepared by induction melting the mixture of industrial AZ31, Mg-10%La and Mg-20%Ce (wt%) master alloys in an induction furnace at 993 K for 30 min under the protection of a mixture of CO_2 and SF_6. The chemical compositions of the ingots were measured by X-ray fluorescence spectrometry, and the results are listed in Table 3-1. Fig. 2.5 is a schematic diagram of the manufacturing process for magnesium alloy sheets. The Mg-based sheets were prepared by VTRC. The roll, which had a diameter of 300 mm and a width of 100 mm, was made from a copper alloy. Twin roll casting experiments were carried out under casting conditions with a casting speed of 30 m/min and a pouring temperature 973 K. Because the casting produces separation force during the casting process, the metal block was set at the side of the moving roller to form a supporting force in order to minimize the gap between the rollers as much as possible during the casting process. Afterward, the melt of magnesium alloy flowed through a nozzle to a position between running rolls. The initial roll gap was set to 0 mm. An oil tank was set under the roll and the Mg-RE alloy sheet was completely submerged in the tank when the casting process was completed to prevent further grain growth. The final thickness of the sheets between 0.5 mm and 1.1 mm and

the width of the strip rang is 25 mm to 50 mm.

From the Mg-RE master ingots and the as-extruded Mg-RE sheets, samples with a dimension of 10 × 10 × 1 mm^3 were firstly grounded with SiC papers to1200 grid, and then by diamond pastes down to #0.25 μm grade. The microstructures of the polished surfaces were observed using a field emission scanning electron microscope (FE-SEM, JMS-6301, Tokyo, Japan) and the elements distribution maps were observed by electron probe micro-analysis (EPMA, JXA-8530F, Tokyo, Japan). The alloy phases were obtained by an X-ray diffractometer (XRD, D/Max 2500 PC, Tokyo, Japan). For TEM (HF-3300, Tokyo, Japan) analysis, the focused ion beam (FIB, JIB-4500, Tokyo, Japan) was used for preparation. During the original work of sample preparation, the alloy sheet was cut into 10 mm^2 square shapes, and the thinned section thickness was about 60 μm. Square metal sheets with an area of 1.5 mm^2 were cut off from the as-cast sheet and stuck together on a Mo grid with some resin glue, and then the sample was further cut with FIB to obtain the ultimate sample thickness of 0.1 μm.

The corrosion behaviors of the alloys were studied by potentiodynamic polarization (HZ700, Tokyo, Japan) and electrochemical impedance spectroscopy (Modulab XM, Tokyo, Japan), using a three-electrode cell comprising an auxiliary electrode of platinum counter, a reference electrode of Ag/AgCl electrode, and a working of the samples. The exposure area was 1 cm^2. After immersion for 0.5 h, electrochemical impedance tests were operated at the open circuit potential with signal amplitude of 10 mV over a frequency varying between 100,000 Hz and 0.01 Hz. After immersion for 1 h, potentiodynamic polarization was performed at a scanning rate of 1 mV/s. All electrochemical tests were conducted in PBS (phosphate buffer saline) solution at 310 K. A triplicate electrochemical test was carried out to ensure the reproducibility of the results. For immersion tests, for each sample, only one side of 1 cm^2 was exposed. Then, the samples were immersed in PBS solution at 310 K for 30 days. After immersion, the section corrosion morphologies were observed by SEM. The concentration of metal ions in the solutions were analyzed by Inductively Coupled Plasma (ICP) (ICPS-7000,

Sequential Plasma Spectrometer, Tokyo, Japan).

Table 3-1 Composition and the atomic radius of the Mg-RE alloy (atomic radius difference between Mg (Al) and other elements is symbolized by ARD_{Mg} (ARD_{Al})

Elements	Mg	Al	Si	Mn	Cu	Fe	Zn	La	Ce
at%	95.253	3.460	0.145	0.132	0.040	0.041	0.053	0.297	0.579
wt%	90.770	3.660	0.160	0.284	0.101	0.090	0.136	1.618	3.181
Radius/nm	0.160	0.143	0.134	0.132	0.128	0.126	0.139	0.187	0.182
ARD_{Mg}/%	-	10.63	16.25	17.50	20.00	21.25	13.13	16.87	13.75
ARD_{Al}/%	11.88	-	6.29	7.69	10.50	11.88	2.78	30.77	27.27

All animal experiments were approved by the University of Saitama Institute of Technology Animal Care and Use Committee (Grant NO. 2019-5). The project recognition date is May 20, 2019. 5 white rats (12 weeks of age, 0.36 ± 0.02 kg) from Tokyo University Institute of medicine were used in this study. Rats were anesthetized with isofluane and the right thighs were shaving and disinfected. The skin and muscle of thighs were carefully retracted to expose the femurs. Single screw fixation was used in this implantation experiment. Sheets were 22 × 4.8 mm^2 with a thickness of 1 mm. Screws were 5 mm in length, with an outer shaft diameter of 1.75 mm and shaft inner diameter of 1 mm. Animals were monitored daily for general behavior, movement, and food and water intake. High resolution microCT (R.mCT2, Rigaku, Tokyo, Japan) was used to assess Mg-RE sheets degradation and new bone formation.

3.3 Results and discussion

3.3.1 Microstructure characteristic

Fig. 3.1 reveals the surface morphologies and EDS analyses of the as-cast Mg-RE alloy ingot. It can be seen from Fig. 3.1 (a) that acicular intermetallic compounds crystallize in the Mg-RE alloy ingots. Fig. 3.1 (b) presents the combined EDS results, and the acicular compound crystallization in the red rectangle contains higher contents of Ce elements. Fig. 3.2 (a) presents the microstructure of the Mg-RE alloy sheet at a thickness of ~1.1 mm and a width of ~50 mm obtained at the casting speed of 30 m/min, in which the microstructure of the Mg-RE alloy sheet is characterized by dendrites of fine grains and a closely spaced secondary dendrite axis. Apart from that, as shown by the red rectangular area in Fig. 3.2 (a), it can be seen that there are portions where no appreciable crystalline features can be observed. Fig. 3.2 (c) shows the XRD patterns of the studied alloys. It can be concluded that the as-cast Mg-RE alloy sheets (Fig. 3.2a) consisted mainly of α-Mg, La-Al and Ce-Al, and it is worth noting that a broad peak appears at the angle of 20°~30°, indicating that the sample may contain both crystalline and amorphous phases.

The crystallite size of each detected phase in Fig. 3.2 (c) could be calculated using the Scherrer equation, which is expressed by $D_{hkl} = K\lambda/B_{hkl}\cos\theta$ [26], where D_{hkl} is the grain size perpendicular to the lattice planes, *hkl* are the Miller index of the planes being analyzed, K is a constant numerical factor called the crystallite-shape factor, λ is the wavelengths of the X-rays, B_{hkl} is the width of the X-ray diffraction peak in radians and θ is the Bragg angle. The calculated results are listed in Table 3-2. It turns out that the grain sizes of the detected phase are very fine. However, the X-ray tube on the line focus side is unsuitable for analyzing such a specific area without crystals, as the line focus range is 0.1~0.2 mm wide and 8~12 mm long [27].

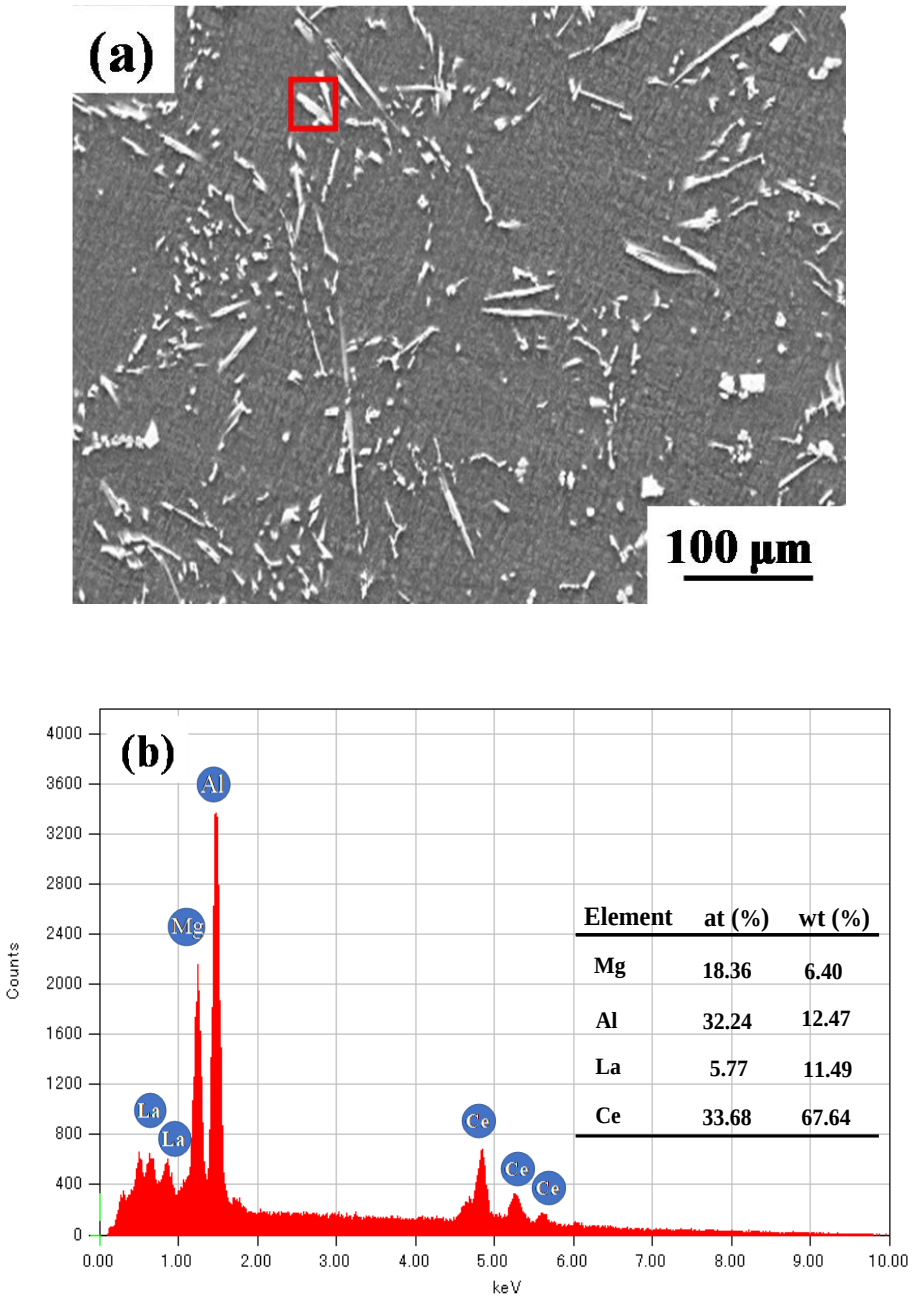

Fig. 3.1 SEM morphologies (**a**) and the precipitation by EDS analysis (**b**) of as-cast Mg-RE alloy ingot.

To solve these problems, the structure of the areas without crystals was analyzed by means of micro area X-ray diffraction. In the current operation, a collimator that was 0.03 mm in diameter was situated at the point focus side of the X-ray tube. Therefore, very small specific areas could be analyzed without reflecting unnecessary regional structural information. Fig. 3.2 (d) displays the μ-

XRD of the areas without crystals of the Mg-RE sheet. The amorphous structure was determined by a peak that does not correspond to any sharp crystalline peak. As shown in Fig. 3.2 (b) and Table 3-2, very fine grains and dendrites with closely spaced secondary dendrite axes can be found around a large amorphous region.

Fig. 3.3 shows the solute element distribution of Mg-RE with TRC. It can be seen that Mg elements are evenly distributed along the matrix, while Al/Ce/La are concentrated in amorphous areas. In addition, Al, Ce, La element segregation exists between crystal phase and the amorphous region. Meanwhile, the grain boundary is prone to segregation, because the relative atomic radius difference (ARD_{Mg}) between Mg and other elements is more than 10% [28], as shown in Table 3-1. It can also be found that Al, Ce and La elements are enriched in the amorphous phase region, which may be related to the fact that the alloy is prone to producing very stable Al-RE compounds under the solidification condition of low cooling rate. Fig. 3.4 presents the values of enthalpy of mixing ($\Delta Hmix\ [AB]$) calculated by Miedma's model for atomic pairs between major elements of Mg-RE sheet samples, in which the enthalpy of mixing between Mg-Al, Mg-La and Mg-Ce are −2 KJ/mol, −7 KJ/mol and −7 KJ/mol, respectively, while the enthalpy of mixing between Al-La and Al-Ce are −38 KJ/mol, which is greater than that between Mg and other major elements [29]. The design of Mg-RE alloy conforms to the three rules summarized by Inoue et al. [30] for the glass forming ability (GFA) of alloys: first, a multi-component system consisting of more than three major elements; second, the difference in atomic size between major elements is large (greater than 10%), and in line with the relationship of large, medium and small; third, the mixed heat between the main elements is a suitable negative value. In other words, Mg-RE alloy has good glass-forming ability.

Table 3-2 Crystallite sizes of the Mg-RE alloy sheet, calculated by Scherrer equation

(hkl)	(100)	(002)	(101)	(102)	(110)	(103)
D_{hkl}/nm	5.1	14.2	7.8	10.6	16.6	17.9

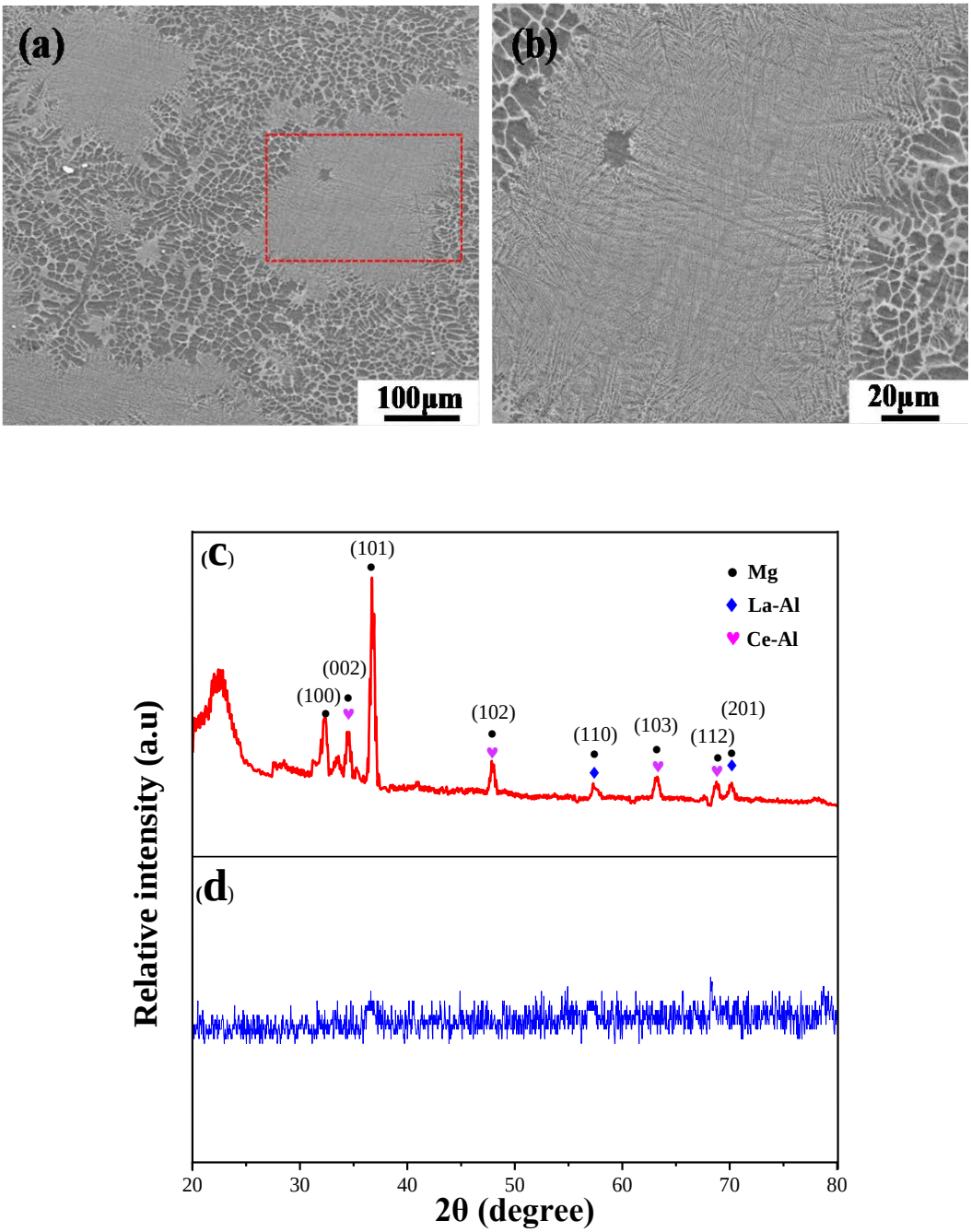

Fig. 3.2 The SEM micrographs and X-ray diffractometry (XRD) patterns of as-cast Mg-RE sheet: (**a**,**c**) SEM micrographs and XRD of the Mg-RE sheets. (**b**,**d**) SEM micrograph and μ-XRD of local amorphous region.

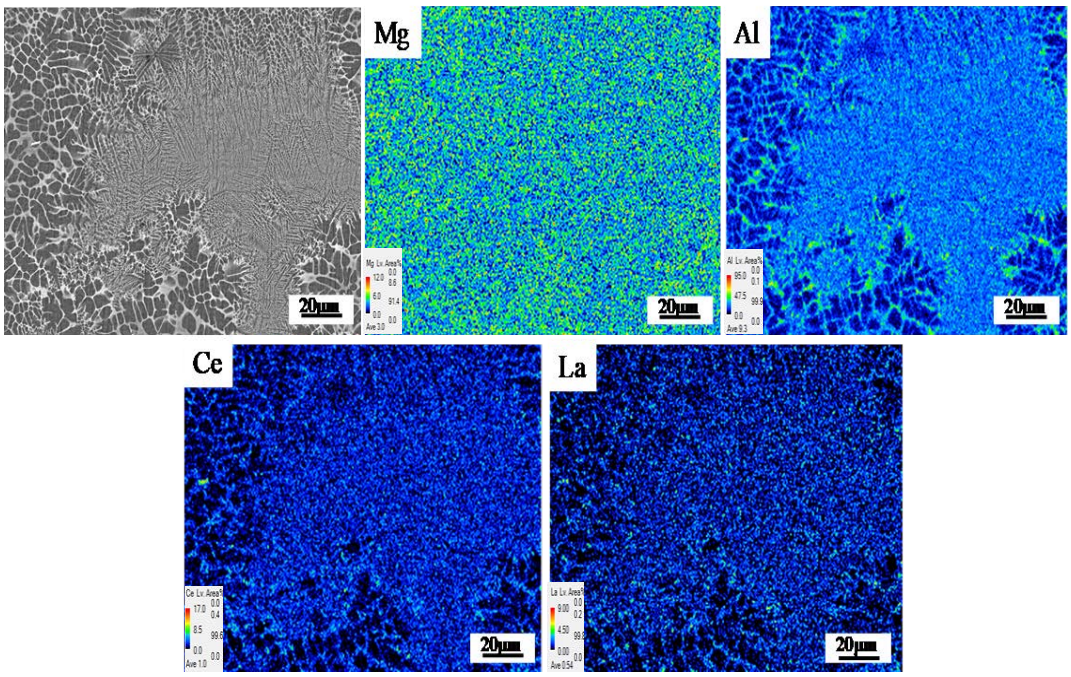

Fig. 3.3 The major element distribution of the Mg-RE alloy sheet with TRC samples.

To ascertain the amorphous phase structure, many initial specimens were prepared using the FIB technique, and TEM observation was further performed. Fig. 3.5 shows that the first step of TEM sample preparation is to find the amorphous phase on the surface of the sample in the SEM diagram, and then cut the specific phase area with FIB technology which make the cutting area length was 30~60 μm. Fig. 3.5 (a) presents the cross section of the sample is sliced by FIB technique. Since part of the sample was cut with FIB on the surface, it is easy to find the section position to be cut. The sample was cut into steps, originally, and a slice thickness of 0.1 μm was ultimately prepared, as shown in Fig. 3.5 (b). Fig. 3.5 (d) presents the TEM image and selected area diffraction pattern (SADP) of the amorphous phase, in which amorphous circular halos are not distinctly visible, and a poor crystallinity is shown, although few spots of electron diffraction exist. This may be due to the small size of the amorphous phase in the current TEM sample or the slight oxidation of the Mg-RE alloy sheet after cutting by FIB technology.

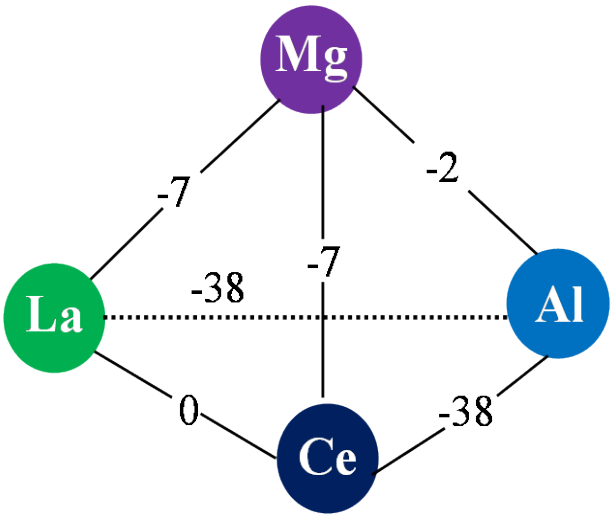

Fig. 3.4 The values of ΔH_{mix} *[AB]* (KJ/mol) calculated by Miedma's model for atomic pairs between major elements of Mg-RE sheet samples.

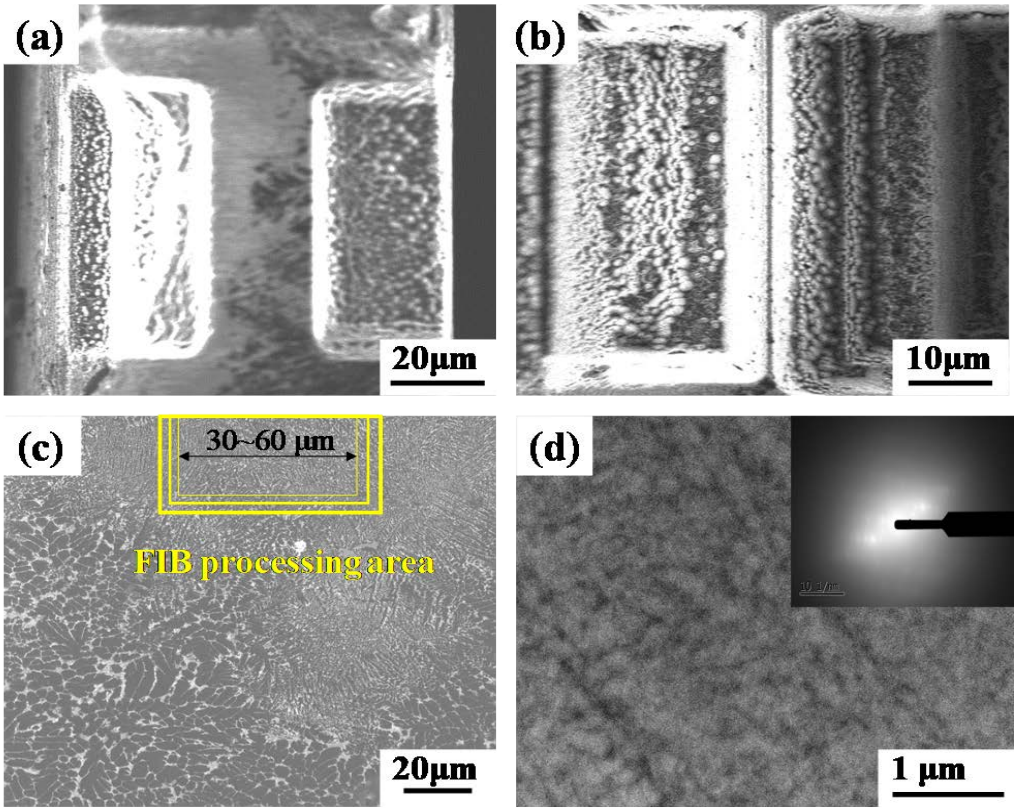

Fig. 3.5 Specimens were prepared using the FIB technique, and TEM observation performed**:** (**a**,**b**) TEM specimen by FIB technique of Mg-RE sheet with TRC; (**c**) SEM and FIB processing area on the Mg-RE sheet surface; (**d**) TEM image and high-resolution morphology.

3.3.2 Electrochemical measurements

Fig. 3.6 shows the electrochemical behaviors of the prepared Mg-RE alloy ingot sample and the sheet with TRC sample in PBS solution at 310 K. In addition, the fitting results are summarized in Table 3-3. As stated above, after the two-roll casting process, the Mg-RE alloy sheet presented a more positive potential (−1.08 $V_{Ag/AgCl}$), with comparable potentials to the Mg-RE alloy ingot (−1.37 $V_{Ag/AgCl}$). Based on electrochemical theory, in the process of electrode reaction, the ions in the solution were mainly in charge of conveying the transformation to the surface of the electrode. In the cathode area, the Mg-RE alloy dissolves into metal cation. Because the metal cation ion concentration is too high, the charge exchange process cannot be carried out as soon as possible. The cloud of ions blocks the electrodes' ability to charge, which is called polarization resistance (*Rp*). In general, the larger the Rp of the metal materials, the larger the ion cloud on the electrode surface, thus preventing charge exchange. The corrosion potential (E_{corr}) of the samples is mainly determined by the relative size between anode and cathode reaction rates, which reflects the reaction trend [31]. Furthermore, the corrosion current density (I_{corr}) shows a decreasing trend: Mg-RE sheet with TRC sample (1.51×10^{-4} A) < Mg-RE ingot sample (1.74×10^{-3} A). Lower I_{corr} indicates better corrosion resistance. Therefore, it is demonstrated that the Mg-RE sheet sample with TRC possesses a higher corrosion potential, a smaller current density, and a better corrosion resistance. Due to the influence of part of the amorphous phase being formed in the Mg-RE alloy after rapid cooling solidification by two-roll casting, the corrosion resistance was enhanced.

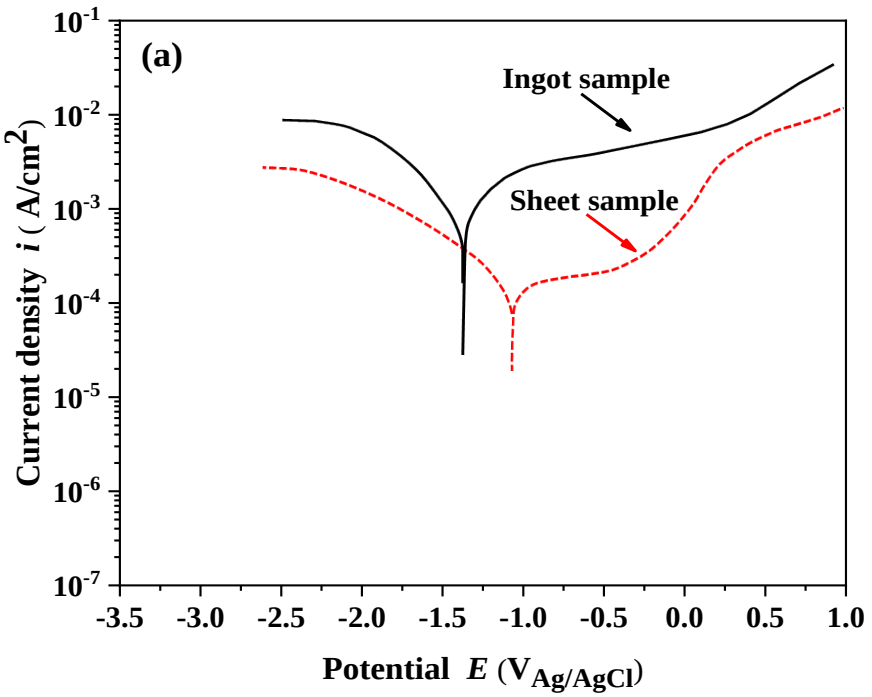
(a)
Ingot sample
Sheet sample
Current density i (A/cm2)
Potential E (VAg/AgCl)

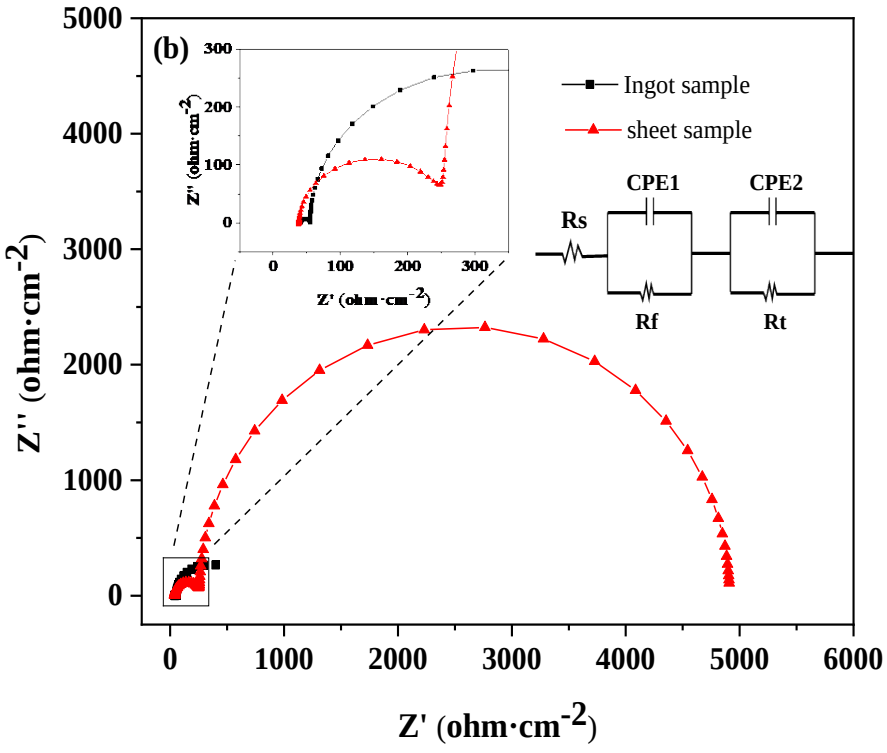
(b)
Ingot sample
sheet sample
CPE1
CPE2
Rs
Rf
Rt
Z'' (ohm·cm-2)
Z' (ohm·cm-2)

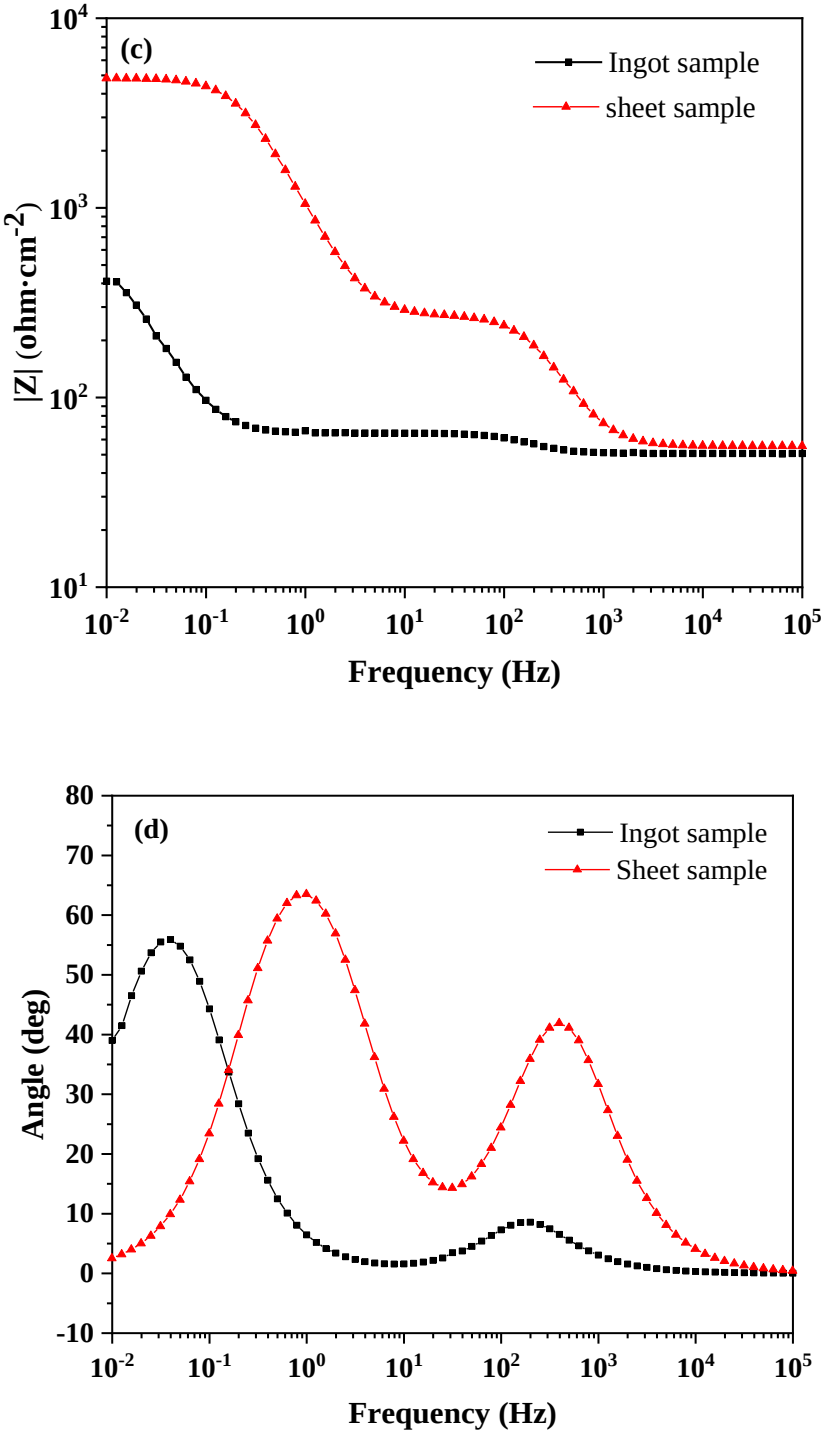

Fig. 3.6 Electrochemical behaviors of the Mg-RE alloy ingot sample and the sheet with TRC sample in PBS solution: (**a**) polarization curves; (**b**) equivalent circuit and Nyquist plots of the real part Z‘ vs. the imaginary part Z“; (**c**) Bode plots of |Z| vs. frequency; and (**d**) Bode plots of phase angle vs. frequency.

Table 3-3 Result of the electrochemical polarization tests in PBS solution

Sample	E_{corr} (V)	I_{corr} (A)	Rs ($\Omega \cdot cm^{-2}$)	Rf ($\Omega \cdot cm^{-2}$)	CPE1 (F)	CPE2 (F)	Rt ($\Omega \cdot cm^{-2}$)	Rp ($\Omega \cdot cm^{-2}$)
Ingot	−1.37	1.74×10^{-3}	50.73	22.72	7.1×10^{-5}	2.60×10^{-2}	528.37	410.12
Sheet	−1.08	1.51×10^{-4}	56.61	216.18	4.03×10^{-6}	1.57×10^{-4}	4655.12	4920.25

The electrochemical impedance data were determined for the corrosion potential in PBS and presented in Nyquist plots (Fig. 3.6b, and Bode plots Fig. 3.6c). The equivalent circuit for electrochemical impedance is shown in Fig. 3.6b. *Rs*, *Rt*, and *Rf* represent the solution resistance between the reference electrode and the working alloy sample, the resistance of charge transfer and the resistance of the corrosion product layer on the surface of the sample, respectively. Additionally, CPE1 and CPE2 illustrate the capacitance of the corrosion product layers and charge separation at the positions where hydrogen evolution increases.

In the Nyquist plots shown in Fig. 3.6 (b), the magnitude of the radius curvature has different values, showing a decreasing trend: Mg-RE ingot sample < Mg-RE sheet with TRC sample, which is also illustrated by the decreasing impedance modulus trend of the Mg-RE alloys in the curves in Fig. 3.6 (c). It is well known that the size of the Nyquist curve is an important parameter that reflects corrosion resistance. That is to say, better corrosion resistance and behavior of the metal and alloy matrix is related to higher |Z| modulus at lower frequency, which is inversely proportional to the corrosion rate of the alloy. The Bode phase plot is shown in Fig. 3.6 (d), and it can be found that the phase angles corresponding to high frequency are in a decreasing order as follows: Mg-RE sheet with TRC sample > Mg-RE ingot sample, which could be attributed to the protective properties of the surface film layers.

3.3.3 Immersion test

Fig. 3.7 presents the cross-sectional SEM micrographs of corrosion morphology of the Mg-RE alloy ingot sample and the sheet with the TRC sample in PBS solution at 310 K for 10 days. It can be observed from Fig. 3.7 (a) that the corrosion layer covered the Mg-RE ingot sample surface, which extended to the inside of the matrix with crack features. In addition, the maximum length of the corrosion cracks extending to the interior of the matrix was 30 μm, and they were distributed unevenly along the cross section of the Mg-RE ingot sample. The improved corrosion-resistance properties of the Mg-RE alloy with TRC are reflected in Fig. 3.7 (b), in that the corrosion layer is thinner and more uniform. The results of the energy spectrum analysis indicate that the content of elements in different location of Mg-RE alloy ingot is dissimilar, which is mainly connected with the corrosion behavior of the alloy in PBS solution. The mechanism of corrosion analysis is as described below.

The multiple layers of Mg-RE alloy ingot primarily consisted of C, O, Mg, Al, Ce and other elements during the immersion test in PBS solution. Mg transformed into the stable Mg^{2+} ion in the initial stages. Meanwhile, the cathodic reaction occurred on account of the galvanic corrosion between the matrix and the secondary phase, accompanied by the hydrogen evolution [32]. The cathode reaction formed a heterogeneous thin porous layer which was predominantly magnesium hydrate on the surface of the Mg-RE alloy. This prevented contact of the solution and the substrate, resulting in a decrease in the corrosion rate [33]. Moreover, the chloride ions in the PBS solution were able to easily penetrate the membrane and react with the magnesium hydrate compounds. Therefore, magnesium hydrate compounds were converted into magnesium chloride compounds, which are more likely to dissolve into magnesium ions and chloride ions [34]. The dissolution of the compound leads to a decrease in the magnesium hydrated compounds around the protective layer, leading to further dissolution of the matrix.

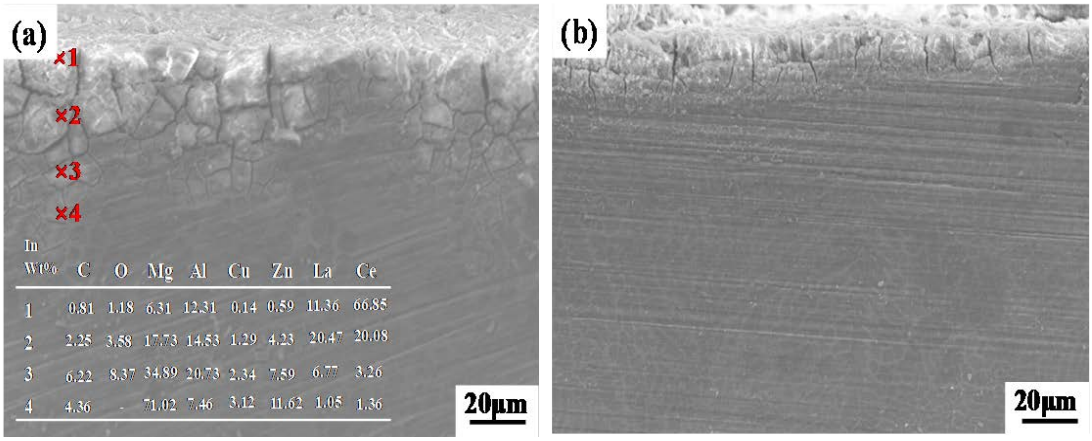

Fig. 3.7 Cross-sectional SEM micrographs of corrosion morphology of (**a**) the Mg-RE alloy ingot sample and (**b**) the sheet with TRC sample in the PBS solution at 310 K for 10 days.

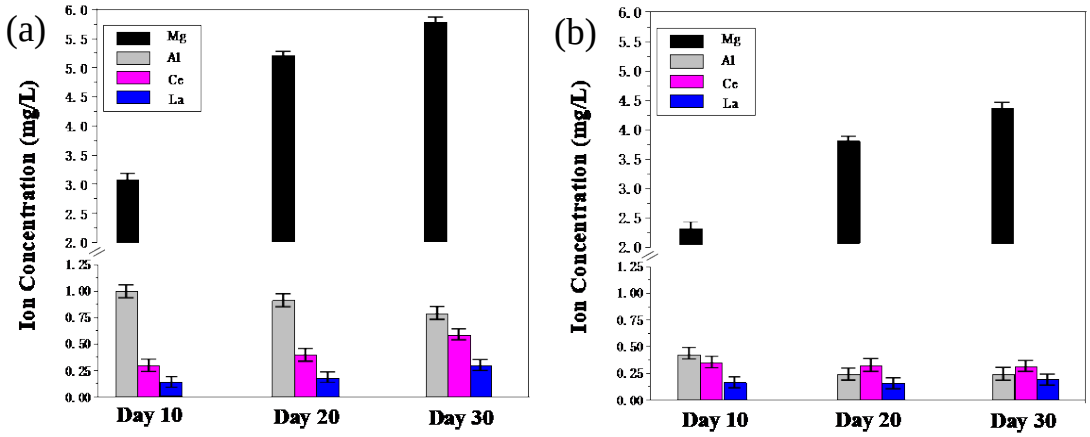

Fig. 3.8 Metallic ion concentrations of the PBS solution at 310 K with (**a**) Mg-RE alloy ingot sample and (**b**) sheet with TRC sample at day 10, day 20 and day 30 under immersion testing.

Magnesium hydrated films constituted on the surface of magnesium are generally referred to as crystals. Previous studies have found that the composition and structure of magnesium and magnesium alloy surface films can be changed using a rapid solidification process. The conversion of magnesium hydrated films from a crystal form into an amorphous film structure improves the corrosion resistance. Amorphous films have better protection than crystalline films, and films without grain boundaries are better able to resist ion motion than crystalline films [35]. The Mg-RE alloy sheet obtained by the TRC process has a unique structure

due to its crystal structure surrounding the amorphous structure, which may be the reason for the improvement of the corrosion resistance of the magnesium hydrated film.

Fig. 3.8 presents the Mg, Al, Ce and La metallic ion concentrations of the solution for (a) the Mg-RE alloy ingot sample and (b) the sheet with the TRC sample at day 10, day 20 and day 30 under immersion testing in PBS solution at a temperature of 310 K. Specifically, both alloys showed a general trend of increasing Mg ion concentration in the PBS solution with increasing immersion time from day 10, day 20 and day 30. In contrast, for Al ion concentration, both alloys showed a decreasing trend. Generally, the Mg-RE alloy ingot sample showed greater average Mg and Al ion concentration in the PBS solution at each time point—day 10, day 20 and day 30. From day 10 to day 20 after immersion, the magnesium ion concentration for the sheet sample was obviously less than the ingot sample after 10, 20 and 30 days. This may be caused by the rapid corrosion of alloys in the initial corrosion stage and then the beginning of passivation to slow down the corrosion. The decrease of aluminum in the corrosive solution may have resulted from the formation of corrosion products on the surface of the sample.

Fig. 3.8 (a) and 3.8 (b) also shows that throughout the entire 30 day culture period, the Mg-RE with TRC sample group showed significantly lower release rates of Ce and La ions than the Mg-RE alloy ingot sample, and the group showed a general trend of increasing Ce and La ion concentration with increasing immersion time, but no significant change for the Mg-RE with TRC sample group. Overall, the content of metallic ions concentrations in the corrosion solution of the Mg-RE alloy sheet produced by rapid solidification TRC method less than that of Mg-RE alloy ingot sample within the same amount of immersion time. Which is probably induced by the special microstructure formed under rapid cooling and exhibits an improved corrosion resistance.

3.3.4 In vivo implantation

The Mg-RE sheet with TRC samples was successfully inserted into the subcutaneous tissue of the rat thigh and attached to the femur with an AZ31 screw during surgery, despite the slight mismatches between the Mg-RE sheet and femur owing to manual surgical placement and the fact that there is only one screw to fix the femur and alloy sheet. Slight skin swelling was observed in the hind limbs of the rats during the visual examination of the rats during the study period. The bulge disappeared after a few days.

Fig. 3.9 reveals the surface volume of the degrading Mg-RE alloy sheet and bone growth changes, depicted using MicroCT 3D rendering after various implantation times. As can be seen from Fig. 3.9 (a) and 3.9 (c), two weeks after surgery, no new bone production was found around the Mg-RE alloy sheet and femur, and the screw between them was clearly visible. There are no obvious corrosion pits on the surface of magnesium alloy sheet. Fig. 3.9 (b) and 3.9 (d), six weeks after the surgery, new bone was formed between the Mg-RE alloy sheet and the femur. Fig. 3.9 (e) presents on the cross section of the bone–alloy joint, the new bone is generated and surrounds the original femur. The sheets are attached to the femur by new bone, which appears to be relatively stable in living organisms. In the red area shown in Fig. 3.9 (d), corrosion pits began to appear on the surface of magnesium alloy sheet after six weeks of surgery. This indicates that the films with improved corrosion resistance of Mg-RE alloy sheet began to degrade in vivo after 6 weeks.

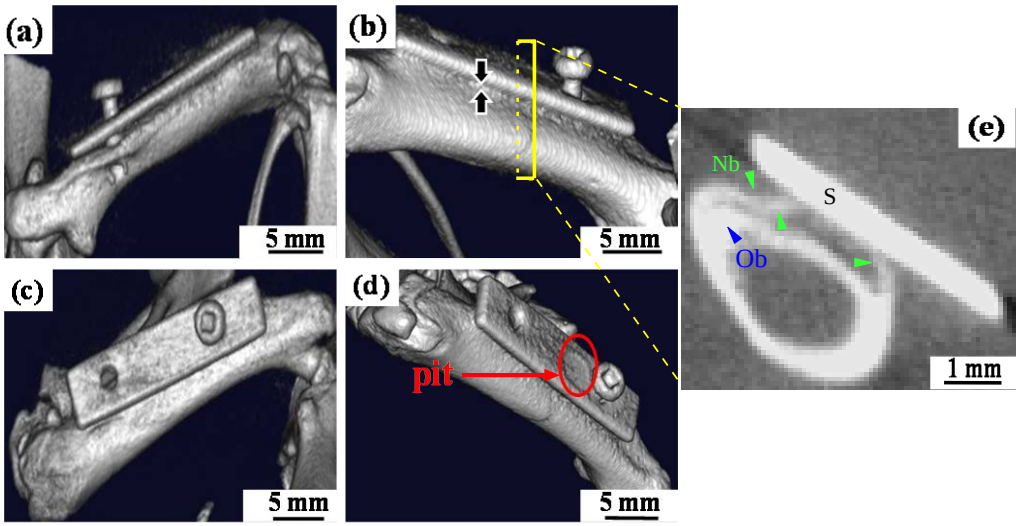

Fig. 3.9 Determination of the volume of the degrading Mg-RE alloy sheet and bone growth changes, depicted in MicroCT 3D rendering after implantation times of 2 weeks (**a**,**c**) and 6 weeks (**b**,**d**). A cross section slice of femoral-sheet contact area observed after 6 weeks (**e**) shows that the new bone (Nb is represented in green) was formed between the Mg-RE alloy sheet (S) and the original bone (Ob is represented in blue).

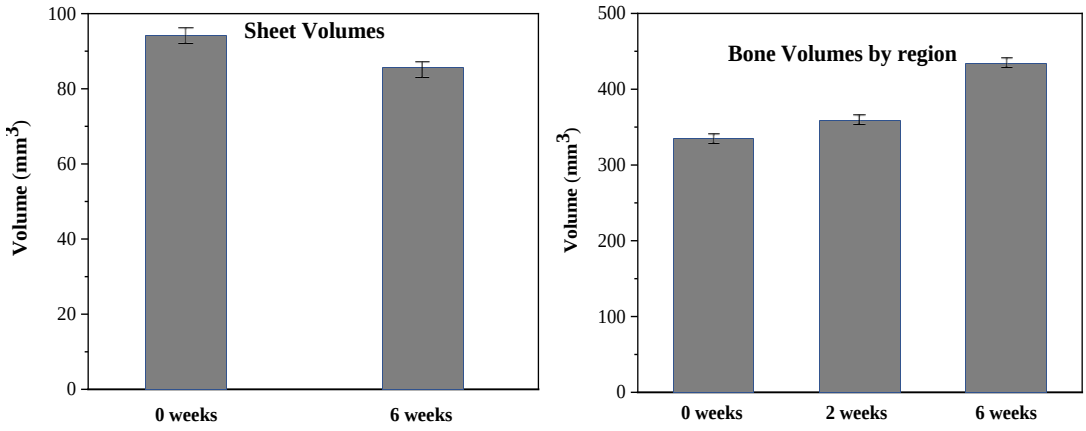

Fig. 3.10 Mg-RE sheet degradation after 6 weeks was estimated by the volume of quantification. This shows a sheet volume loss of 9.32 ± 0.86 mm^3 after 6 weeks. MicroCT 3D rendering after 2 weeks shows there was no obvious change in bone growth around the degrading Mg-RE sheet. By 6 weeks, as new bone formed between the sheet and the bone, a notable change in bone volume was observed from 2 to 6 weeks.

Mg-RE sheet degradation and femoral change were assessed by volume quantification in MicroCT 3D rendering separately as shown in Fig. 3.10. Before surgery, the volume of self-made Mg-RE alloy bone sheet was 94.79 mm^3. The Mg-RE sheet corroded, resulting in 9.32 ± 0.86 mm^3 volume loss after 6 weeks. With regard to the changes in the femur, the volume of the femur did not change significantly during the two weeks following the surgery. In fact, for some time after the surgery, the rat lost significantly more weight, the reason for this being that it took some time for the body to adapt the foreign body. After about five days, the rats returned to their normal mental state and began to eat normally. By 6 weeks, as new bone had formed between the sheet and the femur, a noticeable change in bone volume was observed from 2 to 6 weeks. The rat showed no abnormal physical or physiological responses during subsequent breeding.

Uniquely, magnesium alloy application has the potential to enhance bone formation. Several previous studies have shown that the potential performance, presenting increased bone mass, mineral apposition, and bone mineral density around magnesium alloy implants in bone [36–39]. In our present study, new bone appears in the area where the femur contacts the alloy sheet, which confirmed our findings that the Mg-RE alloy with TRC degradation can lead to the promotion of bone formation. The new bone formation is not common in absorbable polymers or permanent metal devices, thus emphasizing the unique advantages of magnesium fixtures. In this way, the degraded fixture will be gradually replaced in the future.

3.4 Concluding remarks

(1) The Mg-RE alloy sheet was prepared using a vertical-type twin-roll caster method. Its microscopic characterization experiments show that the crystal structure is crystalline phase containing amorphous phase.

(2) EPMA experiments show that Al, La and Ce elements are enriched in the amorphous phase region and the grain boundary region. However, Mg is evenly distributed throughout the microscopic region. This shows that segregation is more likely to affect Al, La and Ce elements.

(3) Electrochemical tests and immersion test results revealed that Mg-RE sheet with TRC has a better corrosion resistance than master alloy, and a uniform corrosion layer on the surface.

(4) In vivo, as an implant material, the tests show that Mg-RE alloys sheets were safe with respect to rat physical fitness and induced new bone formation; thus, they were promising for utilization as implant materials in the future.

3.5 References

1. Green, A.L.; Ma, E. Bulk Metallic Glasses: At the Cutting Edge of Metals Research. MRS Bulletin 2007, 32, 611–619.
2. Chen, Q.Z.; Thouas, G.A. Metallic implant biomaterials. Mater. Sci. R 2015, 87, 1–57.
3. Wise, D.L.; Trantolo, D.J.; Altobelli, D.E.; Yaszemsk, M.J.; Grasser, J.D. Human Biomaterials Application; Humana Press: Totowa, NJ, USA, 1996.
4. Yaszemsk, M.J.; Trantolo, D.J.; Lewandrowski, K.U.; Hasirci, V.; Altobelli, D.E.; Wise, D.L. Biomaterials in Orthopedics; Marcel Dekker Inc.: New York, NY, USA, 2004.
5. Matusiewicz, H. Potential release of in vivo trace metals from metallic medical implants in the human body: From ions to nanoparticles—a systematic analytical review. Acta Biomater. 2014, 10, 2379–2403.
6. Heary, R.F.; Parvathreddy, N.; Sampath, S.; Agarwal, N. Elastic modulus in the selection of interbody implants, J. Spine Surg. 2017, 3, 163–167.
7. Andreas, A.K.; Jörg, F.L.; Florian, H.D.T. Rapid Solidification and Bulk Metallic Glasses—Processing and Properties. In Materials Processing Handbook; CRC Press: Boca Raton, FL, USA, 2007; PP. 17-1-17-44.
8. Masumoto, T.; Maddin, R. The mechanical properties of palladium 20 a/o silicon alloy quenched from the liquid state. Acta Metall. 1971, 19, 725–741.
9. Liebermann, H.; Graham, C. Production of amorphous alloy ribbons and effects of apparatus parameters on ribbon dimensions. IEEE Trans. Magn. 1976, 12, 921–923.
10. Narasimhan, M.C. Continuous casting method for metallic strips. U.S. Patent 4,142,571. 22 October 1979.
11. A. Inoue, T. Nakamura, T. Sugita, T. Zhang, T. Masumoto. Bulky La-Al-TM (TM=Transition Metal) Amorphous Alloys with High Tensile Strength Produced by a High-Pressure Die Casting Method. Mater. Trans. JIM 1993, 34, 351–358.
12. Barekar, N.S.; Dhindaw, B.K. Twin-roll casting of Aluminum alloys—An overview. Mater. Manuf. Process. 2014, 29, 651–661.
13. Chen, H.S.; Miller, C.E. A Rapid Quenching Technique for the Preparation of Thin Uniform Films of Amorphous Solids. Rev. Sci. Instrum. 1970, 41, 1237–1238.
14. East, D.R.; Kellam, M.; Gibson, M.A.; Seeber, A.; Liang, D.; Nie, J.F. Amorphous magnesium sheet produced by twin roll casting. Mater. Sci. Forum 2010, 654, 1078–1081.

15. Lee, J.G.; Park, S.S.; Lee, S.B.; Chung, H.T.; Kim, N.J. Sheet fabrication of bulk amorphous alloys by twin-roll strip casting. Scr. Mater. 2005, 53, 693–697.
16. Oh, Y.S.; Lee, H.; Lee, J.G.; Kim, N.J. Twin-Roll Strip Casting of Iron-Base Amorphous Alloys. Mater. Trans. 2007, 48, 1584–1588.
17. Urata, A.; Nishiyama, N.; Amiya, K.; Inoue, A. Continuous casting of thick Fe-base glassy plates by twin-roller melt-spinning. Mater. Sci. Eng. A 2007, 449, 269–272.
18. Suzuki, T.; Anthony, A.M. Rapid quenching on the binary systems of high temperature oxides. Mater. Res. Bull. 1974, 9, 745–753.
19. Lee, J.G.; Lee, H.; Oh, Y.S.; Lee, S.; Kim, N.J. Continuous fabrication of bulk amorphous alloy sheets by twin-roll strip casting. Intermetallics 2006, 14, 987–993.
20. Hofmann, D.C.; Roberts, S.N.; Johnson, W.L. Twin Roll Sheet Casting of Bulk Metallic Glasses and Composites in an Inert Environment. U.S. Patent 20130025746 A1, 31 January 2013.
21. Ding, P.-D.; Pan, F.-S.; Jiang, B.; Wang, J.; Li, H.-L.; Wu, J.-C.; Xu, Y.-W.; Wen, Y. Twin-roll strip casting of magnesium alloys in China. Transactions of Nonferrous Metals Society of China, 2008, 18, s7−s11.
22. Hu, X.; Ju, D.; Zhao, H. Thermal flow simulation of twin-roll casting magnesium alloy. J. Shanghai Jiaotong Univ. 2012, 17, 479−483.
23. Luo, L.T.; Gong, X.B.; Li, J.Z.; Kang, S.B.; Cho, J.H. Microstructure and Mechanical Properties of Severely Deformed Mg-4.5Al-1.0Zn Alloy Processed by Asymmetric Rolling on Ingot and Twin Roll Cast Strip. Mater. Res. 2016, 19, 207–214.
24. Park, S.S.; Park, W.J.; Kim, C.H.; You, B.S.; Kim, N.J. The Twin-Roll Casting of Magnesium Alloys. JOM 2009, 61, 14–18.
25. Pei, Z.P.; Ju, D.Y.; Li, X. Simulation of critical cooling rate and process conditions for metallic glasses in vertical type twin-roll casting. Trans. Nonferrous Met. Soc. China 2017, 27, 2406−2414.
26. Holzwarth, U.; Gibson, N. The Scherrer equation versus the 'Debye-Scherrer equation'. Nat. Nanotechnol. 2011, 6, 534.
27. Pecharsky, V.K.; Zavalij, P.Y. Properties, Sources, and Detection of Radiation. Fundamentals of Powder Diffraction and Structural Characterization of Materials; Springer: Boston, MA, USA. 2009; pp. 107–132.
28. In-Ho Jung, Mehdi Sanjari, Junghwan Kim, Stephen Yue. Role of RE in the deformation and recrystallization of Mg alloy and a new alloy design concept for Mg–RE alloys. Scr. Mater. 2015, 102, 1–6.

29. Takeuchi, A.; Inoue, A. Calculations of mixing enthalpy and mismatch entropy for ternary amorphous alloy. Mater. Trans. JIM 2000, 41, 1372–1378.
30. Inoue, A. Stabilization of metallic supercooled liquid and bulk amorphous alloys. Acta Mater. 2000, 48, 279–306.
31. Anawati, A.; Asoh, H.; Ono, S. Effects of alloying element Ca on the corrosion behavior and bioactivity of anodic films formed on AM60 Mg alloys. Materials 2017, 10, 11.
32. Song, Y.; Han, E.; Shan, D.; Yim, C.D.; You, B.S. Corros. Sci. 2012, 60, 238–245.
33. Zhang, B.; Hou, Y.; Wang, X.; Wang, Y.; Geng, L. Mater. Sci. Eng. C 2011, 31, 1667–1673.
34. Bakhsheshi-Rad, R.; Abdul-Kadir, M.R.; Idris, M.H.; Farahany, S. Corros. Sci. 2012, 64, 184–197.
35. Makar, G.L.; Kruger, J. Corrosion of magnesium. Intern. Mater. Rev. 1993, 38, 138–153.
36. Witte, F.; Kaese, V.; Haferkamp, H.; Switzer, E.; Meyer-Lindenberg, A.; C.J. Wirth; H. Windhagen. In vivo corrosion of four magnesium alloys and the associated bone response. Biomaterials 2005, 26, 3557–3563.
37. Janning, C.; Willbold, E.; Vogt, C.; Nellesen, J.; Meyer-Lindenberg, A.; Windhagen, H.; Windhagen, F. Thorey, F. Witte. Magnesium hydroxide temporarily enhancing osteoblast activity and decreasing the osteoclast number in peri-implant bone remodelling. Acta Biomater. 2010, 6, 1861–1868.
38. Yang, J.X.; Cui, F.Z.; Lee, I.S.; Zhang, Y.; Yin, Q.S.; Xia, H.; SX Yang. In vivo biocompatibility and degradation behavior of Mg alloy coated by calcium phosphate in a rabbit model. J. Biomater. Appl. 2012, 27, 153–164.
39. Yoshizawa, S.; Brown, A.; Barchowsky, A.; Sfeir, C. Magnesium ion stimulation of bone marrow stromal cells enhances osteogenic activity, simulating the effect of magnesium alloy degradation. Acta Biomater. 2014, 10, 2834–2842.

Chapter 4 *In vivo* degradation behaviour and bone response of cast-rolled alloy in rat femoral model

A new type of Mg-rare earth (Ce, La) and AZ31 alloy sheets were prepared by vertical twin-roll casting (TRC) technology under identical casting conditions, and their microstructure features, degradation behavior and bone response were investigated. Microstructure characterization showed that the Mg-RE exhibited a higher amorphous forming ability than the AZ31. The Ti, Mg-RE and AZ31 sheet implants were implanted in immobilized rat femur model to observe degradation behavior during 16 weeks. The results showed that no significant change was found in the femur surrounding the Ti. This excluded the external factor that the new bone formation resulting from bone remodeling. The degradation rate of the Mg-RE was about 0.11 mm/year after 16 weeks implantation, significantly slower than that of AZ31. In addition, the Mg-RE induced more newly formed bone, which met the necessary conditions for the prevention of pathological fractures. Therefore, the novel Mg-RE alloy appear to hold a healing candidate as the biodegradable implant material.

4.1 Introduction

Magnesium (Mg) alloys with excellent biocompatibility, biodegradability, and bone formation capacity have been widely applied to manufacture bone fixation implants. It is reported that Mg alloys can reduce the risk of the load-shielding after implanting surgery due to their Young's modulus similar to bone [1]. Furthermore, studies have shown that Mg-based alloys implanted within or surrounding the bone present very good biocompatibility [2-6]. Unlike resorbable polymers and permanent inert materials such as stainless steel and titanium (Ti) alloys, Mg alloys possess a unique degradation which is being explored for various orthopedic applications. Hence, there is no necessary to perform a second removal

surgery of the implant after osseous union. It is noteworthy that most of studies of Mg alloys implants are in animals, for instance, rabbit [7], rat [8], pig [9] which present good biocompatibility and normal physiological for different types of Mg alloys. It is demonstrated that Mg^{2+} ions released from Mg-based alloys could present bioeffect for instance inducing new partial bone formation [10-13]. Moreover, the bone around Mg alloy implants presented increased bone mass, mineral apposition and bone mineral density [14-17]. However, Mg-based alloys have its limitations, such as a notably rapid degradation rate reported by previous research [18]. The rapid degradation results in producing Mg hydroxide and hydrogen gas leading to a change in the PH of the tissue fluid which is the most likely to cause tissue inflammation and adversely affect the viability of cells. Therefore, there is a growing need of developing novel degradable magnesium alloys with superior corrosion resistance performances.

It is well known that some rare-earth elements have been found in the human body [19], and the addition of rare-earth elements could effectively improve the corrosion resistance and mechanical properties of Mg alloys [20,21]. Due to the presence of sensitive impurities, the corrosion resistance of Mg alloys will be damaged once the contents of impurities exceed the tolerance limits [22]. However, the rare-earth elements in Mg alloy could combine with the impurities (Cu, Fe, Ni, etc.) forming depositions during the melting process. This effect is so-called “the scavenger effect”. It is believed that the scavenger of rare-earth can effectively improve the corrosion resistance of Mg alloys. In addition, rare-earth elements such as Ce and La could optimize the microstructure of Mg alloys and improve the corrosion resistance of Mg alloys [23]. Hence, researching new type of Mg-RE (RE = rare-earth) alloy is a direction to reduce degradation rate.

On the other hand, optimizing the microstructure of materials is another approach to improve corrosion resistance. It is well known that metallic glasses (MGs), as a newcomer in the field of metals (liquid metals or amorphous/glassy alloys), have an amorphous structure endows unique properties such as lower Young’s modulus, higher strength, excellent corrosion resistant and fatigue [24,25].

Previous studies have shown that twin roll casting (TRC) is a useful technique for preparing amorphous alloy sheets with a wide range of cooling rates. Therefore, TRC process has a great significance to develop new corrosion resistant Mg alloys with amorphous phase.

In the present study, a new Mg alloy was developed by adding rare earth (La, Ce) and adopter for vertical-type twin roll casting. Details of microstructure, *in vivo* degradation (In this study, "degradation" has the same meaning with "corrosion") and bone response of a new Mg-RE (Ce, La) and AZ31 implants were investigated during a 16-week observation by a fixed model in rat femoral. In addition, the evaluation of bone response might be influenced by bone remodeling result from fixed model. Therefore, we compared the bone response of non-absorbent Ti with those of casting-rolled Mg-RE and AZ31 to excluded the external factor caused by altering the mechanical loading of the implants.

4.2 Materials and Methods

4.2.1 Material preparation and characterization

High purity of Mg ingot (99.99%), AZ31 ingot, Mg-10La and Mg-20Ce (in wt.%) were used as raw materials. The melting process was carried out in a resistance furnace under the protection of a mixture of CO_2 and FS_6. AZ31 sheets in this study were produced by melting Mg ingot and AZ31 ingot. The Mg-RE sheets in this study were produced by melting Mg ingot, AZ31 ingot, Mg-10La and Mg-20Ce. Firstly, the Mg ingot and AZ31 ingot were placed into the resistance furnace, and the compound were heated up to 720 ℃ for 1.5 h to completely melted. Secondly, the Mg-10La and Mg-20Ce master alloys were added into the melt, then the melt temperature reduced to 700 ℃ and held for 1.5 h. It can be seen that AZ31 alloy sheets could be obtained in the first casting process, while Mg-RE alloy sheets could be obtained in the whole casting process. The chemical compositions of the alloy sheets were determined by X-ray fluorescence spectrometry and the results

were listed in Table 4-1.

Table 4-1 chemical composition of the cast-rolled sheets

Cast-rolled sheets	Thickness (mm)	Width (mm)	Element (wt.%)						
			Al	Si	Mn	Zn	La	Ce	Mg
AZ31	1.1	75	2.55	0.22	0.43	0.75	-	-	Bal.
Mg-RE	1.2	80	1.21	0.16	0.27	0.21	1.53	2.78	Bal.

The TRC experiments were carried out on a vertical-type twin roll casting mill with two identical rolls made of copper alloy. The diameter and width of both rolls are 300 mm and 100 mm respectively, and the initial roll gap was set to be 0 mm. In consideration of the separation force generated in the casting process, metal blocks were set at the two rotating rolls side to form a supporting force, minimizing the roll gap during casting process as much as possible. When the alloy melted completely, the melt was introduced into the roll gap between the left and right rolls through the asbestos casting nozzle, and the casting rolls begins to operate with 30 rpm. An oil tank was placed under the rotating rolls to avoid further grain growth, hence the cast sheet dipped into the tank could quickly solidify as exits at the rolls. The schematic diagram and practicality illustration of TRC are shown in Fig. 2.5 (a) and Fig. 2.5 (b), respectively.

The specimens with the size of 10 mm in width and 10 mm in length were cut from the sheets, and the transversal cross-section was selected for microstructure analysis. The microstructures were observed using a field emission scanning electron microscope (FE-SEM, JMS-6301, Japan), In addition, the elements distribution maps were performed by electron probe micro-analysis (EPMA, JXA-8530F, Japan). The secondary dendrite arm spacing of AZ31 and Mg-RE were analyzed by Image-Pro analysis software. At least 6 metallographic images were selected for each alloy sheet, and more than 60 groups of secondary dendrites randomly distributed were counted for each metallographic image, and the average

value was taken as the final secondary dendrite arm distance. The focused ion beam (FIB, JIB-4500, Japan) and the transmission electron microscopy (TEM, HF-3300, Japan) were used to identify the crystal structure of the samples.

4.2.2 Implant method

The Ti, Mg-RE and AZ31 samples were lathe machined into 15 mm × 5 mm with a thickness 0.5 mm. All surfaces were grounded with SiC papers up to 1200 grid in order to ensure surface flatness and roughness. Ti and Mg screws (4.5 mm in length, with a shaft diameter of 3.2 mm) were selected to immobilized the Ti, and casting-rolled sheets respectively.

4.2.3 Electrochemical characterization

In vitro corrosion tests were conducted at the temperature of 310 K in 3.5% NaCl solution. EIS (Modulab XM, Tokyo, Japan) and Potentiodynamic polarization (HZ700, Tokyo, Japan) tests were performed in a three-electrode cell. Sheet samples were connected as the working electrodes. Potentials were measured versus the Ag/AgCl electrode. Platinum played the role of auxiliary electrode. The samples were immersed in the 3.5% NaCl solution for one-hour at their open circuit potential. The EIS tests were recorded in a frequency range from 10^{-2} Hz to 10^{5} Hz applying a sinusoidal AC voltage signal of 0.01 V amplitude. Potentiodynamic polarization were initiated at a 0.01 V/s scan rate from the open circuit potential (E_{oc}) to $V_{vs\ Ag/AgCl}$, and then from $V_{vs\ Ag/AgCl}$ to E_{oc}.

4.2.4 Micro-CT analysis

Micro-CT was used to evaluate implants degradation and the formation of new bone. Image processing was performed by means of 3D Viewer and Volume Rendering Control. 3D volumes of the scanned devices were generated from acquired 2D lateral projections using a Simple Viewer software.

4.2.5 In vivo corrosion assessment

The transversal cross-section morphology and elemental composition of Mg-RE and AZ31 sheets were observed by a field emission scanning electron microscope (FE-SEM, JMS-6301, Japan) and the elements distribution maps were observed by electron probe micro-analysis (EPMA, JXA-8530F, Japan). The procedure of removal of sheets from femur without damaging the tissue formed between the sheet and femur.

4.2.6 Histological observation

The femur samples surgically extracted from the rats were fixed in 10% formalin solution for 48 hours and decalcified with a decalcification solution (10% ethylenediamine tetra-acetic) for 28 days. Next, the samples were rinsed by running water and dehydrated in a graded series of alcohol solution (70%, 80%, 95% and 99% alcohol, 2 h each). Then the dehydrated samples were imbedded in a paraffin block. A cutting-grinding unit was used to slice the section of the femurs in contact with the sheets. Finally, the slice samples were stained by hematoxylin and eosin (H&E) and then the new bone morphology were observed by a microscope.

4.2.7 Statistical analysis

All experimental data analysis was conducted using SPSS 20. Statistical significance was analyzed using one-way analysis of variance (ANOVA) followed by Tukey tests. The statistical significance was set a p-value of less than 0.05 ($p<0.05$).

4.3 Results and discussion

4.3.1 Microstructures analysis

Fig. 4.1 shows the microstructure of AZ31 and Mg-RE sheets produced by TRC process. It can be seen from Fig. 4.1 (a) that the microstructures of the casting-rolled AZ31 are composed of unevenly distributed dendrite regions. The fine dendrites are obvious in the yellow rectangle region as shown in Fig. 4.1 (b) which are named AZ31's region of interest (A-ROI). Fig. 4.1 (c) displays the microstructures of Mg-RE sheets which are mainly characterized by dendrites with closely spaced secondary dendrite arms and fine equiaxed crystals. Meanwhile, it can be found that some special regions having no visible crystalline features indicated by the yellow rectangle region as shown in Fig. 4.1 (d), which are named Mg-RE's region of interest (M-ROI).

To determine the phase of A-ROI and M-ROI, high resolution transmission electron microscope (HR-TEM) images with selected area electron diffraction (SAED) patterns of those two observation regions are shown in Fig. 4.2. It can be observed that the atoms are arranged in regular lines in A-ROI, and the SAED pattern indicates A-ROI is the hexagonal close packed lattice (HCP) structure, as shown in Fig. 4.2 (a). However, HR-TEM image of M-ROI shows that there are three types atomic arrangements displayed in Fig. 4.2 (b).

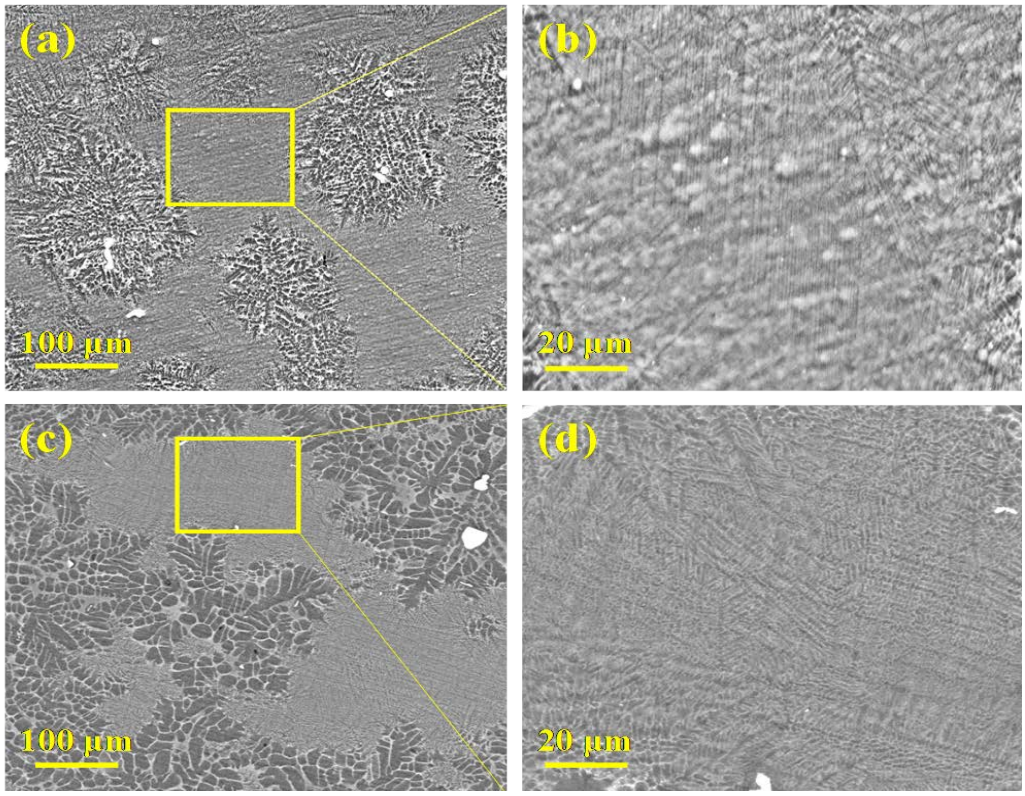

Fig. 4.1 Cross-section microscopic morphologies of casting-rolled AZ31 sheet (a, b) and Mg-RE sheets (c, d).

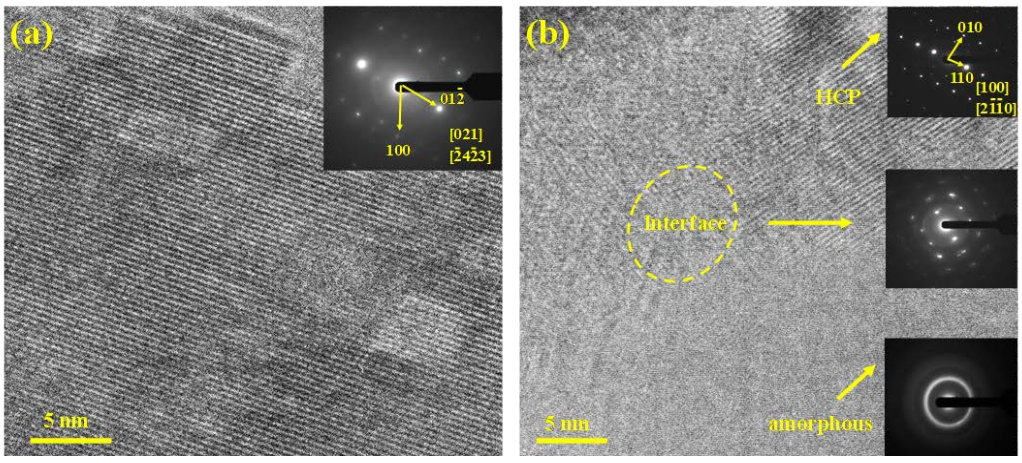

Fig. 4.2 HR-TEM images and corresponding SAED patterns showing A-ROI in AZ31 sheets (a) and M-ROI in Mg-RE sheets, respectively.

The atoms arranged in order is determined to be HCP structure, while the atoms arranged in disorder is confirmed to be amorphous phase. The interface between crystal phase and amorphous phase exhibits HCP diffraction pattern. Those results indicate that Mg-RE alloy contains amorphous structure.

Fig. 4.3 (a) and (b) shows the statistical results of secondary dendrites arm spacing of the AZ31 and Mg-RE sheets. The average secondary dendrite arm spacing of the AZ31 and Mg-RE is 0.75 μm and 0.62 μm, respectively. Secondary dendrite arm spacing is correlated with the solidification rate, and increase cooling rate can result in finer secondary dendrite arm spacings [27]. According to the previous research [28], the quantitative between the cooling rate and secondary dendrite arm spacings following relationship:

$$\lambda=35.5R^{-0.31} \qquad (4.1)$$

where R is averaged cooling rate ($K\cdot s^{-1}$) during solidification; λ is the distance between secondary dendrites (μm). Based on formula (1), the AZ31 and Mg-RE were obtained under casting condition with cooling rate of 2.53×10^5 $K\cdot s^{-1}$ and 4.68×10^5 $K\cdot s^{-1}$, respectively, which both presented a fast cooling rate. The research [29] present that the formula (4.1) is applicable for the cooling rate of 10^{-1} $K\cdot s^{-1}$ ~ 10^6 $K\cdot s^{-1}$. According to the calculation results, it is suitable to use the formula (4.1) to evaluate the cooling rate during TRC process. The SEM image of the Mg-RE containing amorphous regions is presented in Fig. 4.3 (c), and the volume fraction containing amorphous of M-ROI statistical results is given in Fig. 4.3 (d). It can be seen that the average volume fraction of the regions containing amorphous is 14.3% in the Mg-RE sheet samples. From the above results, it can be concluded that the Mg-RE can possess an amorphous phase made by TRC method. However, it is quite hard to obtain amorphous phase for the AZ31, even trying to build a fast cooling rate with TRC method. Therefore, the amorphous phase forming ability of the Mg-RE is higher than the AZ31 during rapid cooling solidification. Hence, it is hypothesized that the Mg-RE alloy has a better corrosion resistant than AZ31 alloy.

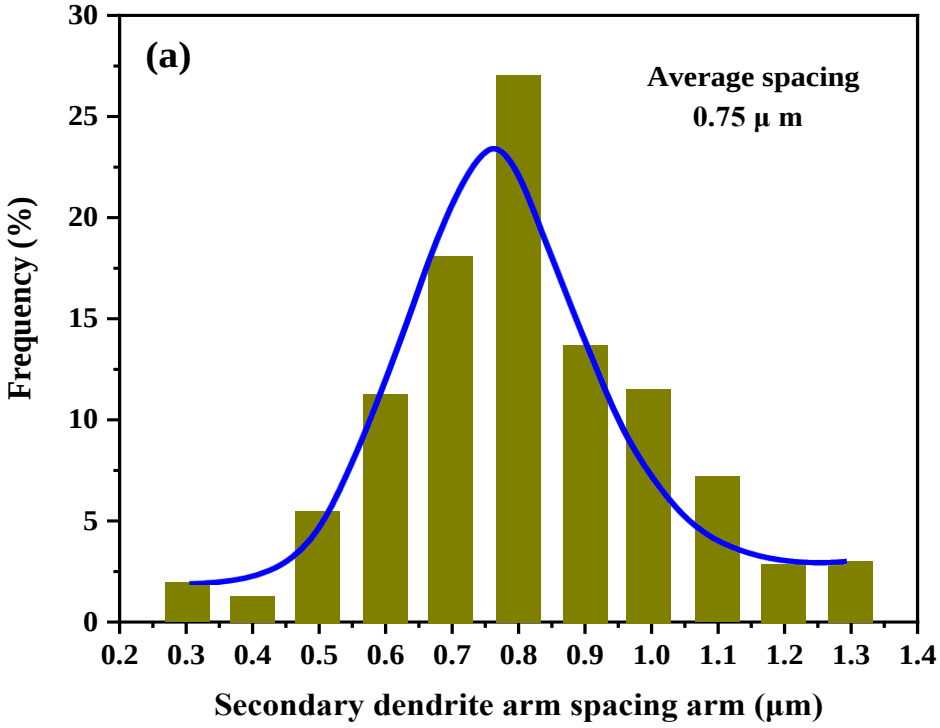
(a)
Average spacing
0.75 µ m
Frequency (%)
Secondary dendrite arm spacing arm (µm)
0
5
10
15
20
25
30
0.2
0.3
0.4
0.5
0.6
0.7
0.8
0.9
1.0
1.1
1.2
1.3
1.4

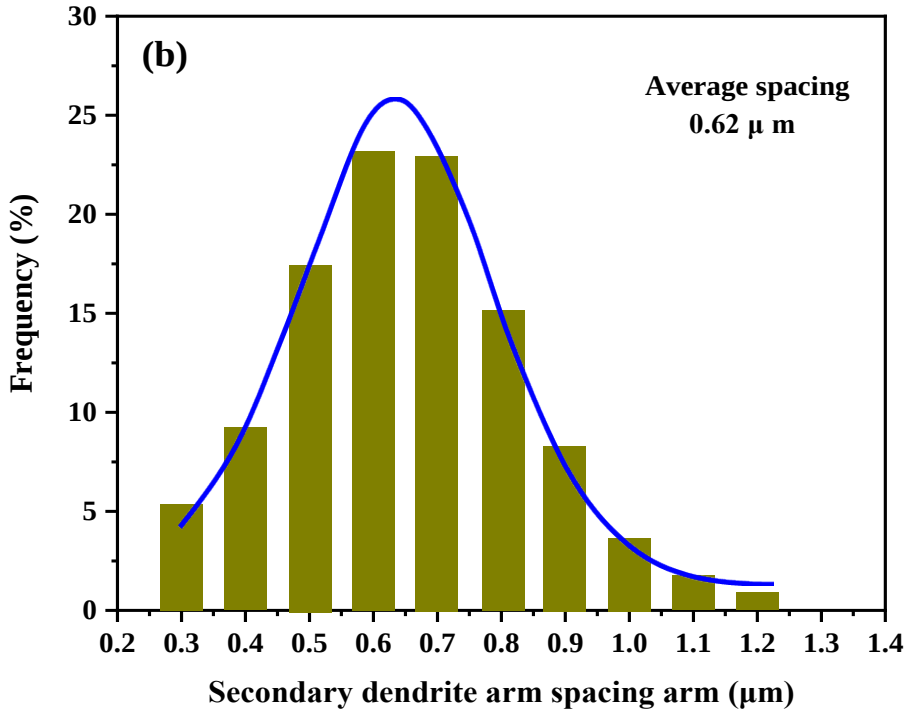
(b)
Average spacing
0.62 µ m
Frequency (%)
Secondary dendrite arm spacing arm (µm)
0
5
10
15
20
25
30
0.2
0.3
0.4
0.5
0.6
0.7
0.8
0.9
1.0
1.1
1.2
1.3
1.4

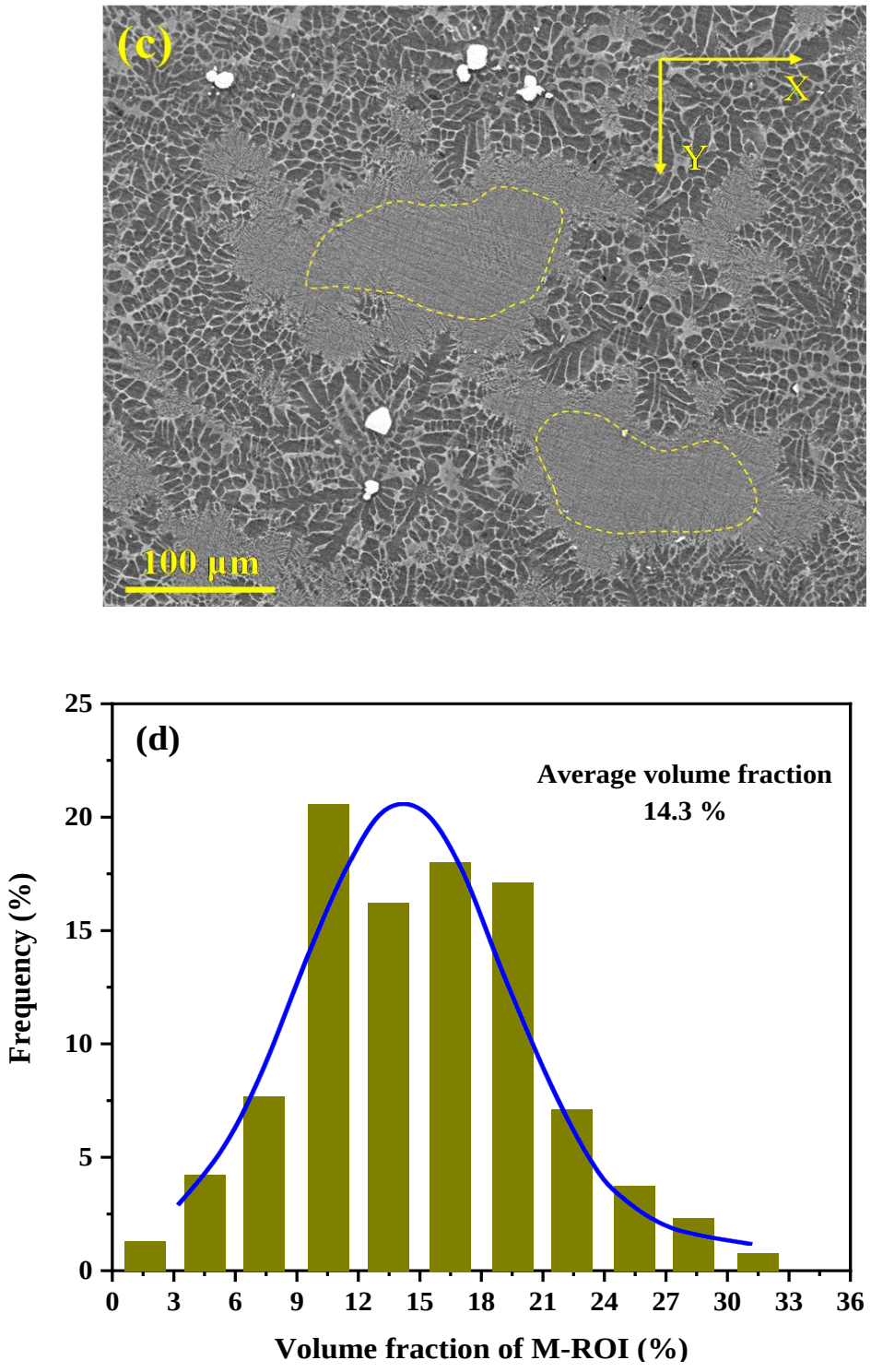

Fig. 4.3 Statistical results of secondary dendrites arm spacing of AZ31 sheets (a) and Mg-RE sheets (b); SEM micrograph of Mg-RE (c), volume fraction estimation of M-ROI, indicated by the yellow regions and the statistical results is shown in (d).

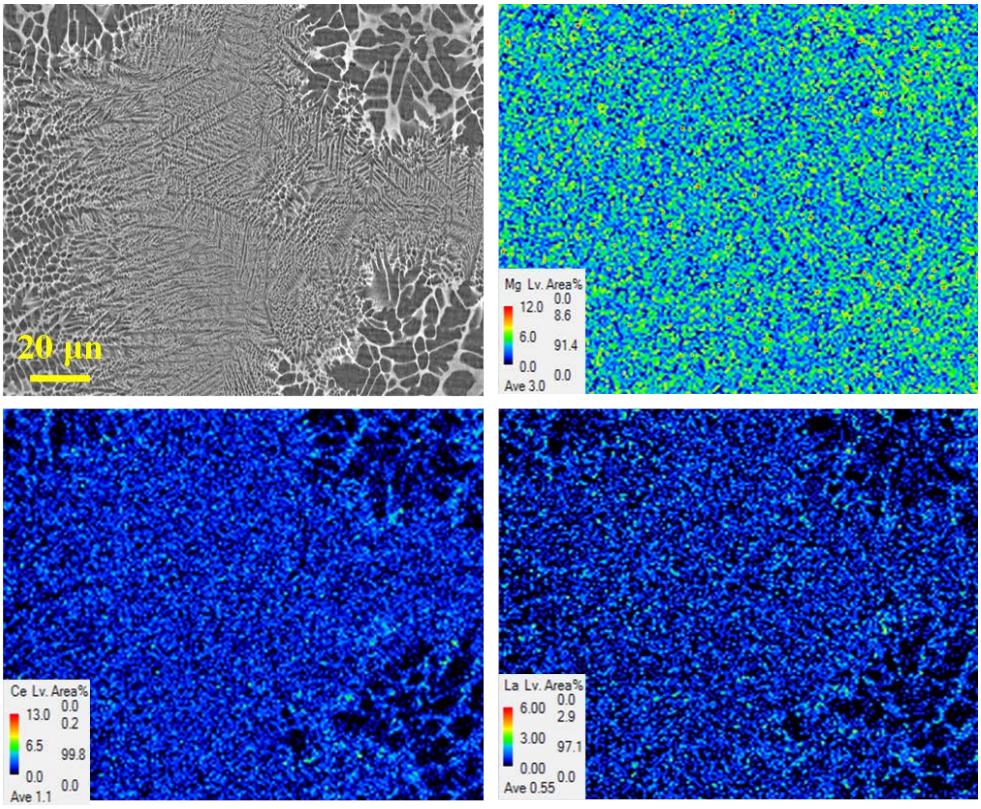

Fig. 4.4 The Mg, Ce and La element distribution of the Mg-RE sheet in region containing amorphous phase regions.

Fig. 4.4 shows the Mg, Ce and La elements distribution of the Mg-RE sheet containing amorphous phase regions. It can be seen that Mg is evenly distributed on the substrate, Ce and La concentrated in the region containing the amorphous, which indicates that addition Ce and La into the Mg-based alloy is beneficial to form amorphous. As the secondary dendrite arm spacing around the amorphous phase is very short, it can be seen from formula (4.1) that this region has a large cooling rate during solidification. If the cooling rate is large enough, the atoms with a high melting point in the melt loose kinetic energy when the temperature drops [30]. For these reasons, the atoms in the melt to freeze and form an amorphous phase.

In general, the key factor of preparing amorphous alloys is to obtain high cooling rates during solidification of casting alloys. In this study, the current TRC conditions could provide a rapid cooling rate up to 10^5 $K \cdot s^{-1}$. If the cooling rate is fast enough that crystal structure in the melting liquid has no time to nucleate and grow, the liquid can avoid crystallization during rapid solidification. The liquid is called supercooled liquid. The viscosity of supercooled liquid can be expressed by the following equation [31]:

$$\eta^{-1} = A\exp(-K/V_f) \qquad (4.2)$$

where A and K are constant; V_f is free volume. In this study, there were more element components in Mg-RE relative to AZ31, and larger atomic size difference among the major elements. For example, the relative atomic radius difference between Mg and rare-earth elements (Ce, La) is more than 12%. According to formula (4.2), the larger atomic size difference will result in reducing free volume and increasing the viscosity of the supercooled liquid. Increasing the viscosity of the supercooled liquid makes the atoms hard to spread over long-range, so it is easier for the alloys to form amorphous states. In addition, an appropriate negative enthalpy of mixing ($\Delta Hmix\ [AB]$) between major elements is also a necessary condition for good amorphous forming ability [32]. The $\Delta Hmix\ [AB]$ of Mg-Ce and Mg-La calculated by Miedma's model are both −7 KJ/mol [33]. In general, the Mg-RE are easier to form amorphous phase than the AZ31.

The solute distribution coefficient during the rapid solidification process can be expressed as [34]:

$$K=C_s/C_L \qquad (3)$$

Where K is the solute partition coefficient; C_s is the solute concentration in the liquid phases; C_L is solute concentration in the solid phases. The K values of the major elements such as Ce and La in Mg-RE is less than 1 during solidification. Based on formula (3), the content of solute elements (Ce, La) in preferentially crystallized solids is less than the content of solute elements (Ce, La) in surrounding liquids. Solute atoms such as Ce and La are continuously discharged

into the liquid phase and enriched the supercooled liquid regions during rapid solidification process (Fig. 4.4).

4.3.2 In vitro corrosion properties

To get information about the corrosion behavior of those sheets, the corrosion resistance of the three samples was evaluated by EIS and potentiodynamic polarization in 3.5% NaCl solution at temperature of 310 K after one-hour immersion, as shown in Fig. 4.5. The Nyquist and Bode plots (Fig. 4.5 a-c) of the AZ31, Mg-RE and Ti were characterized by two apparent time constants in the two capacitive loops of high-middle and low frequency areas. The equivalent circuit (Fig. 4.5 a) was used to investigate the EIS quantitatively, and the fitting results presents in Table 2. The equivalent circuit model consisted of R_s (solution resistance), R_1 (charge-transfer resistance), R_2 (film resistance), constant elements CPE1 and CPE2, where, CPE1 and CPE2 represent the capacitive behaviors of oxidation film and charge-transfer, and Q is the CPE magnitude, n value is a nature element [35]. Generally, an increase in the values of the charge transfer resistance with a decrease in the dissolution rate of the materials substrate [36]. According to the results of Table 4-2, both R_1 and R_2 of the AZ31 are lowest among those sheets, indicating an increased dissolution rate of the materials substrate. The sum of R_1 and R_2 for sheets were in the following order: AZ31 < Mg-RE < Ti, indicating the Mg-RE possess a better corrosion resistance than AZ31.

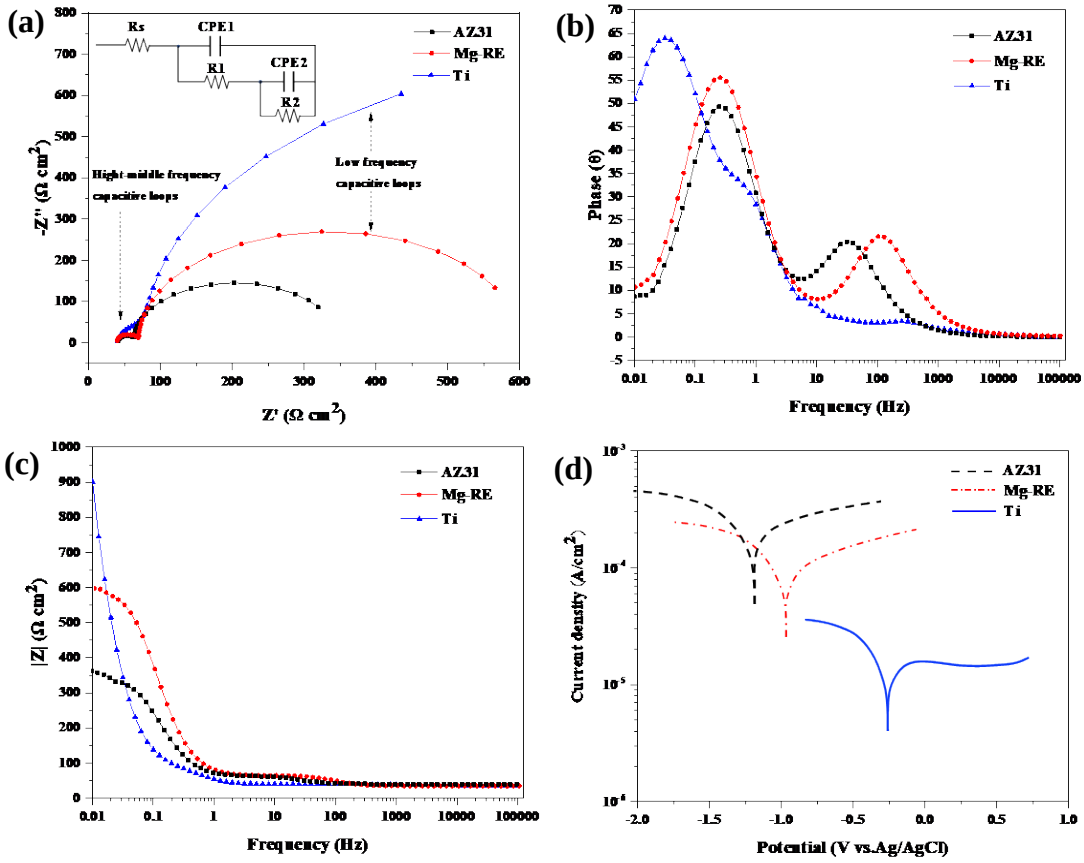

Fig. 4.5 (a) Electrochemical behaviors of the AZ31, Mg-RE and Ti implants in 3.5% NaCl solution: (a) Nyquist spectra plots and equivalent circuit; (b, c) Bode plots of EIS; (d) The potentiodynamic polarization curves.

The potentiodynamic polarization curves of the sheet materials in 3.5% NaCl solution at temperature of 310 K after one-hour immersion are shown in Fig. 4.5 (d). The average values corrosion potential (E_{corr}) and corrosion current density (i_{corr}) measured by Tafel extrapolation are presented in Table 4-3. The Mg-RE have more positive value of E_{corr} (-0.88 V vs Ag/AgCl) and lower i_{corr} (5.1×10^{-4} A cm^{-2}) than these of AZ31, which implies the rolled samples of the Mg-RE present a higher corrosion resistance. In conclusion, the results of the electrochemical tests confirm the hypothesis that the Mg-RE alloys with higher amorphous forming ability have better corrosion resistance. In this study, the Mg-RE has an amorphous structure, in which the atoms have short-range arranging or are no crystalline defects, like gain boundaries or dislocations. A previous study [37] showed that

amorphous alloys have much higher corrosion resistance than crystalline alloys due to the absence of grain boundaries and second phases.

Table 4-2 Fitting resulting of EIS spectra

Alloy	R_S	CPE1		R_1	CPE2		R_2
	(Ω cm^2)	Q_1 (μF cm^{-2}s^n)	n	(Ω cm^2)	Q_2 (μF cm^{-2}s^n)	n	(Ω cm^2)
AZ31	24.89	274.8	0.84	24.45	5496	0.82	279.7
Mg-RE	25.11	66.83	0.81	31.7	3864	0.83	528.4
Ti	24.96	5350	0.80	90.09	10670	0.81	1328

Table 4-3 E_{corr} and I_{corr} values for AZ31, Mg-RE and Ti in 3.5% NaCl solution

Sample	E_{corr} (V vs Ag/AgCl)	I_{corr} (A cm^{-2})
AZ31	-1.13	9.5×10^{-3}
Mg-RE	-0.88	5.1×10^{-4}
Ti	-0.25	1.2×10^{-5}

4.3.3 Animal test

All fixed implants were well accommodated by the animals and without any obvious adverse health events and the animals showed no gas cavities *in vivo*. During 16-week observation period after the operation, experimental animals resumed normal movement and behavior bearing on both forearms (Date not shown).

4.3.4 Degradable implant cross-sectional examination

For studying the corrosion products of the Mg-RE and AZ31 implants that *in vivo* contact with the femur, Mg and other elements such as C, O, P and Ca in corrosion layer were studied. The morphologies of the cross-section of the Mg-RE and AZ31 and corresponding elements distribution were detected by the EPMA mapping surface-scan at 8 and 16 weeks postoperatively as shown in Fig. 4.6 and Fig. 4.7. Mg, O, C, P, Ca and rare-earth (Ce, La) distributions in the cross-section

of the sheets were analyzed. After the Mg-RE and AZ31 were implanted with femur for 8 weeks (Fig. 4.6), the external surface of the implants began to degrade. The Mg substrate was transformed into magnesium hydroxide and the compound containing O, C, P and Ca as the corrosion products. It also can be seen that the amount of Mg in corrosion layer of Mg-RE was higher than that AZ31. This demonstrated that the *in vivo* corrosion products of the Mg-RE have thicker protective magnesium hydroxide layer than the AZ31. Furthermore, the rare earth (La, Ce) distribute in the corrosion layer and the substrate of Mg-RE were rather homogeneous.

As the implantation time for 16 weeks (Fig. 4.7), O, C, P and Ca distributions extended to the internal section gradually. The Mg in corrosion layer of the Mg-RE was slight decreased from 8 weeks after implantation. However, the Mg content in the AZ31 corrosion layer was very low, which suggested the magnesium hydroxide almost degraded. In addition, the rare earth (Ce, La) in the corrosion layer have not changed significantly. The experimental results demonstrate that the degradation of the Mg-RE was more slowly than that of the AZ31, which may be ascribed to the addition rare-earth (Ce, La) relieved the degradation of the magnesium hydroxide, thus improving the corrosion resistance.

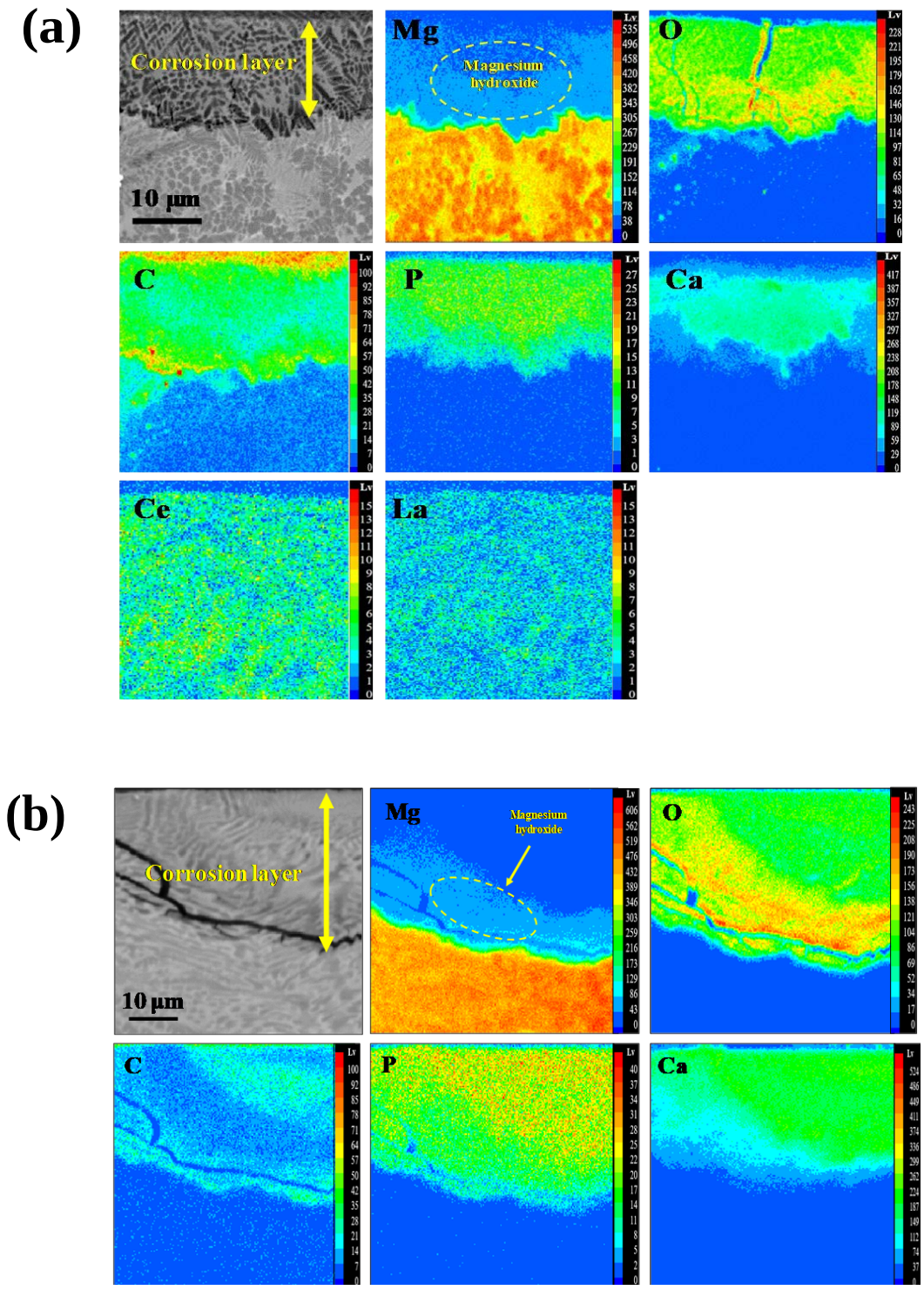

Fig. 4.6 Cross-section images and EPMA surface-scan of (a) Mg-RE sheets, and (b) AZ31 sheets after 8 weeks implantation.

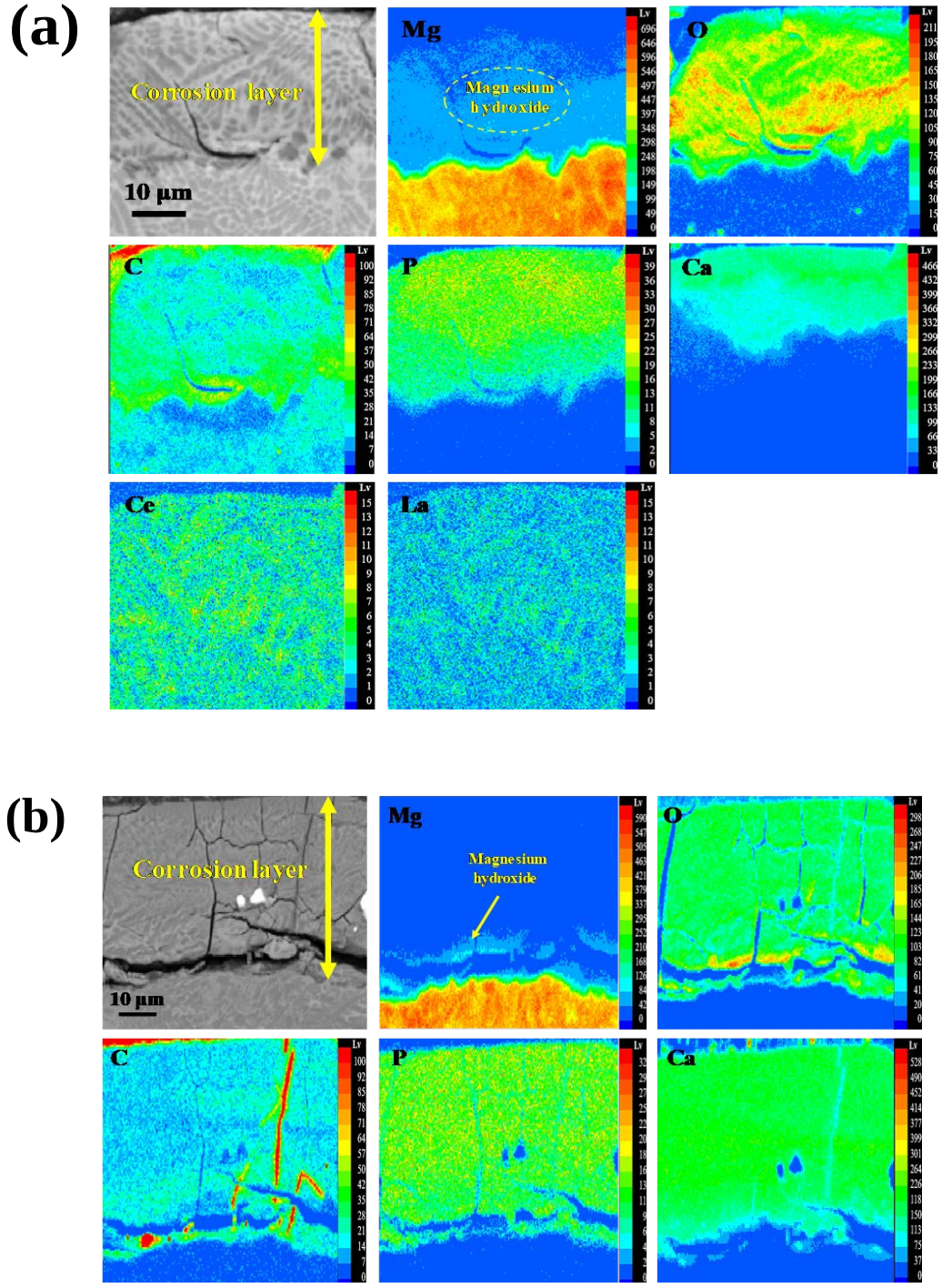

Fig. 4.7 Cross-section images and EPMA surface-scan of (a) Mg-RE sheets, and (b) AZ31 sheets after 16 weeks implantation.

In general, the poor corrosion resistance of Mg-based alloys limits their application as implants. The reasons for rapid degradation of Mg-based alloys is multifaceted, but mainly due to the chloride ion transform magnesium hydroxide protection layer into soluble magnesium chloride [38]. In this study, the total amount of Mg in corrosion layer of the AZ31 significant decreased after 8 weeks and 16 weeks implantation compared with the Mg-RE (Fig. 4.6 and 4.7). Consequently, the corrosion resistance of the AZ31 decreased with the amount of Mg element compared with the Mg-RE. It is noting that the rare-earth (Ce, La) in the corrosion layer of the Mg-RE were homogeneous distribution after 8weeks and 16 weeks implantation respectively (Fig. 4.6 and 4.7). Because of enrichment of rare-earth (Ce, La) in the corrosion layer of magnesium alloys, the corrosion product layer was complete and compact, which improved the protective effectiveness of the corrosion layer and restrains further degradation of Mg substrate in corrosive mediums [39].

The degradation products mainly contain Mg, O, C, P and Ca, which exist both in the Mg-RE and AZ31. Previous studies [40-42] have demonstrated that these degradation products similar to composition of nature bone exhibit good biocompatibility. Therefore, it can draw the conclusion that the biocompatibility of the degradation products of the Mg-RE is acceptable as biomaterials.

4.3.5 Bone response and histological examination

Fig. 4.8 shows the representative images of 3D micro-CT reconstruction of a rat femur with implanted sheets 2 weeks, 8 weeks and 16 weeks after surgery. The Ti, Mg-RE and AZ31 implants remained in their original position, and bone callus formation was observed in the 500-slice region of interest. In the Ti group, there was no bone callus formation at the area between the Ti sheet and the femur in all experimental periods. Limited bone callus formation could be detected between the AZ31 sheet and the femur at 8 and 16 weeks of implantation. In contrast, a large increase in bone mass was found at the area between the Mg-RE sheet and the

femur. The boundary between the Mg-RE sheet and the femur was not obvious after 16 weeks implantation resulting from the new bone formation.

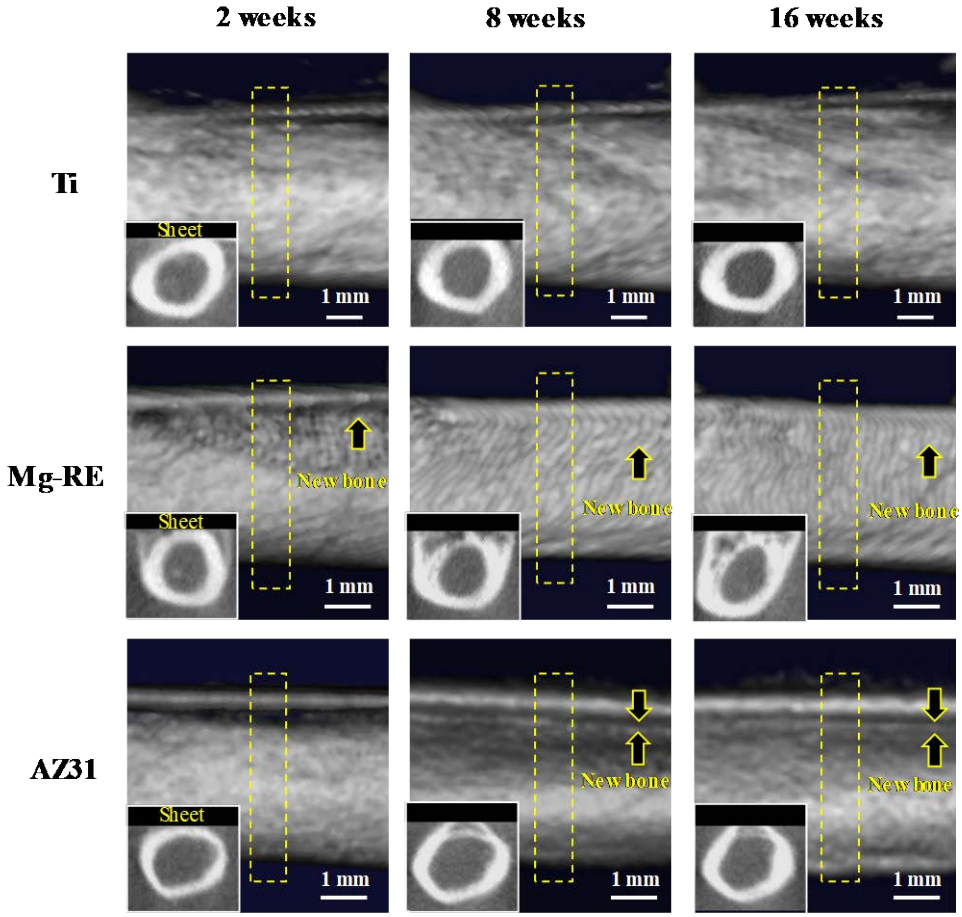

Fig. 4.8 Representative 3D micro-CT reconstruction illustrating the bone respond of Ti, Mg-RE and AZ31 sheet implants after 2, 8 and 16 weeks postoperatively. Yellow boxes indicate the horizontal section region of interest BV/TV: bone volume/tissue volume. Tb. N: umber of trabecular bone.

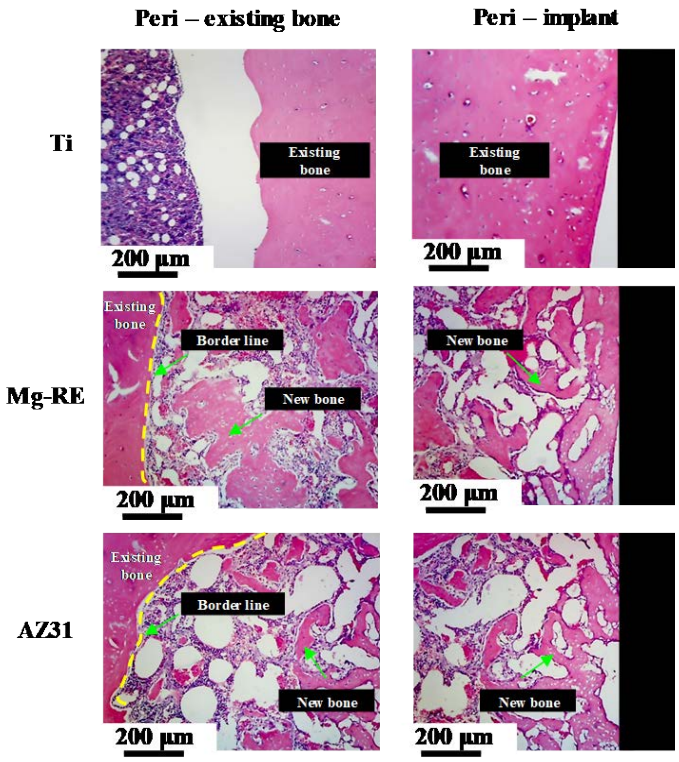

Fig. 4.9 Decalcified sections with hematoxylin and eosin (H&E) staining showing the morphology of the peri-existing bone and the new bone around the implants (black boxes) 16 weeks after implantation.

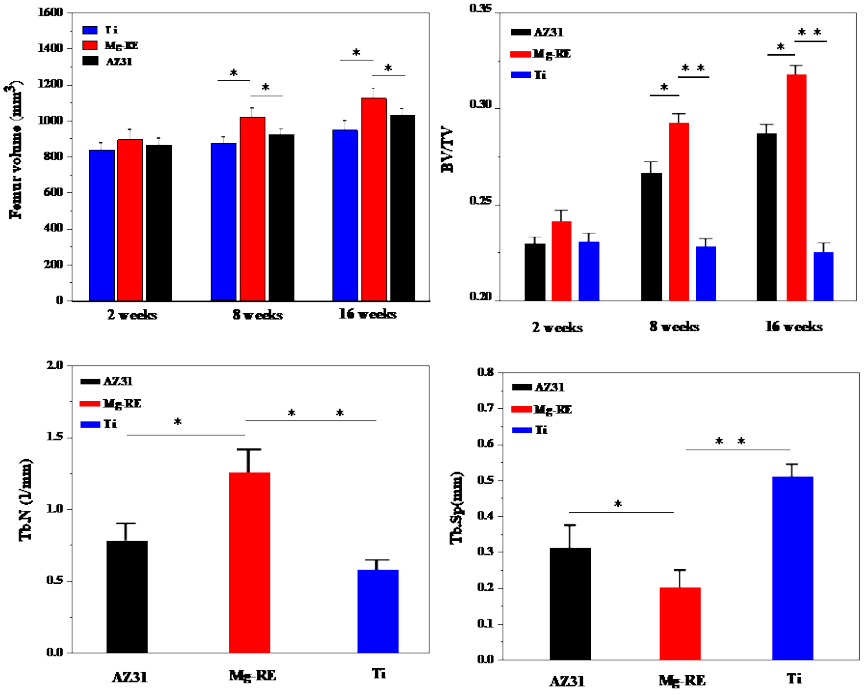

Fig. 4.10 Statistical analyses of parameters of femur based on horizontal section region of interest (*P < 0.05, **P < 0.01).

Fig. 4.9 shows the histological images of the bone-implant interface that an area where new bone formation around the Ti, Mg-RE, AZ31 sheet samples after 16 weeks postoperatively. In the Mg-RE group, the new trabeculae formation almost filled the bone-implant gap 16 weeks after implantation, and there was more mature new bone structure at near existing bone. In contrast, there were a limit amount of newly formed trabeculae around implant and existing bone in the AZ31 group. However, no newly formed trabeculae were observed around the Ti group. In addition, no inflammatory reactions occurred in the area where new bone formation around the Mg-RE, AZ31 samples throughout the experiment. From the horizontal section 2D of the region of interest, the femur volume, BV/TV, Tb. N and Tb. Sp level (Fig. 4.10) suggest that indicating a large bone bridge is formed across the interface with Mg-RE group, and bone formation was directed towards the Mg-RE implants.

In this study, no significant change was found in the femur surrounding the non-absorbent Ti. This excluded the external factor that the fixed implants might cause bone remodeling by altering the mechanical loading of the implants. In general, the new bone formation during implantation of Mg-based alloy is known as a good sign, because it wound facilitate fracture healing [43]. In the present study, more new bone formation was found around the Mg-RE than that around the AZ31. The reason was attributed to as these sheets degrade, and local tissue are stimulated by Mg^{2+} to form new bone [44]. Studies [11,45,46] demonstrated that the beneficial effect of Mg^{2+} on new bone formation. The osteocyte adhesion and bone tissue growth could be enhanced by Mg^{2+}. However, superfluous Mg^{2+} released with degradation may inactivate new bone tissue formation, resulting in the less of new bone tissue around the implants [47]. In addition, the biological effects of rare-earth on new bone formation are unclear. Some animal experiments [48, 49] showed that the rare-earth had positive effects on osteoblast activation and bone mineral density. It is noteworthy that the periosteum formation of new bone and the increased femur volume should not be considered a positive response to Mg-RE, but considered necessary to cure pathological fractures [50].

It is notable noting that there are limitations in the *in vivo* study. Firstly, it is not known the serum metabolic parameters of the animal body during the process of implants degradation. Secondly, in this study, the surgical was performed when the bone was completely healthy. Therefore, further experimental studies are needed to investigate whether Mg-RE has a therapeutic effect on clinical healing of fractures or bone damage.

4.4 Concluding remarks

In the present work, the Mg-RE and AZ31 alloy sheets with same continuous casting conditions for *in vivo* implants were prepared by TRC process. The microstructure, *in vivo* degradation behavior and bone response for 16 weeks of Mg-RE and AZ31 sheets were investigation systematically. We found that the Mg-RE present a better amorphous forming ability than AZ31 under the same casting conditions. The results of electrochemical tests showed that the Mg-RE sheets exhibit a higher corrosion resistance with respect to the AZ31 sheets. *In vivo* study showed that no significant change was found in the femur surrounding Ti sheet. This excluded the external factor that the new bone formation resulting from bone remodeling. Much more new bone tissue around the Mg-RE sheet. It indicates that the Mg-RE have potential to be implants for wide application.

4.5 References

1. R. Huiskes; H.H. Weinans, R. van Rietbergen. The relationship between stress shielding and bone resorption around total hip stems and the effects of flexible materials, Clin. Orthop. Relat. Res. 274 (1992) 124–134.
2. Z. Li, S. Shizhao, M. Chen, B.D. Fahlman, D. Liu, H. Bi, In vitro and in vivo corrosion, mechanical properties and biocompatibility evaluation of MgF2-coated Mg-Zn-Zr alloy as cancellous screws, Mater. Sci. Eng. C. 75 (2017) 1268-1280.
3. P. Han, P. Cheng, S. Zhang, C. Zhao, J. Ni, Y. Zhang, W. Zhong, P. Hou, X. Zhang, Y. Zheng, Y. Chai, In vitro and in vivo studies on the degradation of high-purity Mg (99.99 wt.%) screw with femoral intracondylar fractured rabbit model, Biomaterials. 64 (2015) 57-69.
4. S. Ouyang, Y. Liu, Q. Huang, Z. Gan, H. Tang, Effect of composition on in vitro degradability of Ti–Mg metal-metal composites, Mater. Sci. Eng. C. 107 (2020) 110327.
5. X. Kong, L. Wang, G. Li, X. Qu, J. Niu, T. Tang, K. Dai, G. Yuan, Y. Hao, Mg-based bone implants show promising osteoinductivity and controllable degradation: A long-term study in a goat femoral condyle fracture model. Mater. Sci. Eng. C. 86 (2018) 42-47.
6. J. Lee, H.S. Han, K.J. Han, J. Park, H. Jeon, M.R. Ok, S.J. Yang, Long-term clinical study and multiscale analysis of in vivo biodegradation mechanism of Mg alloy, Proc Natl Acad Sci USA. 113 (2016) 716–721.
7. L.Y. He, X.M. Zhang, B. Liu, Y. Tian, W.H. Ma, Effect of magnesium ion on human osteoblast activity, Braz. J. Med. Biol. Res. 49 (2016) e5257.
8. D.T. Chou, D. Hong, P. Saha, J. Ferrero, B. Lee, Z. Tan, P. N. Kumta, In vitro and in vivo corrosion, cytocompatibility and mechanical properties of biodegradable Mg–Y–Ca–Zr alloys as implant materials, Acta Biomater. 9 (2013) 8518–3853.
9. T. Imwinkelried, S. Beck, B. Schaller, Pre-clinical testing of human size

magnesium implants in miniature pigs: Implant degradation and bone fracture healing at multiple implantation sites, Mater. Sci. Eng. C. 108 (2020) 110389.

10. S. Agarwal, J. Curtin, B. Duffy, S. Jaiswal, Biodegradable magnesium alloys for orthopaedic applications: A review on corrosion, biocompatibility and surface modifications, Mater. Sci. Eng. C. 68 (2016) 948-963.
11. J.X. Yang, F.Z. Cui, I.S. Lee, Y. Zhang, Q.S. Yin, H. Xia, S.X. Yang, In vivo biocompatibility and degradation behavior of Mg alloy coated by calcium phosphate in a rabbit model, J. Biomater, Appl. 27 (2012) 153–164.
12. E. Willbold, K. Kalla, I. Bartsch, K. Bobe, M. Brauneis, S. Remennik, F. Witte, Biocompatibility of rapidly solidified magnesium alloy RS66 as a temporary biodegradable metal, Acta Biomater. 9 (2013) 8509–8517.
13. B. Schaller, N. Saulacic, S. Beck, T. Imwinkelried, B.T. Goh, K. Nakahara, W. Hofstetter, T. Iizuka, In vivo degradation of a new concept of magnesium-based rivet-screws in the minipig mandibular bone, Mater. Sci. Eng. C. 69 (2016) 247-254.
14. F. Witte, V. Kaese, H. Haferkamp, E. Switzer, A. Meyer-Lindenberg, C.J. Wirth; H. Windhagen, In vivo corrosion of four magnesium alloys and the associated bone response, Biomaterials. 26 (2005) 3557–3563.
15. S. Julmi, A.K. Krüger, A.C. Waselau, A. Meyer-Lindenberg, P. Wriggers, C. Klose, H. J. Maier, Processing and coating of open-pored absorbable magnesium-based bone implants, Mater. Sci. Eng. C. 98 (2019) 1073-1086.
16. C. Janning, E. Willbold, C. Vogt, J. Nellesen, A. Meyer-Lindenberg, H. Windhagen, F. Thorey, F. Witte, Magnesium hydroxide temporarily enhancing osteoblast activity and decreasing the osteoclast number in peri-implant bone remodeling, Acta Biomater. 6 (2010) 1861–1868.
17. J. Rogowska-Tylman, J. Locs, I. Salma, B. Woźniak, M. Pilmane, V. Zalite, A. Chlanda, In vivo and in vitro study of a novel nanohydroxyapatite sonocoated scaffolds for enhanced bone regeneration, Mater. Sci. Eng. C. 99 (2019) 669-684.

18. A. Myrissa, N. A. Agha, Y. Lu, E. Martinelli, J. Eichler, G. Szakacs, A.M. Weinberg, In vitro and in vivo comparison of binary Mg alloys and pure Mg, Mater. Sci. Eng. C. 2016, 61: 865-874.
19. J. Emsley, Nature's building blocks: an A-Z guide to the elements, Oxford University Press, 2011.
20. F. Mert, C. Blawert, K. U. Kainer, N. Hort, Influence of cerium additions on the corrosion behavior of high pressure die cast AM50 alloy, Corros. Sci. 65 (2012) 145-151.
21. J. Zheng, Q. Wang, Z. Jin, T. Peng, Effect of Sm on the microstructure, mechanical properties and creep behavior of Mg–0.5 Zn–0.4 Zr based alloys, Mater. Sci. Eng., A. 527 (2010) 1677-1685.
22. G. Song, A. Atrens, Understanding magnesium corrosion—a framework for improved alloy performance, Adv. Eng. Mater. 5 (2003) 837-858.
23. W. Liu, F. Cao, L. Zhong, L. Zheng, B. Jia, Z. Zhang, J. Zhang, Influence of rare earth element Ce and La addition on corrosion behavior of AZ91 magnesium alloy, Mater. corros. 60 (2009) 795-803.
24. C. Suryanarayana, A. Inoue, Bulk Metallic Glasses, first ed., CRC, New York, 2011.
25. A. Monfared, H. Vali, S. Faghihi, Biocorrosion and biocompatibility of Zr-Cu-Fe-Al bulk metallic glasses, Surf. Interface Anal. 45 (2013) 1714–1720.
26. H. Wang, D. Ju, H. Wang, Preparation and Characterization of Mg-RE Alloy Sheets and Formation of Amorphous/Crystalline Composites by Twin Roll Casting for Biomedical Implant Application, Metals, 9 (10), 1075.
27. H.H. Liebermann. Rapidly solidified alloys made by chill block melt-spinning processes process, Journal of Crystal Growth. 70 (1984) 497-506.
28. A. Hadadzadeh, M. A. Wells, Mathematical modeling of thermo-mechanical behavior of strip during twin roll casting of an AZ31 magnesium alloy, J. Magnesium Alloys. 1 (2013) 101-114.
29. R.V. Allen, D.R. East, T.J. Johnson, W.E. Borbidge, D. Liang, Magnesium alloy sheet produced by twin roll casting, in: J.N. Hryn (Ed.), Magnesium

Technology, TMS, Indianapolis, IN, USA 2001, pp. 75–80.

30. W. H. Wang, The nature and properties of amorphous matter, Prog. Phys. 33 (2013) 177.
31. F. Spaepen, A microscopic mechanism for steady state inhomogeneous flow in metallic glass, Acta Metall. 25 (1977) 407.
32. A. Inoue, Stabilization of metallic supercooled liquid and bulk amorphous alloys, Acta Mater. 48 (2000) 279–306.
33. A. Takeuchi, A. Inoue, Calculations of mixing enthalpy and mismatch entropy for ternary amorphous alloy, Mater. Trans. JIM. 41 (2000) 1372–1378.
34. N. R. Ronco, F. Menestrina, L.M. Romero, C.B. Castells, Determination of gas–liquid partition coefficients of several organic solutes in trihexyl (tetradecyl) phosphonium dicyanamide using capillary gas chromatography columns, J. Chromatogr. A 1584 (2019): 179-186.
35. Hirschorn B, Orazem M E, Tribollet B, et al. Determination of effective capacitance and film thickness from constant-phase-element parameters. Electrochim. Acta, 2010, 55: 6218-6227.
36. Y. Song, E.H. Han, D. Shan, C. D. Yim, B. S. You, The effect of Zn concentration on the corrosion behavior of Mg-xZn alloys, Corros. Sci. 65 (2012) 322-330.
37. H.F. Li, Y.F. Zheng, Recent advances in bulk metallic glasses for biomedical applications, Acta biomater. 36 (2016): 1-20.
38. H.R. Bakhsheshi-Rad, M.H. Idris, M.R. Abdul-Kadir, A. Ourdjini, M. Medraj, M. Daroonparvar, E. Hamzah, Mechanical and bio-corrosion properties of quaternary Mg–Ca–Mn–Zn alloys compared with binary Mg–Ca alloys, Mater. Des. 53 (2014) 283-292.
39. W. Liu, F. Cao, L. Chuang, Z. Zhang, J. Zhang, Effect of rare earth element Ce and La on corrosion behavior of AM60 magnesium alloy, Corros. Sci. 51 (2009) 1334-1343.
40. F. Witte, V. Kaese, H. Haferkamp, E. Switzer, A. Meyer-Lindenberg, C.J.

Wirth, H. Windhagen, In vivo corrosion of four magnesium alloys and the associated bone response, Biomaterials. 26 (2005) 3557-3563.

41. M. P. Staiger, A. M. Pietak, J. Huadmai, G. Dias, Magnesium and its alloys as orthopedic biomaterials: a review, Biomaterials. 27 (2006) 1728-1734.
42. G. Song, Control of biodegradation of biocompatable magnesium alloys, Corros. sci. 49 (2007) 1696-1701.
43. P. A. Revell, E. Damien, X. S. Zhang, P. Evans, C. R. Howlett, The effect of magnesium ions on bone bonding to hydroxyapatite, Key. Eng. Mater. 254 (2004) 447–450.
44. A. Chaya, S. Yoshizawa, K. Verdelis, N. Myers, Costello, B. J, D.T. Chou, C. Sfeir, In vivo study of magnesium plate and screw degradation and bone fracture healing, Acta biomater. 18 (2015) 262-269.
45. F. Witte, N. Hort, C. Vogt, S. Cohen, K. U. Kainer, R. Willumeit, F. Feyerabend. Degradable biomaterials based on magnesium corrosion, Curr. Opin. State. Mater. Sci. 12 (2008) 63-72.
46. F. Witte, H. Ulrich, C. Palm, E. Willbold, Biodegradable magnesium scaffolds, Part II: peri-implant bone remodeling, J. Biomed. Mater. Res. Part A. 81 (2007) 757–765.
47. C. M. Serre, M. Papillard, P. Chavassieux, J. C. Voegel, G. Boivin, Influence of magnesium substitution on a collagen-apatite biomaterial on the production of a calcifying matrix by human osteoblasts, J. Biomed. Mater. Res. 42 (1998) 626–633.
48. J. Zhang, S. Xu, K. Wang, S. Yu, Effects of the rare earth ions on bone resorbing function of rabbit mature osteoclasts in vitro, Chin. Sci. Bull. 48 (2003) 2170–2175.
49. A. S. Karakoti, O. Tsigkou, S. Yue, P. Lee, D. P, M. M. Stevens, J. R. Jones, S. Seal, Rare earth oxides as nanoadditives in 3-D nanocomposite scaffolds for bone regeneration, J. Mater. Chem. 20 (2010) 8912–8919.
50. D. Dziuba, A. Meyer-Lindenberg, J. M. Seitz, H. Waizy, N. Angrisani, J. Reifenrath, Long-term in vivo degradation behaviour and biocompatibility of

the magnesium alloy ZEK100 for use as a biodegradable bone implant, Acta biomater. 9 (2013) 8548-8560.

Chapter 5 Influence of casting speed on microstructure and biodegradation properties of Mg-RE alloy

In this chapter, two casting speeds of 10 rpm and 30 rpm were used in vertical twin-roll casting (TRC) to obtain Mg-rare earth (Mg-RE) alloys, and their microstructures, corrosion behaviours and *in vivo* bone reactions were investigated in detail. The results indicated that the roll-castings of TRC-30 rpm exhibited a finer grain size and higher volume fraction of non-crystallization than those in castings of TRC-10 rpm. Moreover, the results of electrochemical impedance spectroscopy (EIS) and potentiodynamic polarization indicated that the castings of TRC-30 rpm displayed a higher corrosion resistance compared to those in the castings of TRC-10 rpm. Animal tests showed that a higher degree of newly formed bone tissues was achieved by implants of TRC-30 rpm. Additionally, *in vivo* tests displayed that degradation properties of the TRC-30-rpm implants were better than those of the TRC-10-rpm implants; furthermore, the degradation layer was a two-layer structure, and P and Ca were enriched in the outer degradation layer. In summary, these findings elucidated that casting speed has a substantial effect on the microstructure and degradation property of Mg-based implants, and the degradation property performs better with increased casting speed.

5.1 Introduction

Biodegradable magnesium (Mg) alloys are widely used for manufacturing biomedical implants owing to their excellent antibacterial properties, biocompatibility, and superior osseointegration [1-4]. In most cases, Mg-based alloys containing a larger grain size and many grain boundaries (GBs) are significantly limited in extensive application due to notable grain boundary corrosion [5,6]. Optimizing the microstructure of Mg-based materials has been demonstrated to be a good method to improve corrosion resistance. For example,

casting or deformation processes can increase the corrosion resistance of Mg-based alloys because of grain refinement and optimizing distribution of the secondary phase [7,8]. However, it is difficult to obtain ultrafine-grained, nanocrystalline or even amorphous biodegradable Mg alloys by applying traditional casting techniques.

Compared with traditional casting processes, the twin-roll casting (TRC) process may be an effective method for preparing materials of ultrafine-grained, nanocrystalline or amorphous structures owing to their rapid solidification rate. In addition, the TRC process combines rolling deformation and continuous casting into one process, which exhibits a potential to produce metal sheets and strips for its unique advantages, such as high productivity, a short production period, and lower energy consumption [9]. A previous study [10] showed that the vertical TRC process makes it possible to produce biodegradable Mg-based materials with nanostructured or amorphous structure. However, investigation on the effects of casting parameters on microstructure and corrosion resistance, especially practical clinical animal experiments of Mg alloy produced by vertical TRC, are very limited. It is crucial to understand the corrosion behaviour of Mg alloys with different casting methods, which is beneficial to extend the application of Mg-based biomedical implants.

In this chapter, the effects of two different roll-casting speeds on the microstructure of Mg-rare earth (Mg-RE) TRC sheets were analysed. Furthermore, the *in vitro* corrosion behaviour (in this study, “corrosion” has the same meaning as “degradation”) was characterized by electrochemical impedance spectroscopy (EIS) and potentiodynamic polarization in Hank’s balanced salt solution. *In vivo* animal testing was conducted by implanting rectangle sheets, which are an immobilized model of rat femoral, and monitoring micro-CT and histological data at different times after surgery. In summary, the current study aims to provide an idea for the efficient preparation of Mg-based alloys and to evaluate the corrosion and *in vivo* bone reactions of Mg-RE alloys with potential biomaterial applicability.

5.2 Experimental methods

5.2.1 Materials preparation

The experimental Mg-RE material was prepared by a copper mold casting method. Pure Mg, AZ31 ingot, Mg-10La and Mg-20Ce (in wt.%) were used as raw materials. The chemical compositions of the Mg-RE material were determined by X-ray fluorescence spectrometry and are listed in Table 5-1. The melting process was carried out in an electronic resistance furnace under the protection of CO_2 and SF_6 mixture gas. Then, some cube bars were cut from Mg-RE alloy ingots for TRC processing. The TRC experiments were based on a vertical twin-roll casting with roll width of 100 mm, roll radius of 150 mm, and roll gap set to 0 mm. Considering the separation force generated in the casting process, metal blocks were set at the two rotating rolls sides to form a supporting force to minimize the roll gap during the casting process as much as possible. When the alloy melted completely, the melt was introduced into the roll gap between the left and right rolls through an asbestos casting nozzle. An oil tank was placed under the rotating rolls to avoid further grain growth, so the cast sheet dipped into the tank could quickly solidify when it exited at the rolls. In the current study, two kinds of roll-casting speeds with 10 rpm and 30 rpm were adopted.

Table 5-1 Chemical composition of the Mg-RE ingots

Elements	Al	Si	Mn	Zn	La	Ce	Mg
Wt. %	3.66	0.12	0.28	0.12	1.62	3.21	Bal

The cross-section microstructure of the polished surface was observed by scanning electron microscope (SEM) with energy dispersive spectroscope (EDS) (SEM, JXA-8530F, Tokyo, Japan), and the element distribution was observed using an electron probe micro-analysis (EPMA, JXA-8530F Tokyo, Japan). The average grain size and the volume fraction of non-crystallization phase under

different conditions were measured using ImageJ software.

5.2.2 Electrochemical tests

In vitro corrosion tests were conducted at the temperature of 310 K in Hank's solution, which consisted of 8.0 g/L NaCl, 0.06 g/L $MgSO_4 \cdot 7H_2O$, 0.06 g/L KH_2PO_4, 0.1 g/L $MgCl_2 \cdot 6H_2O$, 0.1208 g/L $Na_2HPO_4 \cdot 12H_2O$, 0.14 g/L $CaCl_2$, 0.4 g/L KCl, and 1 g/L glucose. Potentiodynamic polarization (HZ700, Tokyo, Japan) and EIS (Modulab XM, Tokyo, Japan) tests were performed in a three-electrode cell. Prior to electrochemical tests, the samples with the dimension of 1 cm^2 were obtained from the roll-casting sheets and then ground to 4000 grit. The Mg-RE sample was connected as the working electrodes. Potentials were measured versus the saturated calomel reference electrode (SCE). A platinum gauze played the role of auxiliary electrode. The electrochemical tests were carried out at 310 K, and the alloy samples were immersed in Hank's solution for one hour at their open circuit potential.

The EIS tests were recorded in a frequency range from 0.01 Hz to 100000 Hz while applying a sinusoidal AC voltage signal of 0.01 V amplitude. The analyses of EIS dates were performed in an appropriate equivalent circuit (EC) model using ZSimDemo software. Subsequently, potentiodynamic polarization was initiated at a 0.01 V/s scan rate from the open circuit potential (E_{OC}) to 0.75 V_{SCE} and then from -2.35 V_{SCE} to E_{OC}.

5.2.3 In vivo bone implantation

All animal experiments were reviewed by the Saitama Institute of Technology Animal Care and Use Committee (Grant No. 2019-5). A total of 12 white rats (Wistar; male, 16 weeks of age, 340 ± 15 g) from Tokyo University Institute of Medicine were selected for the animal test. The 12 animals were divided into two groups randomly. Rectangle sheet samples (15 mm × 5 mm with a thickness 0.5 mm) were implanted as follows: TRC-10-rpm alloy in 6 rats from G1 group and TRC-30-rpm alloy in 6 rats from G2 group. Implanting rectangle sheets of these materials in a fixed model of rat femoral. Prior to surgery, the implants were

sterilized using ethylene oxide, and Mg screws were selected to fix the implants. The implantation procedure is shown in Fig. 2.25. After surgery, daily clinical observation was performed.

5.2.4 Micro-CT and histological assessments

Micro-CT (R.mCt. Rigaku, Tokyo, Japan) was performed to evaluate the formation of new bone. 3D images were obtained based on 2D image sequences. The microstructure of rats' right femurs was measured with a scanning resolution of 30 μm/slice. The trabecular bone parameters such as bone volume/tissue volume (BV/TV), trabecular separation (Tb.Sp) and trabecular thickness (Tb.Th) were quantified with Bone-J software [11]. The femur samples were fixed in 10-vol% formalin solution for three days and decalcified with a 10-vol% decalcification solution for 30 days. Then, the dehydrated samples were embedded in paraffin. Sections of the region close to the alloy site were cut and stained by haematoxylin and eosin (H&E). Details about the staining method were described in Ref. [12]. The staining slices were observed by a light microscope.

5.2.5 In vivo degradation tests

After 12 weeks of implantation, the cross section of implants was observed under SEM equipped with EDS. The structure of the degradation layer and the element distribution were analysed.

5.2.6 Statistical analysis

Statistical analyses were conducted using SPSS 18.0 software (IBM, Armonk, USA). One-way analysis of variance was performed to evaluating the differences among those specific groups ($p < 0.05$ was considered statistically significant).

5.3 Experimental results

5.3.1 Investigation of microstructures

Fig. 5.1 shows the microstructures, grain size and volume fraction of non-crystallization region of Mg-RE alloys produced under different casting speeds. The typical microstructures of Mg-RE alloy produced by the TRC-10-rpm casting method are composed of cellular crystals and an intergranular non-crystallization region (Fig. 5.1a). However, when the casting speed increases to 30 rpm, the width of the non-crystallization region is larger and discontinuous, while the crystalline structure is characterized by closely spaced secondary dendrite and fine grains (Fig. 5.1b). Consequently, the average grain size is reduced from 11.2 μm to 6.4 μm (Fig. 5.1c). The volume fraction of the non-crystallization region is increased from 3.3% to 13.2%, as shown in Fig. 5.1 (d).

The EPMA mappings in the Mg-RE alloy of the TRC-10-rpm and TRC-30-rpm specimens are shown in Fig. 5.2 (a) and 5.2 (b), respectively. It can be seen in Fig. 5.2 (a), Al, Ce and La are enriched in the non-crystallization region. Fig. 5.2 (b) indicates that there are higher contents of Al, Ce and La in the non-crystallization region compared with the crystallization region.

To further investigate the results of the alloying elements distribution, the compositions of the different points were measured by EDS (Fig. 5.3), and the corresponding results are shown in Table 5-2. Obviously, the contents of Al, Ce and La in the non-crystallization region are higher than those in crystallization region. Moreover, the Al, Ce and La concentration of Mg-RE alloy substrate in the TRC-30-rpm sheet is higher than that of the TRC-10-rpm sheet.

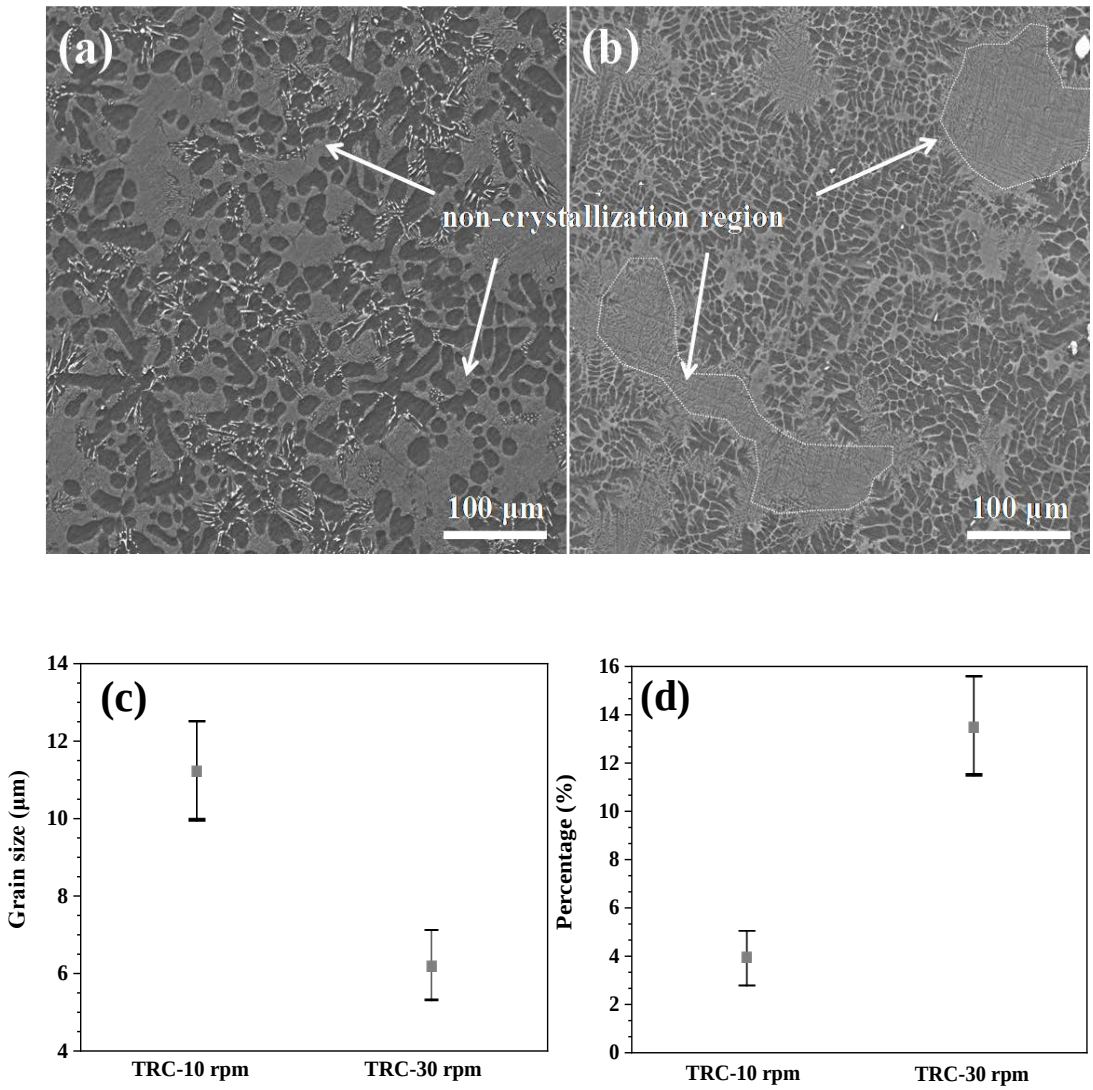

Fig. 5.1 Microstructures and the results including grain size and volume fraction of non-recrystallization region of Mg-RE alloys under different conditions: (a) TRC-10 rpm; (b) TRC-30 rpm.

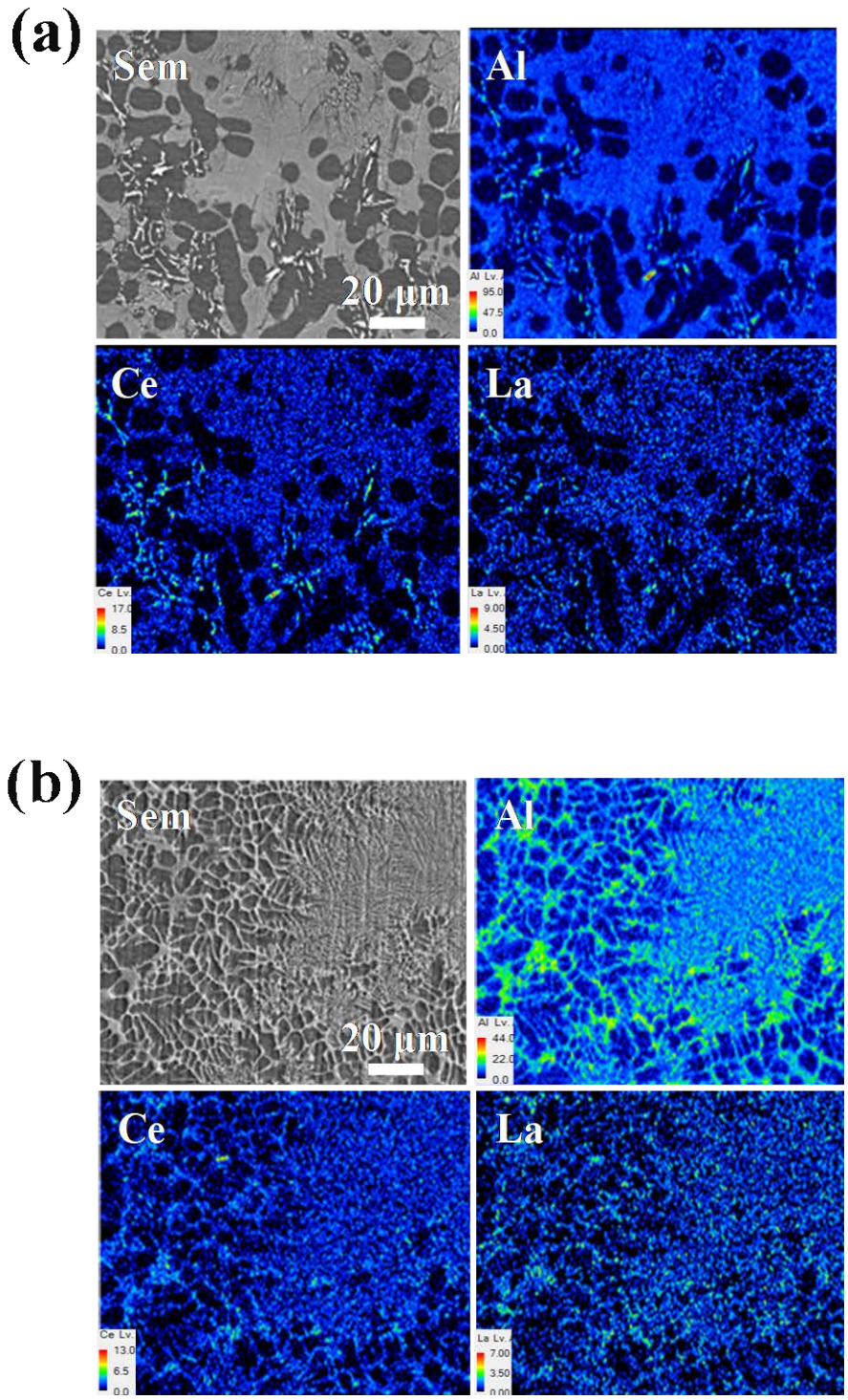

Fig. 5.2 Microstructures and EPMA of Mg-RE alloys under different conditions: (a) TRC-10 rpm; (b) TRC-30 rpm.

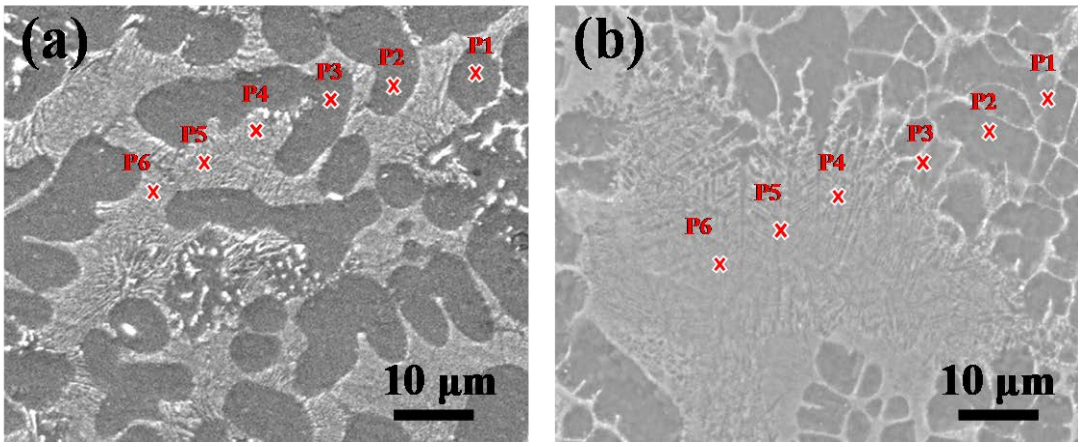

Fig. 5.3 Microstructures and measuring points of crystallization and non-crystallization regions of Mg-RE alloy: (a) TRC-10 rpm; (b) TRC-30 rpm.

Table 5-2 EDS spectra results of the crystallization and non-crystallization regions in Mg-RE alloy

Alloy	Measured regions	Measured points	Elements (wt%)		
			Al	Ce	La
TRC-10 rpm	Crystallization	P1	1.27	1.50	0.79
		P2	1.51	1.62	0.87
		P3	1.47	1.59	0.93
	Non-crystallization	P4	3.45	5.16	3.58
		P5	3.19	6.17	3.24
		P6	3.81	5.77	3.35
TRC-30 rpm	Crystallization	P1	4.23	7.33	4.92
		P2	4.14	8.65	5.52
		P3	4.35	8.79	5.64
	Non-crystallization	P4	5.23	11.25	6.13
		P5	4.62	10.55	6.30
		P6	5.43	12.31	6.81

5.3.2 Electrochemical characterization

To obtain information about the interface between the Mg-RE alloys and the Hank's solution in electrochemical processes, the EIS tests were performed in the test solution at 310 K after one-hour immersion.

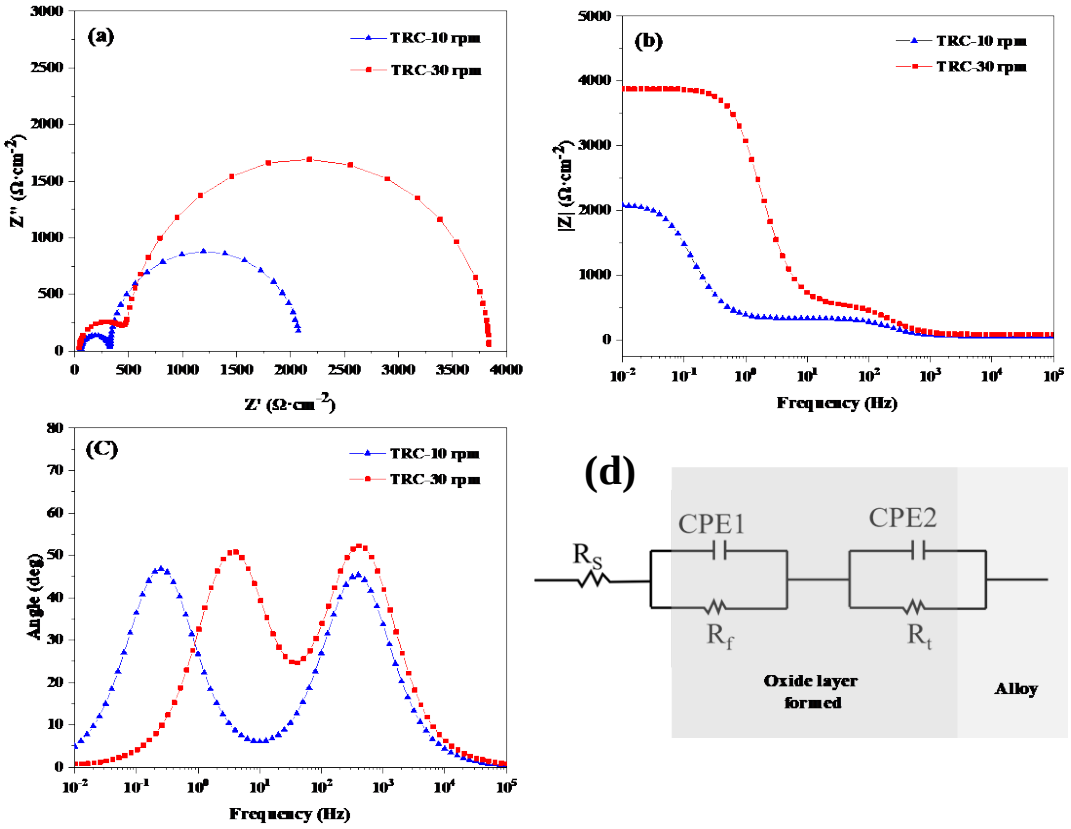

Fig. 5.4 EIS spectra of Mg-RE alloy with different casting speed in Hank's solution at 310 K after one-hour immersion: Nyquist plots (a), Bode plots (b,c) and Equivalent circuit of EIS spectra (d).

Fig. 5.4 presents the recorded impedance spectra of Mg-RE alloy in Hank's solution. The Nyquist spectra of samples with different casting speed are consisted of high-frequency capacitive semicircles and low-frequency capacitive semicircles (Fig. 5.4a). The high-frequency semicircles can be connected to the double electrochemical layer formed on the alloys surface. However, the low-frequency semicircles can be related to the passive layer generated on the surface materials. The larger diameter for the sample with TRC-30 rpm presents a higher corrosion resistance. Fig. 5.4b and 5.4c show that the impedance values monotonically increase with the decreasing frequency and two wave crests of TRC-10-rpm and TRC-30-rpm samples, which are in good consistency with the Nyquist plots.

The potentiodynamic polarization curves of Mg-RE alloy with different casting speeds in Hank's solution at 310 K after one-hour immersion are shown in Fig. 5.5.

The average values of corrosion potential (E_{corr}) and corrosion current density (i_{corr}) measured by Tafel extrapolation are presented in Table 5-3. Samples with TRC-30 rpm have more positive value of E_{corr} (-1.08 V_{SCE}) and lower i_{corr} (1.48×10^{-4} A cm^{-2}), which implies the samples of TRC-30 rpm present a higher corrosion resistance.

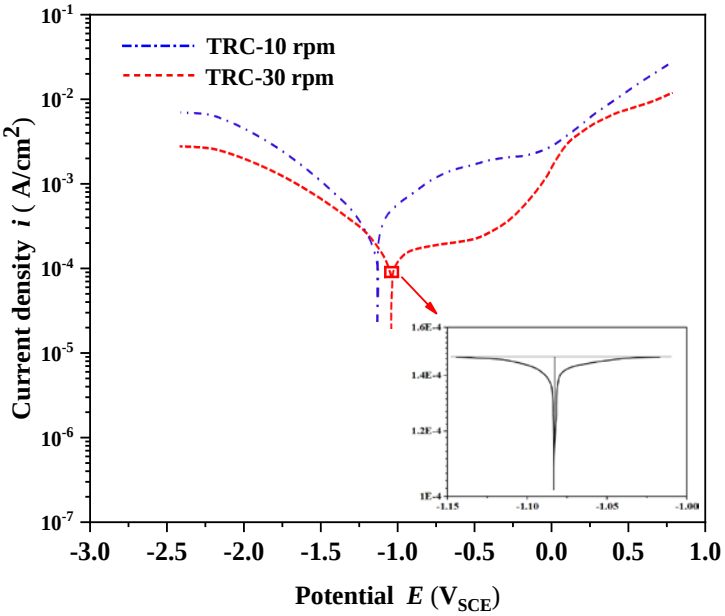

Fig. 5.5 Potentiodynamic polarization curves of Mg-RE alloy with different casting speed in Hank's solution at 310 K after one-hour immersion. The inset shows Tafel analysis for Mg-RE alloy.

Table 5-3 Average values measured from potentiodynamic polarization curves for the Mg-RE alloy in Hank's solution at 310 K after one-hour immersion

Sample	E_{corr} /V_{SCE}	$-\beta_c$/V decade^{-1}	β_a/V decade^{-1}	i_{corr}/A cm^{-2}
TRC-10 rpm	-1.17	0.139	0.179	2.23×10^{-3}
TRC-30 rpm	-1.08	0.142	0.188	1.48×10^{-4}

5.3.3 Micro-CT and histological characterization

Micro-CT technology offers a non-invasive and accurate assessment of the bone tissues changes and implants *in vivo* [13]. Fig. 5.6 illustrates the micro-CT

and histological observation of the interfaces between the Mg-RE alloy implants and bone tissues. After 4 weeks, there is a continuous small amount of newly formed bone (NB) around the two group implants (I). 12 weeks postoperatively, more newly bone tissues are observed around the two group implants. It can be seen from histological images, for the TRC-30-rpm group, the newly formed bone trabeculars (BT) becomes thinner 12 weeks after surgery, which implies there is more obvious ossification.

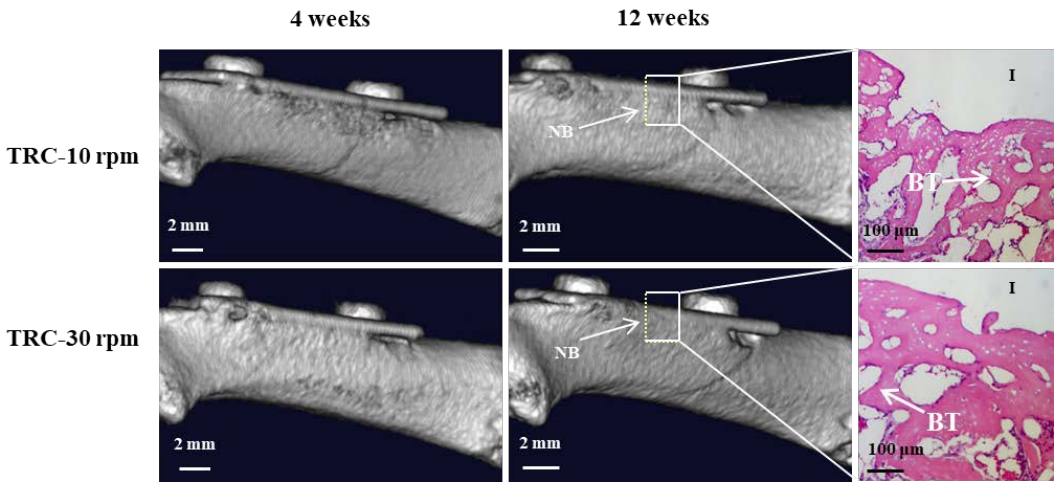

Fig. 5.6 Representative micro-CT 3D images and the histological observation of the interfaces between the Mg-RE alloy implants and bone tissues. Micro-CT 3D rendering presents the newly bones (NB) around the two group implants (I). H&E histological stain shows bone trabeculars (BT) within the newly formed bone after 12 weeks.

Table 5-4 Average quantitative parameters of bone morphometric indexes measured for the rat animal model with the Mg-RE implant 12 weeks after surgery as determined by micro-CT

Sample	BV (mm2)	TV (mm2)	BV/TV	Tb.Th (μm)	Tb.Sp (μm)
TRC-10 rpm	4.87	6.25	0.78	26.29	51.21
TRC-30 rpm	6.59	7.91	0.83	37.47	32.93

The average quantitative parameters of bone morphometrics were evaluated, as shown in Table 5-4. The group samples of TRC-30 rpm present a higher value for BV/TV, indicating a more intensity new bone formed in this rat model. In addition, although statistically insignificant ($p > 0.05$), the values of Tb.Th and Tb.Sp of the new bone tissue presented better extensibility for the Mg-RE alloy of TRC-30 rpm.

5.3.4 In vivo degradation

The Mg-RE alloy samples were collected after 12 weeks of implantation. Fig. 5.7 shows representative micrographs of the cross section and corresponding EDS line scanning observation of the alloy samples.

It can be seen that the characteristic corrosion layer of Mg-RE alloy exhibits two-layer structure. The degradation layers with different thickness are found in Mg-RE alloys. For Mg-RE alloy of TRC-10 rpm, the thickness of inner layer is ~25 μm, and the outer layer is ~40 μm, in addition, some micro-cracks could be found in both inner and outer layer. The generation of micro-cracks is probably due to the accelerate dissolving of degradation products. However, for Mg-RE alloy of TRC-30 rpm, the thickness of inner layer and outer layer are ~15 μm and ~30 μm, respectively. This two-layer structure is compact and uniform, and no obvious micro-cracks are found during the investigation. The elements in the degradation layer are listed in Fig. 5.7. In addition, there are mainly O, C, P and Ca in the whole degradation layer.

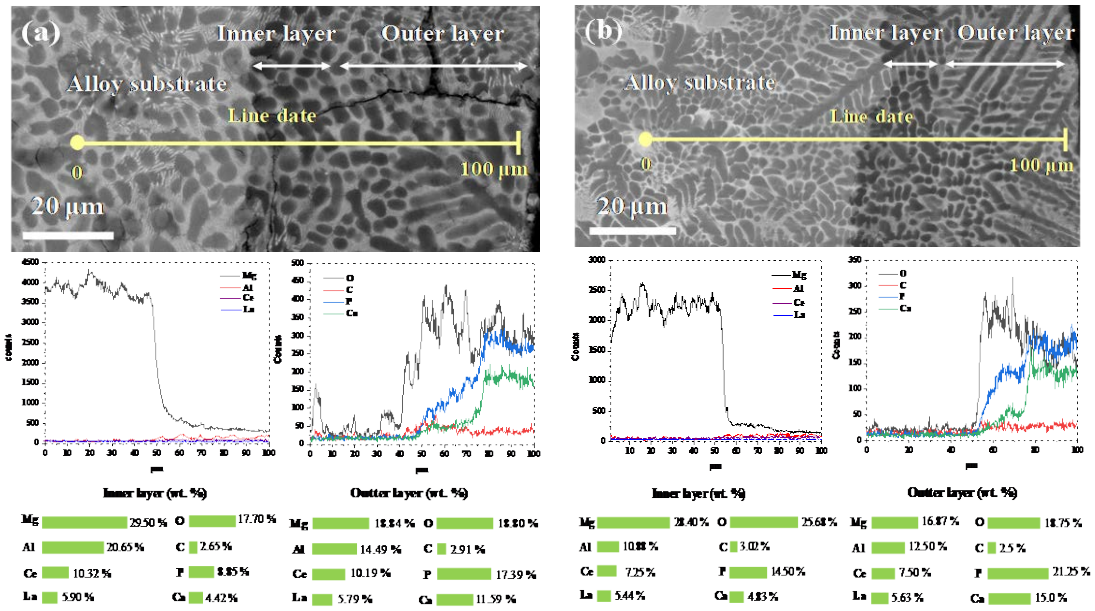

Fig. 5.7 Representative SEM images showing the cross section of the degradation layer and corresponding EDS line scanning observation of Mg-RE alloy with (a) TRC-10 rpm and (b) TRC-30 rpm after implantation for 12 weeks.

5.4 Discussion of experimental results

5.4.1 Microstructure analyses

An obvious feature of the TRC process is that the large thermal gradient along the thickness direction leads to rapid directional solidification [14,15]. Consequently, combined with the rolling effect, cellular mechanisms, closely spaced secondary dendrite, non-crystallization and fine grains are the common crystalline characteristics in as-cast TRC sheets [16, 17]. During the TRC process, the cooling intensity in the roll-casting area is mainly depend on set-back distance and casting speed. In this study, the set-back distance shows almost no change in the casting process. The contacting time of the metal melt and roller shell in the 30-rpm case is nearly 3 times of that in the 10-rpm case. Therefore, the cooling intensity in the former case is three times higher than that in the latter case.

Based on the fundamental of solidification, constitutional undercooling will form in the solid-liquid interface. The solid-liquid interface rejects the solution and

accumulates solute, enabling cellular structure to grow stably under the initial small disturbance. As the cooling rate increases, closely spaced secondary dendrite forms instead of cellular mechanism for larger constitution undercooling. In the present study, the alloys are extruded and deformed, which means grain growth and recrystallization would occur during the solidification process. When the cooling rate is high, due to the crystal structure change, recrystallization does not occur completely. As a result, the grain size of the alloy of TRC-30 rpm is smaller than that of the alloy of TRC-10 rpm.

As seen from Table 5-2, the contents of Al, Ce and La in the non-crystallization region are significantly higher than those in the crystallization region of the TRC-10-rpm and TRC-30-rpm sheets. Elements dissolution is related to the solute partition coefficient (K), and K can be expressed as the following equation during the solidification process [18]:

$$K = C_S / C_L \qquad (5.1)$$

where C_S and C_L are solute concentration in solid phase and liquid phase, respectively. The K of the Al, Ce and La is less than 1 during the Mg-RE alloy melt solidification; therefore, in a preferentially crystallized solid, the C_S is always less than the C_L, which leads to Al, Ce and La atoms constantly being released into the liquid phase.

According to the solidification theory, the solute content in the solidified phase (C^*_S) can be calculated by the following Scheil-Gulliver equation [19]:

$$C^*_S = k_0 C_0 [1 - f_S / (1+\alpha k_0)]; \alpha = D_S \tau / S^2 \qquad (5.2)$$

where k_0 and C_0 are the equilibrium partition coefficient and the initial melt compositions, respectively; DS is solid phase diffusion coefficient; τ is partial solidification time; S and f_S are half distance of dendrite spacing and solid phase mass fraction at solid-liquid interface, respectively. Based on equation (5.2), the solute content in the solid phase is closely related to the type of dendrite in the crystal structure. Therefore, it is easy to infer that the content of solid elements increases with the increase of roll-casting speed from 10 to 30 rpm. The solute

elements such as Al, Ce and La in the TRC-30-rpm sheet are higher than those of the TRC-10-rpm sheet, which shows that the experimental results are in good agreement with the theoretical analysis.

5.4.2 Electrochemical test analyses

The corrosion behaviour of the Mg-RE alloy was investigated by means of electrochemical tests during the immersion in Hank's solution at 310 K. The EIS of the Mg-RE alloy was characterized by two time constants, one corresponding to the charge transfer process between solution and the alloy surfaces, and the other one corresponding to the thin passivating oxide film. Hence, the corrosion resistance of the Mg-RE alloy is associated with the formation of a protective oxide layer. When further increasing the intensity of passive layer, the corrosion resistance of the underlying metal becomes greater.

Table 5-5 Impedance fitting results for the Mg-RE alloy

Alloy	R_S	CPE1		R_f	CPE2		R_t
	(Ω cm^2)	Q_f (μF cm^{-2}s^n)	n	(kΩ cm^2)	Q_t (μF cm^{-2}s^n)	n	(kΩ cm^2)
TRC-10 rpm	58.25	2.45	0.84	1.76	921.80	0.82	0.27
TRC-30 rpm	61.54	3.81	0.81	3.36	37.14	0.83	0.44

The quantitative date of the EIS results obtained using an equivalent circuit (EC) are shown in Fig. 5 (d), and the fitting results are presented in Table 5-5. The EC model consisted of R_S (solution resistance), R_t (charge-transfer resistance), R_f (film resistance), and constant elements CPE1 and CPE2. CPE1 and CPE2 represent the capacitive behaviours of growth the oxidation film and charge-transfer, respectively, Q is the CPE magnitude, and the n value is a nature element [20]. According to previous studies [21], the EC model illustrates a two-layer oxide film consisting of an outer layer and an inner layer. The passive two-layer oxide film formed on the metal surface alleviated the direct contact between the metal

and corrosion media, which results in enhanced corrosion resistance of the alloy substrate.

The use of constant element CPE (defined by Q and n) cannot be the accurate value of capacitance [22]. B. Hirschorn et al. [23] reported the effective capacitance (C_f) can be calculated by the following equation:

$$C_f = Q^{1/n} [R_S R_f / (R_S + R_f)]^{(1-n)/n} \qquad (5.3)$$

where C_f represent the value of the oxidation film in μF cm^{-2}, and n is the CPE index. It can be found that the calculation results of the Mg-RE alloys of TRC-10 rpm and TRC-30 rpm are 6.26 μF cm^{-2} and 13.87 μF cm^{-2}, respectively. The change of C_f is related to the thickness film (d), surface area (s), relative dielectric constant (ε) and permittivity of vacuum (ε_o) of the oxide film which can be expressed as the following equation [24]:

$$C_f = \varepsilon\varepsilon_o s / d \qquad (5.4)$$

where ε and ε_o are constant, and s is the corrosion film area. Thus, the lower C_f value of the Mg-RE alloy of TRC-10 rpm shows a thicker corrosion film that is formed in the initial process. Indeed, the protective passive corrosion film offers the major contribution of high corrosion resistance for all Mg-RE alloys in Hank's solution. The value of R_f represents the passive film resistance as observed in Table 5-5. The results demonstrate that Mg-RE alloys of TRC-30 rpm possess better corrosion protection and lower dissolution.

Lower corrosion current density and more positive corrosion potential values were plotted in the polarization curves for Mg-RE alloys of TRC-30 rpm. This result demonstrates that the Mg-RE alloys exhibit better corrosion resistance with high roll-casting speed. This result demonstrates that the Mg-RE alloys exhibit better corrosion resistance with high roll-casting speed. On one hand, previous studies [25,26] have reported that the corrosion resistance of Mg-based alloy can be significantly improved by grain refinement. The larger grain size of α-Mg may cause galvanic corrosion because of the difference of electric potential with secondary phases [27,28]. On the other hand, the amounts of inert elements such

as Al, Ce and La are more enriched in the non-crystallization regions. Consequently, the corrosion resistance increases with the increasing casting speed.

5.4.3 In vivo degradation property analyses

This work evaluated the *in vivo* bone tissue reaction of Mg-RE alloys using an immobilized implantation model in rat femoral model. Micro-CT was used to investigate the newly formed bone tissue accumulated around the implant materials. The 3D rendering demonstrates that the interface of the femur and the Mg-RE alloy of TRC-30 rpm is deposited in greater proportion of newly formed bone.

Previous studies [29-31] indicate that local bone tissues are stimulated by Mg ions to form new bone. However, excess Mg ions released with Mg-based material degradation could dampen the formation of new bone tissue [32]. The electrochemical experiments show that the Mg-RE alloy of TRC-30 rpm possesses greater corrosion resistance than the alloy of TRC-10 rpm. The results indicate that the degradation layer of the Mg-RE alloy of TRC-30 rpm has a relatively low release rate of Mg ions. Thus, the Mg-RE of TRC-30-rpm group promotes higher ability of newly formed bone during the 12 weeks after implantation.

The degradation layer shows a two-layer structure with different thicknesses, which is consistent with the conclusions of electrochemical characterization. In addition, there are O, Mg, C, P and Ca in the degradation layer for *in vivo* tests. Mg dissolves in body fluids based on following equations:

$Mg \rightarrow Mg^{2+} + 2e$; anodic reaction.

$2H_2O + 2e \rightarrow H_2 + 2OH^-$; cathodic reaction.

$Mg(OH)_2$ changes $MgCl_2$ under the action of the cathodic ion (Cl^-), which can increase the PH of the solution and result in further dissolution of Mg [6,33]. Furthermore, Ca^{2+} and PO^{4-} in body fluids reacts with OH^- to form $Ca_{10}(PO_4)(OH)_2$ [34,35]. It is worth noting that in both Mg-RE alloys, the outer layer contains more P and Ca than in the inner layer. Previous studies have reported

that these degradation products can promote newly formed bone and show good biocompatibility [36]. Therefore, it could be concluded that the degradation product of the Mg-RE alloy is acceptable and good. However, the dissolution mechanism of the degradation layer remains to be further studied.

In summary, based on the results of investigations, the research shows an intrinsic link between the casting speed and the properties including the biological application of the Mg-RE alloy. As mentioned above, the higher casting speed could produce higher cooling rate, a smaller casing grain size and higher volume fraction of non-crystallization. In addition, alloying elements such as Al, Ce and La in Mg-RE alloy are significantly enhanced in alloy substrate with a faster cooling rate, and the same trends were reported by Li et al. [37]. The above microstructural features of the Mg-RE alloy could increase corrosion resistance in a faster casting speed. Moreover, as alloying elements of Mg, the rare-earth elements (REEs) such as Ce, La are more suitable for bone regeneration application compared to pure Mg [38,39]. The results of *in vivo* confirmed that the Mg-RE implant of TRC-30 rpm exhibit better bone formation with a faster casting speed. This work could provide a new understanding of the development of the Mg alloy using the TRC process to improve the degradable performance of potential orthopaedic implants.

5.5 Concluding remarks

In this chapter, to provide an idea for the efficient preparation of Mg-based alloys with potential biomaterial applicability, two casting speeds of 10 rpm and 30 rpm were used in vertical TRC to obtain the Mg-RE alloys, and the corresponding the microstructure, corrosion behavior and in vivo bone reaction were discussed in detail. According to the system analysis, the conclusions are summarized as follow:

(1) It is found that the roll-castings of TRC-30 rpm present a finer grain size and higher volume fraction of no-crystallization compared to that of TRC-10 rpm.

(2) The results of electrochemical tests show that the Mg-RE alloys of TRC-30 rpm exhibit a higher corrosion resistance with respect to the alloys of TRC-10 rpm.

(3) The present animal tests show that Mg-RE alloys of TRC-30 rpm promote more newly formed bone tissues than that of TRC-10 rpm group.

(4) In vivo implants degradation tests demonstrate that the degradation layer exhibits two-layer structure. In addition, P and Ca are enriched in the outer degradation layer of Mg-RE alloys. These findings provide a better understanding of in vivo degradation mechanism of Mg-RE implants.

5.6 References

1. Lee J W, Han H S, Han K J, et al. Long-term clinical study and multiscale analysis of in vivo biodegradation mechanism of Mg alloy. Proc Natl Acad Sci, 2006, 113: 716–721.
2. Brown A, Zaky S, Sfeir C, et al. Porous magnesium/PLGA composite scaffolds for enhanced bone regeneration following tooth extraction. Acta Biomater, 2015, 11: 543-553.
3. Zhao D, Huang S, Lu F, et al. Vascularized bone grafting fixed by biodegradable magnesium screw for treating osteonecrosis of the femoral head. Biomater, 2016, 81: 84-92.
4. Xie G, Wang X. Metallic Glasses for Biomedical Applications. In: Setsuhara Y, Kamiya T, Yamaura S, eds. Novel Structured Metallic and Inorganic Materials. Singapore: Springer, 2019. 421-433
5. Xin R, Luo Y, Zuo A, et al. Texture effect on corrosion behavior of AZ31 Mg alloy in simulated physiological environment. Mater Lett, 2012, 72: 1–4.
6. Zhang S, Zhang X, Zhao C, et al. Research on an Mg-Zn alloy as a degradable biomaterial. Acta Biomater, 2010, 6: 626–640.
7. Vojtěch D, Kubásek J, Serák J, et al. Mechanical and corrosion properties of newly developed biodegradable Zn-based alloys for bone fixation. Acta Biomater, 2011, 7: 3515–3522.
8. Gui Z, Kang Z, Li Y. Mechanical and corrosion properties of Mg-Gd-Zn-Zr-Mn biodegradable alloy by hot extrusion. J Alloys Compd, 2016, 685: 222–230.
9. Lv Z, Du F, An Z, et al. Centerline segregation mechanism of twin-roll cast A3003 strip. J Alloy Compd, 2015, 643: 270-274.
10. Wang H, Ju D, Wang H. Preparation and Characterization of Mg-RE Alloy Sheets and Formation of Amorphous/Crystalline Composites by Twin Roll Casting for Biomedical Implant Application. Met, 2019, 9: 1075.
11. Doube M, Michał M, Arganda-Carreras I, et al. BoneJ: free and extensible bone image analysis in ImageJ. Bone, 2010, 47: 1076–1079.
12. Fântânariu M, Trincă L C, Solcan C, et al. A new Fe-Mn-Si alloplastic biomaterial as bone grafting material: in vivo study. Appl Surf Sci, 2015, 352: 129–139.
13. Roshan-Ghias A, Vogel A, Rakotomanana L, et al. Prediction of spatio-temporal bone formation in scaffold by diffusion equation. Biomater, 2011, 32: 7006–7012.

14. Sun N, Patterson B R, Suni J P, et al. Microstructural evolution in twin roll cast AA3105 during homogenization. Mater Sci Eng A, 2006, 416: 232–239.
15. Gras C, Meredith M, Hunt J D. Microstructure and texture evolution after twin roll casting and subsequent cold rolling of Al-Mg-Mn aluminium alloys. J Mater Process Technol, 2015, 169: 156–163.
16. Chen S, Chen J. Simulation of microstructures in solidification of aluminum twin-roll casting. Trans Nonferrous Met Soc China, 2012, 22: 1452–1456.
17. Haga T, Takahashi K, Ikawa M, et al. A vertical-type twin roll caster for aluminum alloy strips. J Mater Process Technol, 2003, 140: 610–615.
18. Ronco N R, Menestrina F, Romero L M, et al. Determination of gas–liquid partition coefficients of several organic solutes in trihexyl (tetradecyl) phosphonium bromide using capillary gas chromatography columns. J Chromatogr A, 2019, 1584: 179-186.
19. Schaffnit P, Stallybrass C, Konrad J, et al. A Scheil–Gulliver model dedicated to the solidification of steel. Calphad, 2015, 48: 184-188.
20. Jia H, Feng X, Yang Y. Effect of grain morphology on the degradation behavior of Mg-4 wt% Zn alloy in Hank's solution. Mater Sci Eng C, 2020, 106: 110013.
21. Pan J, Thierry D, Leygraf C. Electrochemical impedance spectroscopy study of the passive oxide film on titanium for implant application. Electrochim Acta, 1996, 41: 1143–1153.
22. Hirschorn B, Orazem M E, Tribollet B, et al. Constant-Phase-Element Behavior Caused by Resistivity Distributions in Films. J Electrochem Soc, 2010, 157: C452-C457.
23. Hirschorn B, Orazem M E, Tribollet B, et al. Determination of effective capacitance and film thickness from constant-phase-element parameters. Electrochimica Acta, 2010, 55: 6218-6227.
24. Musiani M, Orazem M E, Pébère N, et al. Constant-Phase-Element Behavior Caused by Coupled Resistivity and Permittivity Distributions in Films. J Electrochem Soc, 2011, 158: C424-C428.
25. op't Hoog C, Birbilis N, Estrin Y. Corrosion of pure Mg as a function of grain size and processing route. Adv Eng Mater, 2008, 10: 579-582.
26. Birbilis N, Ralston K D, Virtanen S, et al. Grain character influences on corrosion of ECAPed pure magnesium. Corros Eng Sci Technol, 2010, 45: 224-230.
27. Song Y, Shan D, Chen R, et al. Effect of second phases on the corrosion behaviour of wrought Mg–Zn–Y–Zr alloy. Corros Sci, 2010, 52: 1830-1837.

28. Argade G R, Panigrahi S K, Mishra R S. Effects of grain size on the corrosion resistance of wrought magnesium alloys containing neodymium. Corros Sci, 2012, 58: 145-151.
29. Witte F, Hort N, Vogt C, et al. Degradable biomaterials based on magnesium corrosion. Curr Opin Solid State Mater Sci, 2008, 12: 63-72.
30. Witte F, Ulrich H, Palm C, et al. Biodegradable magnesium scaffolds: Part II: peri-implant bone remodeling. J Biomed Mater Res Part A, 2007, 81: 757–765.
31. Yang J X, Cui F Z, Lee I S, et al. In vivo biocompatibility and degradation behavior of Mg alloy coated by calcium phosphate in a rabbit model. J Biomater Appl, 2012, 27, 153–164.
32. Serre C M, Papillard M, Chavassieux P, et al. Influence of magnesium substitution on a collagen-apatite biomaterial on the production of a calcifying matrix by human osteoblasts. J Biomed Mater Res, 1998, 42: 626–633.
33. Bakhsheshi-Rad H R, Idris M H, Abdul-Kadir M R, et al. Mechanical and bio-corrosion properties of quaternary Mg–Ca–Mn–Zn alloys compared with binary Mg–Ca alloys. Mater Des, 2014, 53: 283-292.
34. Zong Y, Yuan G, Zhang X, et al. Comparison of biodegradable behaviors of AZ31 and Mg–Nd–Zn–Zr alloys in Hank's physiological solution. Mater Sci Eng B, 2012, 177: 395-401.
35. Miao H, Zhang D, Chen C, et al. Research on biodegradable Mg–Zn–Gd alloys for potential orthopedic implants: In Vitro and in Vivo Evaluations. ACS Biomater Sci Eng, 2019, 5: 1623-1634.
36. Witte F, Kaese V, Haferkamp H, et al. In vivo corrosion of four magnesium alloys and the associated bone response. Biomater, 2005, 26: 3557-3563.
37. Li S, He C, Fu J, et al. Evolution of microstructure and properties of novel aluminum-lithium alloy with different roll casting process parameters during twin-roll casting. Mater Charact, 2020, 161: 110145.
38. Willbold E, Gu X, Albert D, et al. Effect of the addition of low rare earth elements (lanthanum, neodymium, cerium) on the biodegradation and biocompatibility of magnesium. Acta Biomater. 2015, 11: 554-562.
39. Liu J, Bian D, Zheng Y, et al. Comparative in vitro study on binary Mg-RE (Sc, Y, La, Ce, Pr, Nd, Sm, Eu, Gd, Tb, Dy, Ho, Er, Tm, Yb and Lu) alloy systems. Acta Biomater, 2020, 102: 508-528.

Chapter 6 Conclusions

In this research, we have developed a novel magnesium alloy by a vertical-type twin-roll caster (TRC) method, and its microstructure features were characterized by scanning electron microscopy (SEM), X-ray diffraction (XRD) and electron probe microanalysis (EPMA) and transmission electron microscopy (TEM), and the corrosion behaviors of Mg-RE alloy sheet have been investigated in corrosive solution by electrochemical techniques and immersion test in a simulated physiological condition. Furthermore, it was implanted into the femur of rat to explore its prospect as biological transplantation material. The following conclusion can be drawn from the results of the results of experiment studies:

1. According to the preparation and characterization of Mg-RE alloys by vertical-type twin roll casting, the conclusions have been obtained as follows:

(1) A new magnesium alloy Mg-RE (La, Ce) alloy sheets were prepared by vertical-type twin roll casting. Its microscopic characterization experiments shown that the microstructure structure is crystalline phase containing amorphous phase. This particular microstructure composed of amorphous/crystalline composite.

(2) EPMA experiments show that Al, La and Ce element are enriched in the amorphous phase region and grain boundary region. However, Mg is evenly distributed throughout the microscopic region. This shows that segregation is more likely to affect Al, La and Ce elements.

(3) Electrochemical tests and immersion results both showed that Mg-RE sheet with TRC has a better corrosion resistance than master alloy, and a uniform corrosion layer on the surface.

(4) *In vivo*, as an implant material, the tests show that Mg-RE alloys sheets were safe with respect to rat physical fitness and induced new bone formation; thus, they were promising for utilization as implant materials in the future.

2. According to the scheme of animal experiment was designed and the degradation characteristics, bone reaction of the three implants (Ti, AZ31, Mg-RE) *in vivo* were compared. The *in vivo* tests the conclusions have been obtained as follows:

The Mg-RE and AZ31 alloy sheets with same continuous casting conditions for *in vivo* implants were prepared by TRC process. The microstructure, in vivo degradation behavior and bone response for 16 weeks of Mg-RE and AZ31 sheets were investigation systematically. We found that the Mg-RE present a better amorphous forming ability than AZ31 under the same casting conditions. *In vivo* study showed that no significant change was found in the femur surrounding Ti sheet. This excluded the external factor that the new bone formation resulting from bone remodeling. The Mg-RE experienced much lower degradation rate than AZ31. Much more new bone tissue around the Mg-RE sheet and it indicates that the Mg-RE have potential to be implants for widely applied.

3. Two types of Mg-rare earth alloys were produced by using different casting speeds and the corresponding the microstructure, corrosion behavior and in vivo bone reaction were discussed in detail. According to the system analysis, the conclusions are summarized as follow:

(1) It is found that the roll-castings of TRC-30 rpm present a finer grain size and higher volume fraction of no-crystallization compared to that of TRC-10 rpm.

(2) The results of electrochemical tests show that the Mg-RE alloys of TRC-30 rpm exhibit a higher corrosion resistance with respect to the alloys of TRC-10 rpm.

(3) The present animal tests show that Mg-RE alloys of TRC-30 rpm promote more newly formed bone tissues than that of TRC-10 rpm group.

(4) *In vivo* implants degradation tests demonstrate that the degradation layer exhibits two-layer structure. In addition, P and Ca are enriched in the outer degradation layer of Mg-RE alloys. These findings provide a better understanding of in vivo degradation mechanism of Mg-RE implants.

The main innovation of this research is the amorphous/crystalline composite Mg-RE alloy sheets were prepared by a vertical-type twin-roll caster (TRC) of quench solidification method. What's more, *in vivo* as an implant material tests show that Mg-RE alloy sheet have better biocompatibility and induce new bone formation, and was promising to be utilized as implant materials in the future.

It is notable noting that there are limitations in the research. Firstly, it is not known the serum metabolic parameters of the animal body during the process of implants degradation. Secondly, in this study, the surgical was performed when the bone was completely healthy. Finally, the expected effect of this study is that the Mg-RE alloy material is almost completely degraded, but only the amorphous phase is left and is contained in the new bone. The effect is to prevent the release of Al in the alloy, thus eliminating the harm of Al to the organism. However, the expected ideal effect has not yet appeared due to the operation time of this study is only 16 weeks.

Therefore, further experimental studies are needed to investigate whether Mg-RE has a therapeutic effect on clinical healing of fractures or bone damage. In addition, the mechanism of new bone formation induced by Mg-rare earth alloy is still unclear, which needs further study in the future.

Related publications

Journal Article:

1. **H Wang**, D Ju, & H Wang. Preparation and Characterization of Mg-RE Alloy Sheets and Formation of Amorphous/Crystalline Composites by Twin Roll Casting for Biomedical Implant Application. *Metals*, *9*(10): (2019) 1075.

2. **H Wang**, H Wang, T Kumazawa, D Ju & J Cao. Effect of casting speed on microstructure, corrosion behaviour and *in vivo* bone reaction of Mg-rare earth alloys. *Science China Technological Science.* (Accepted, in press).

3. **H Wang**, T Kumazawa, Y Zhang, H Wang & D Ju. *In vivo* degradation behaviour and bone response of a new Mg-rare earth alloy immobilized in a rat femoral model. *Materials Today Communications*. (Minor Revision).

International Conferences:

1. **H Wang**, D Ju. Study on Development of Novel Mg-Based Alloys by Rapid Solidification Technology of Twin Roll Casting. ***The 5th International Conference on Nanomechanics and Nanocomposites (ICNN5). 22 to 25 August 2018, Fukuoka Japan.***

2. **H Wang**, D Ju. In Vivo Study of Biodegradation and Osteogenic Capacity of Mg-RE Sheet and AZ31 Screw in Immobilized Rat Femoral Model. ***The 10th International Forum on Advanced Materials Science and Technology (IFAMST) and The 1st Materials Conference in Guangdong-Hong Kong-Macao Greater Bay Area. December 19-22, 2019. Shenzhen China.***

Project Research Report:

1. **H Wang**, D Ju. Development of Mg-based amorphous alloy for biomaterials. ***Cooperative Research and Development Center for Advanced Materials (CRDAM), Institute for Materials Research (IMR), Tohoku University (Project Number 18G0042), Sendai Japan.***

Acknowledgements

I would like to express my sincere gratitude to my advisor, Prof. Dong-Ying JU and Prof. Jian-Ting CAO, for taking me as their student and giving me the opportunity to pursue for my research at Saitama Institute of Technology. Here, I would like to give my sincere thanks for their support, encouragement and guidance throughout my study. Without their painstaking efforts in revising and polishing my drafts, the completion of the present thesis would not have been possible. They devote a considerable portion of his time to reading my manuscripts and making suggestions for further revisions.

I would like to thank Prof. Kumazawa, who is a warm-hearted, responsible and enthusiastic person for scientific research and life. In the animal experiment, he helped me complete the implantation of experimental materials and the anatomy experiment. I couldn't have finished my experiment without his support. I have learned a lot from him, whether in life or in study, which has benefited all my life.

I would thank Prof. Uchida who is patient and willing to teach, and gave me many valuable suggestions and help in microstructure measurement. Also, I would thank Prof. Sato who attended my presentation, and for his productive suggestions and taking time away from their busy schedules to serve on my committee.

I would also thank all the Ju laboratory members in over the years for their enjoyable help and collaboration.

Finally, my deep appreciation is my family for their love, support and encouragement throughout my study and graduate work.

August, 2020

Haijian Wang